이학석사 학위논문

나노입자 탐침을 이용한 탐침증강 분광법

Nanoparticle Probes for Tip-Enhanced Spectroscopy

2016년 2월

서울대학교 대학원

화학부 물리화학

김 나 라

Abstract

Nanoparticle Probes for Tip-Enhanced Spectroscopy

NARA KIM
Department of Chemistry
The Graduate School
Seoul National University

For exploring chemical and physical properties of nanoscale objects, chemical information of single molecule and optical images with high spatial resolution is imperative. In this regard, tip-enhanced near-field optical microscopy (TENOM) is an evolving field having extensive potential. Because it provides higher spatial resolution as well as the electric field enhancement at the tip-end. This means, in other words, plasmonic enhancement and spatial confinement within the tip are critically connected to the enhanced optical signal. Therefore, we explored enhanced optical signals with various kinds of the probes to find the optimal plasmonic properties of the probes.

To apply the TENOM, we use a confocal microscopy with a radially polarized light at 532 nm wavelength and an atomic force microscopy (AFM) fitted with the tip. To check the validation of our experimental setup, we first examined the radial polarizer which generates the polarization component of a laser at 532 nm parallel to the tip (z-aixs). By getting fluorescence images of nile red (in polystyrene beads with a diameter 20 nm) in both radial and azimuthal mode, we were convinced that polarization of laser was parallel to the z-axis in the focal plane. And then, experiments for tip-enhanced Raman scattering (TERS) and fluorescence (TEF) were

conducted with two types of special fabricated probes which were synthesized in a similar way.

In order to guarantee the our setup is available for the TERS and TEF measurements, we used a nanoparticle - a Au core/Ag shell nanoparticle (Au@AgNP) with a controlled thickness of shell - attached probe. For the synthesis of Au@AgNP probe, a seed Au nanoparticle (NP) is picked up by DNA-DNA interaction and enhanced with a silver solution were employed. For the TERS measurement, the self-assembled biphenyl-4-thiol (BPT) monolayer on Au film as the sample was employed with the Au@AgNP (size: 20-90 nm) probe. We find that such tips show high plasmonic field enhancement and this reveals clearly as size of NPs increases.

For a further study, we developed a scanning probe with a metallic nanostar (a core diameter of ~70 nm and spike lengths between 50 nm and 80 nm). The approach involves AuNP pickup process and growth of spikes through reduction of Au^{3+} with ascorbic acid in the presence of Ag^{+}. The nanostar probe makes the narrow enhancement field on account of its sharp edge. We find that nearly all of the tips show the local field enhancement up to 100-fold with an improved optical resolution below 100 nm for TERS and TEF was confirmed. These were evaluated with DiI dye for TEF and crystal violet for TERS. The current probe, however, shows large tip-to-tip variability, which may arise from the uncontrolled orientation of the apexes of the spike with respect to the sample surface, which calls for the further fabrication improvement. The result overall supports a new fabrication approach for the probe that is effective for tip-enhanced spectroscopy.

.....

keywords : Tip-enhanced near-field optical microscopy, tip-enhanced Raman scattering, tip-enhnaced fluorescence, nanostar, Au@Ag nanoparticle, plasmon

Student Number : 2014-20304

Table of Contents

1. Introduction

Spectroscopic methods with high spatial resolution combined with strong signal intensity are becoming more important for understanding chemical and physical properties of nanoscale objects. One of these methods is the tip-enhanced near-field optical microscopy (TENOM) which has been continuously developed. The TENOM (1.1) is the combination of the confocal microscopy and the atomic force microscopy (AFM). To understand basic concepts of TENOM, we first discuss how enhanced electric field appears around a metallic probe (1.1.1). Then, we are exploring the enhanced signals by the enhanced electric field in terms of the tip-enhanced Raman scattering (1.1.2.) and fluorescence (1.1.3.).

1.1. Tip-Enhanced Near-field Optical Microscopy

Tip-enhanced near-field optical microscopy (TENOM)[1,2] is a powerful optical tool capable of providing a huge signal enhancement as well as high spatial resolution. The conventional optical microscope has theoretical limitation of the instrument owing to the diffraction of the light. According to Abbe's diffraction limit,[3] Abbe's resolution, d, is expressed as below:

$$d = \frac{\lambda}{2nsin\theta} = \frac{\lambda}{2NA}$$

where d is proportional to the wavelength of illumination (λ) and inversely proportional to refractive index of the imaging medium (n) and the sine of the aperture angle ($\sin\theta$). The objective numerical aperture (NA) is defined by $nsin\theta$. If visible laser is applied to this

equation, the resolution is about 200-400 nm. It's still big to observe the material with nanometer scale. To break the diffraction limit of the light, therefore, the AFM tip is introduced into the confocal microscope. This is the TENOM. The confinement of the near-field in the vicinity of the metallic tip enable not only better resolution but also significant signal enhancement. With these things, TENOM can be put to use in every ways. In particular, Raman spectroscopy has limitations because of low intensity although it has strong points such as having molecular specific information. At this point, TENOM could be the solution. Also, for the fluorescence microscope, it will takes effect in terms of nanoimaging. In short, with the TENOM, we can get chemical compositions from the sample and nanoimaging with the sufficient signal and resolution but with the minimum damage.

1.1.1. Enhanced electric field at a metallic tip

At a metallic tip, the enhanced electric field could be explained in a lightening rod effect and a surface plasmon resonance based on metallic nanoparticles. First of all, the lightening rod is related to the geometry of the metallic tip. An electrical charge highly accumulates at the end of the sharp tip. Therefore, in the presence of the irradiation, the electric fields are the strongest at the end of the tip so that higher photon confinement in the small volume in the vicinity of the tip is possible. Next, suppose a metallic nanoparticle is attached to the AFM tip. Then, enhanced signal can be explained by the localized surface plasmon resonance (LSPR). The surface plasmon is the oscillations of localized electric field around the nanoparticle with specific frequencies. The LSPR occurs when particles are much smaller than the wavelength of the incident excitation source.[4] The

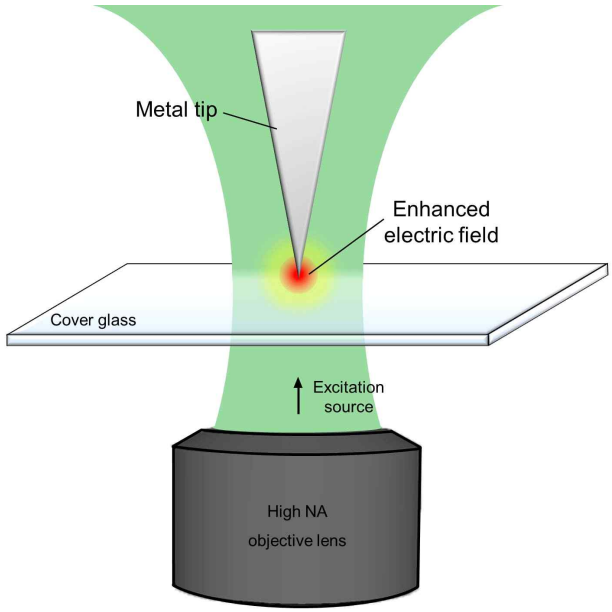

Figure 1 Schemetic enhaced-electric field at a metallic tip under the exposure of the exictation source.

shape and size of the metallic nanoparticles affect the resonant frequency of the conduction electron. Electromagnetic field of light bring the conduction electrons to excitation of the LSPR. And this causes the generation of strong electromagnetic field around the metallic nanoparticles. To sum up, the strongest electric field in the sharp tip leads to spatial confinement of the near-field in vicinity of the metallic tip. This resulted in considerable enhanced signal. Due to the spatial confinement of the near-field, in the TENOM, the enhanced field is localized in very small regions (ranging between 10-100 nm). In the confocal microscope, however, the diameter of laser when it is focused in the focal plane that means the size of effective electromagnetic field is about 300-600 nm. In other words, compared with the conventional microscope, the area of effective electromagnetic field become extremely smaller (see Figure 1). The

spatial confinement of the near-field also can be thought of in terms of the resolution of the image. Along with the AFM, the resolution is strongly correlated with the geometry of the tip in the TENOM. However, actually in the TENOM, it is more complicated since we need to take into account the enhanced field related to the geometry of the tip.

There are several factors that affect the intensity of the electric field. First, the enhanced electric field is working efficiently when the distance between tip and sample is very small.[5] A little reflection is likely to show that this is the natural consequences because the tip escaped from focal spot of laser as the tip retracted from a sample. At the focal spot, the amount that exposed to the laser at the tip is the largest. Second, we need to consider the LSPR. As mentioned above, the size, arrangement and shape of the nanoparticles at the tip make a change of the resonant frequency of the conduction electron of metallic nanoparticles. When the resonant frequency of a metallic probe and wavelength of the excitation source are well matched, the intensity of the enhanced electromagnetic field could be maximized. Note that both the geometry of the metallic nanoparticle at the tip and the wavelength of the excitation source could be considered. Lastly, the polarizaion of light has a influence. Considering the experimental setup, the AFM tip (z-direction, see Figure 1) is perpendicular aligned to the sample surface (xy-plane). Additionally, the laser is placed along the z-direction. For effective interaction between the tip and laser, the polarization of the laser must have z-direction. That's why we use radial polarizer in the confocal setup (It will be referred with more details in 2.1.2.).

1.1.2 Tip-enhanced Raman scattering

The tip-enhanced electric field leads to the tip-enhanced signal. In the case of Raman spectroscopy, it is powerful analysis tool as it provide vibration spectra (also known as fingerprints) contained molecular specific information. Unfortunately, its own scattering cross-section is very weak resulting in difficulties for analysis. To suppressing the weakness of the conventional Raman spectroscopy, tip-enhanced Raman scattering (TERS)[6-11] has been applied. Applying the strong enhanced electric field at the metallic tip to Raman spectroscopy, the intensity of the Raman signal can be enormously enhanced.

For the TERS, sample has been chosen as one-dimensional structure (eg. carbon nanotube)[6-8] or uniform coverage for flims[9] or self-assembly monolayers (SAMs).[10,11] This is because position of sample area is reflected in the signal enhancement factor. The signal enhancement factor (EF) for TERS is expressed as below:[12-14]

$$EF = \frac{I_{TERS} / N_{TERS}}{I_{Raman} / N_{Raman}}$$

where N_{Raman} and N_{TERS} are the number of probe molecules in the normal Raman and TERS signal, respectively. The I_{Raman} and I_{TERS} denote the corresponding intensity. If N_{TERS} and N_{Raman} are changed as the position of sample is chaged, it's not reasonable to compare the ratio between I_{TERS}/N_{TERS} and I_{Raman}/N_{Raman}. Therefore, sample need to have uniform coverage properties. The number of probe molecules for the normal Raman, N_{Raman}, is calculated by [(the density of probe molecule) × (diffraction limited area of the laser focal spot) × (depth of focus)] / (molecular weight of the molecule). In the case of SAMs, N_{TERS} can be expressed as follow; (surface

packing density of the SAMs) × (area of the enhanced local field). The area of the enhanced local field is determined by the FDTD simulation results.

1.1.3. Tip-Enhanced Fluorescence

In tip-enhanced fluorescence (TEF)[15-22], there are a few more things should be considered. Because of the mechanism in fluorescence that the excitation occur from the real excited electronic energy state (cf. virtual state in Raman) to ground state, the photobleaching and quenching appear. To minimize the photobleaching, the intensity of the excitation source should be diminished. Additionally, if a metallic particle is too close to probe molecules below 2 nm, quenching is dominant than spontaneous fluorescence emission. Therefore, in the case of TEF, the tip-sample distance is more critical than in the TERS and proper distance (2-10 nm) between the tip and the sample should be take into consideration (Figure 2).[23-27]

There are requirements for sample showing up TEF efficiently. The orientation and its dipole moment of probe molecules plays an important role that sample, interacting with the tip when tip is in proximity under the laser exposure.[24-26] If orientation and its dipole moment of the molecule are aligned in z-direction, enhanced signal in TEF will be maximized. But aligning the molecules in the direction we want is still exploring. With those difficulties, we just fixed the sample by spin-coating with the polymer film (eg. polymethyl methacrylate, PMMA). Then, orientation of molecules are random so we select a molecule with high enhancement among them. With polymer coating, one more merit exists that we can adjust the

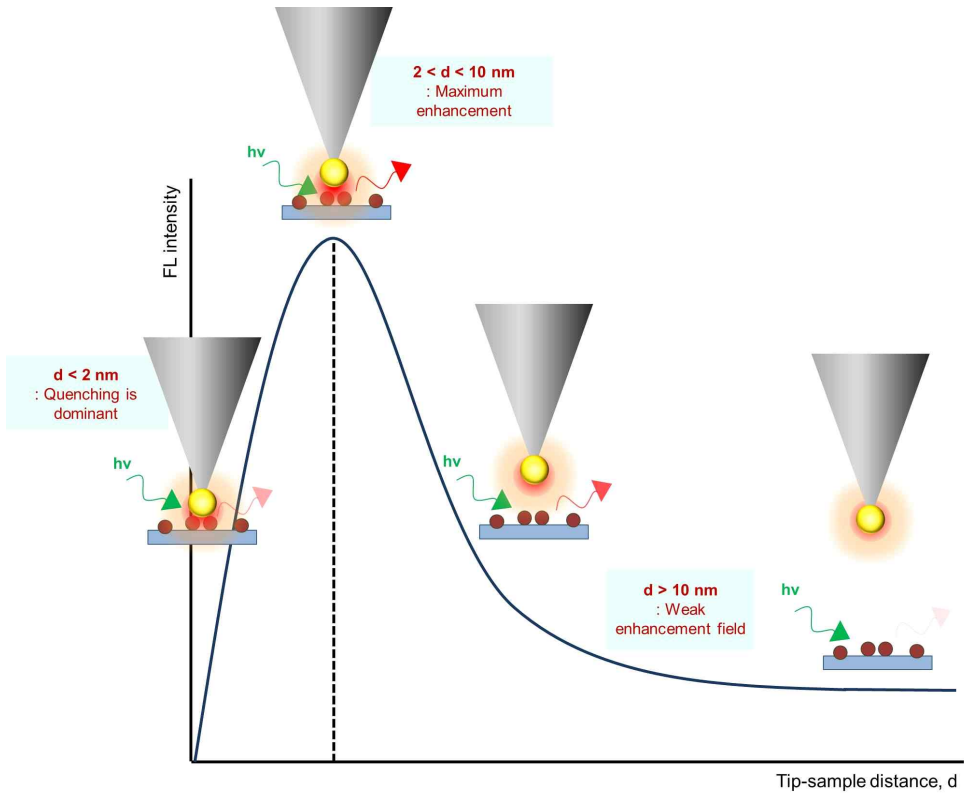

Figure 2 Fluorescence (FL) intensity as a function of the distance between the tip and the sample surface.

tip-sample distance by adjusting the thickness of the polymer film. Another sample condition is that sample ought not to have high quantum yield.[23,28,29] In the far field, the quantun yield of fluorescence $Q_0 = \Gamma/(\Gamma + k_{nr})$, while in the presence of near-field metallic nanoparticles, $Q_m = (\Gamma + \Gamma_m)/(\Gamma + k_{nr})$. The Γ is the fluorescence radiative rate, the k_{nr} is the nonradiative rates, and the Γ_m is an additional radiative rate. If the Q_0 is too high, the Γ_m will be neglected so the enhanced fluorescence signal is almost not appeared. Therefore, the sample with low quantum yield of fluorescence should be selected.

Nanostructures within the AFM tip are significant as well. In TERS, monolithic metal coated tip has been overwhelmingly used due to simplicity of the fabrication.[6-11] In TEF, however, tip with isolated structure has better local field enhancement than monolithic metal coated tip.[30] For the monolithic tip, the field enhancement is not strong to overcome the quenching owing to its structure. It becomes easier to extricate the local field from the tip-end. Besides, metal-coated tips are off-resonant with the excitation source. For the isolated nanostructure, on the other hand, the local field stayed behind its isolated structure rather than escaping from it. Also, it is fully resonant with the visible irradiation by tuning. Therefore, isolated metallic nanoparticle attached probe is preferred for TEF.

In turn, finding optimal conditions (eg. kind of the sample, design for the tip and power of laser, etc) for TEF, we can get fluorescence images with high spatial resolution and considerable enhancement.

2. Experimental setup

In this chpater, I'll explain the confocal microscope experimental setup combined with the atomic force microsopy (AFM). All of the experimental data are acquired from this setup. First, I'll explain the entire composition of the TENOM setup and how it works (2.1.). Then, I'll discuss setup in detail divided into the confocal microscopy (2.1.1.), a radial polarizer (2.1.2.) and an atomic force microscopy (2.1.3.).

2.1. Tip-Enhanced Near-field Optical Microscopy

The schematic design for the experimental setup is shown in Figure 3. To start with the irradiation of the laser with λ_{ex} = 532 nm, rays with only λ_{ex} = 532 nm passes through 532 nm line filter and other rays are blocked by this. First set of two lenses and a pinhole functions as a spatial filter. Second set of a pinhole involving the linear polarizer and the radial polarizer (Nanophoton, ZPol-532-QzM-4) will be discussed at greater length later (in the chapter 2.1.2.) for making parallel polarization beam to the tip. The dichroic mirror divided ray that half is transmitted and another half is reflected. Next two lenses are used for making 4f system to validate the confocal system. The laser goes to combined AFM (XE-120, Park Systems) and inverted microscope (IX71, Olympus). The laser is focused onto the tip through an objective lens (oil immersion, NA = 1.46), and Raman and fluorescence signals are collected through the same objective lens. Then, beam is faced with the 532 nm edge filter so only ray with λ>532 nm (Raman and fluorescence signals which

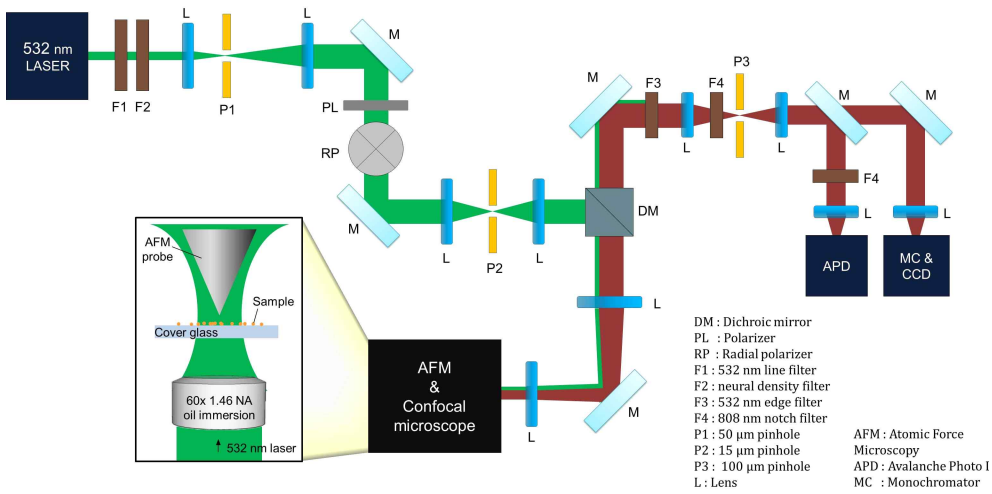

Figure 3 The experimental tip-enhanced spectroscopy setup.

we want to observe) can pass and the other is blocked. The 808 nm notch filter is blocked only the ray with λ = 808 nm from the laser involved in AFM. Third set of a pinhole also acts as spatial filter so the signal-to-noise ratio could be increased. The signal is collected to the following detectors; The avalanche photodiodes (APDs, Thorlabs) and a Raman spectrometer (Triax 320, Horiba; DU-401, Andor Tech) can be switched by a flipped mirror. We get fluorescence images by APDs and spectra by Raman spectrometer. Before using the setup, the alignment has been always checked.

2.1.1. Confocal microscopy

Confocal microscopy uses in various ways due to its high resolution images and easy operation, although it has diffraction limit of light. The invention of the confocal microscope is attributed to Marvin Minsky in 1955.[31] In Minsky's design, pinhole apertures is the

key factor to eliminate out-of-focus rays.

Confocal microsope is almost same with a conventional microscope, but main difference is that light source passes pinhole aperture with a diameter 20-100 μm hole. To understand confocal microscopy,[31,32] look Figure 4. Light is focused by a lens and then light is focused again by a following lens. Red plane indicates the signal comes from the target species located in the focal volume, source 1. In other words, a point source of light is confocal with source 1. We also see light coming from a out-of-focus that generates background signal. Blue plane is not at the focal point of the lens, so it cannot pass pinhole aperture. Consequentially, by applying pinhole, it's possible to pass selectively source 1 and reject light coming from out-of-focus like source 2. In this way, the background signal is significantly reduced compared with the conventional microscope. In addition, the resolution in depth can be considerably improved. However, the confocal microscope still has resolution limitation due to diffraction as the conventional microscope does.

We get confocal fluorescence image of nile red molecules (in the polystyrene beads with a diameter of 20 nm, Invitrogen), Figure 5A, which is appeared as small circles. A solution that was diluted with water by a factor of 10^4 times was spin-coated at 3000 rpm for 60 seconds on a glass substrate. The glass substrate treated piranha and RCA I processes before using. Resolution could be checked by line indicated in Figure 5A, white line. Line profile is appeared in Figure 5B and C. Full width at half maximum (FWHM) which means resolution is confirmed up to 250 nm. We get theoretical value by putting parameters into Abbe's diffraction limit equation, $d = \lambda/2NA$. We use light source as a laser with $\lambda = 532nm$ and oil immersion

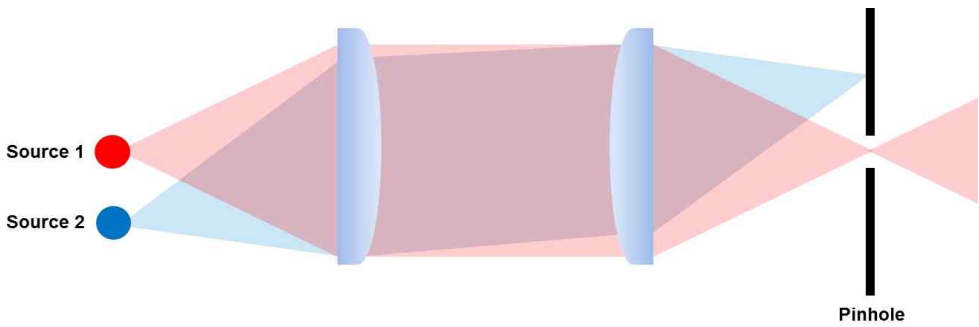

Figure 4 Source 1 (red) passed through two lenses and focuses on aperture of a pinhole. Otherwise, source 2 (blue) is blocked by a pinhole. As a result, light from only source 1 (red) makes signal by reaching a detector. Background from defocused rays such as source 2 (blue) is considerably depressed.

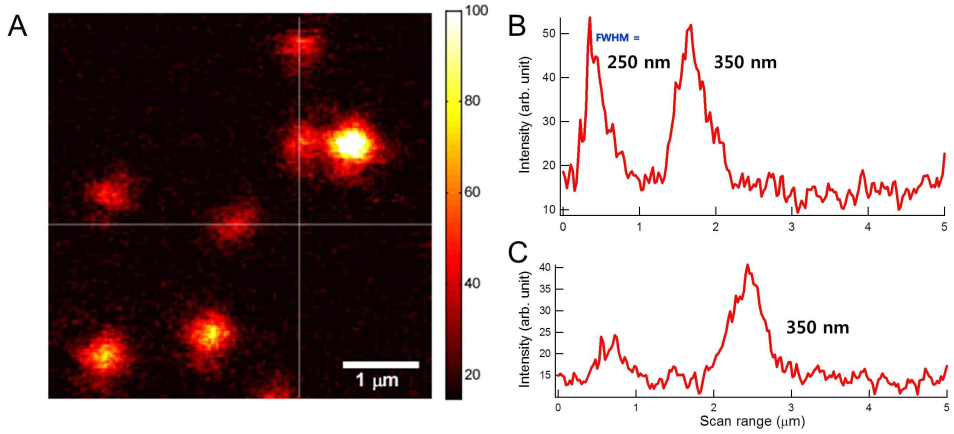

Figure 5 **A** confocal fluorescence image. Image smoothing processing is applied. In each points, the exposure time is 10 ms. The color scale bar indicates intensity of fluorescence. **B** Line profile applicable to a white parallel line in 2A. Here, FWHM is about 250, 350 nm, respectively. **C** Line profile applicable to a white vertical line in 2A. FWHM is about 350 nm.

objective lens that has $NA = 1.46$. To apply these, $d = 532/(2 \times 1.46) = 182\,nm$. Compared with experimental data, 250 nm, it is not deviate a lot. Therefore, we can confirm the size of pinhole is proper, and the confocal microscope is well operate as well.

2.1.2 Polarization mode converter

Polarization mode converter can be used in many ways, e.g. polarization Raman microscope,[34,35] surface deformations,[36] optical imaging of tautomerization,[37] and high-focusing microscopy.[38] We insert polarization mode converter into the confocal setup to use near-field microscopy that is basis for the concept of the confinement of incident light with a nanoparticle which was discussed already in chapter 1. Now, let's look at the radial polarization in detail.

First, we need to know how radially and azimuthally polarized doughnut mode (RPDM and APDM, respectively) is made. To make doughnut-mode laser beam, laser passes through a linear polarizer, a polarization mode converter[37,38] (also known as radial polarizaer), a lens, a pinhole and a lens in order (as shown in Figure 6A). The linear polarizer is an optical filter that make beam with only specific direction of vector passes. We adjust the beam through the polarizer is parallel to its reflection plane. And then, beam passes radial polarizer that consists of four segments of half-wave plate. By rotating polarization mode converter, we can make RPDM or APDM. Both two modes have doughnut-shaped intensity distribution,[38] and the pinhole (with a diameter of 15 μm) functions as a mode cleaner.[37,38]

The electric field vector in the focal plane is completely different even though both RPDM and APDM have doughnut-shaped

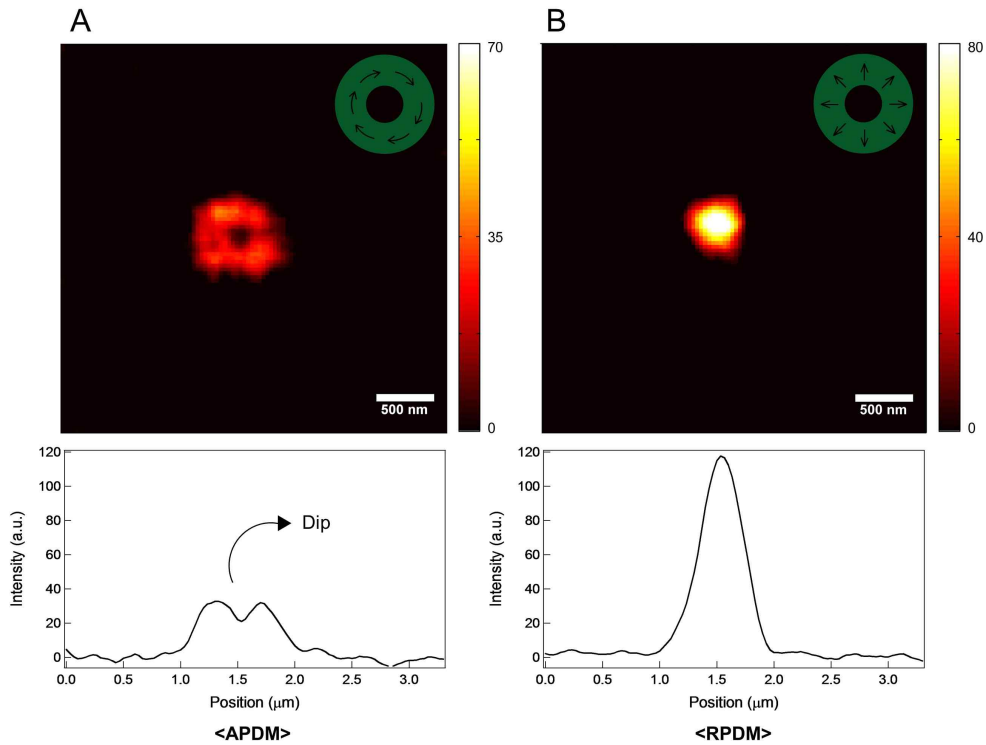

Figure 6 Fluorescence images of nile red molecules and line profiles sampled along the corresponding images when using **A** APDM and **B** RPDM, respectively.

intensity distribution. In APDM (Figure 6B), when laser is focused by high NA objective lens, only in-plane (xy) polarization component is remained in the focal plane.[34,37] This still contains doughnut mode intensity distribution in that the lateral field intensity is strictly dominant. In RPDM (Figure 6C), however, additional mode that the electric field vector in the focal plane is parallel to z-axis (longitudinal direction) is made.[34,37] Here, longitudinal components is stronger than in-plane so that the electric field intensity is the strongest at the center instead of doughnut mode intensity distribution. According to this, fluorescence image in APDM and

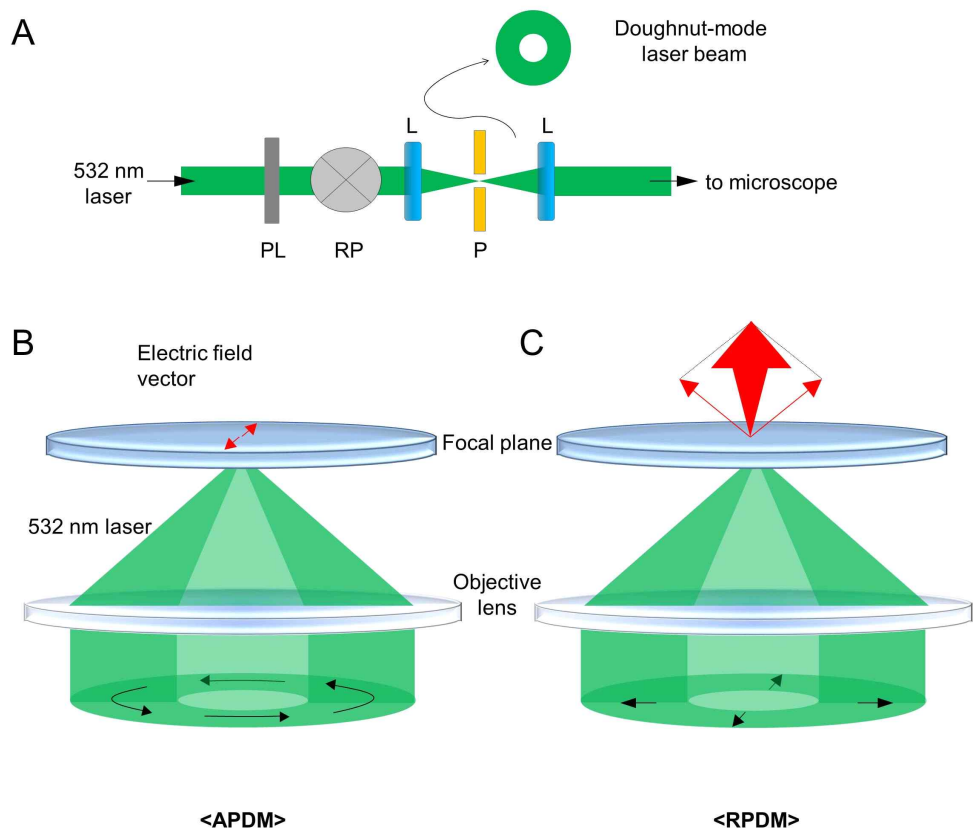

Figure 7 The polarization mode converter. **A** The partial experimental setup (PL: linear polarizer, RP: radial polarizer, L: lens, P: pinhole with a diameter of 15 μm). **B** Electric field formation in the focal plane when APDM is focused by high NA objective lens. **C** When RPDM is focused in the focal plane, direction of vector is perpendicular to the focal plane.

RPDM emerged as doughnut and filled sphere shape, respectively (Figure 7). In the line profile indicated in Figure 7A (APDM), the dip indicated with an arrow proves that the polarization mode converter works properly. In Figure 7B (RPDM), fluorescence appear as a small sphere with the higher intensity distribution at the center as expected.

2.3. Atomic Force Microscopy (AFM)

We use a near-field microscopy that is combined with the confocal microscopy involved the radial polarizer (we discussed so far in the previous sections) and an atomic force microscopy (AFM). In this section, we look through how the AFM functions.[39,40]

The AFM is measured in three dimensions, the horizontal (xy) plane and the vertical (z) plane. Resolution at z-direction up to nanoscale is normally higher than xy plane. The key principle is the beam-lever deflection method based on laser and photodiode array (Figure 8). In Figure 8A, the reflected laser from cantilever of the AFM probe is detected by a position-sensitive photodiode (PSPD). Here, deflection of cantilever can vary as topography of the sample changes. If tip is moving up and down, the laser will reach the A and B sections of the PSPD (see Figure 8B). Likewise, the laser will fluctuate between C and D sections of PSPD when the tip is moving side to side. In the case of the former, it generates AFM signal (normal force). The latter case, it generates the lateral force microscopy (LFM) signal (lateral force) and the type of image data is friction.[41]

The signal from the PSPD goes to feedback loop that controls the z-position of the probe through piezoelectric scanner connecting to the AFM probe. In our system, scanner of sample is moving to xy plane with a raster scannig, while AFM head is moving up and down (z-direction). In other words, the images of AFM are acquired by the combination of raster scanning in sample stage and height profiling in AFM.

The AFM imaging modes can be largely categorized as the contact, tapping and noncontact mode. As you can see in the Figure

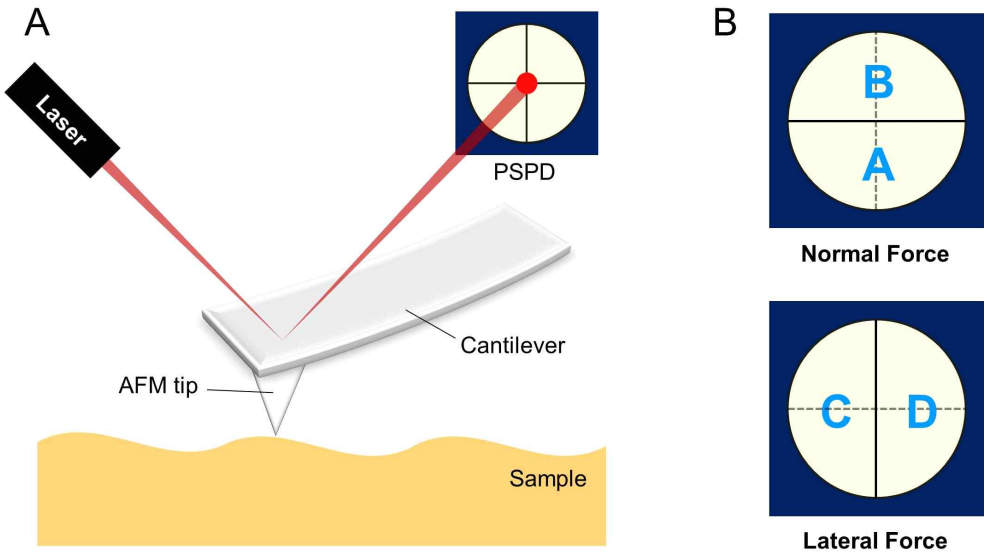

Figure 8 **A** A brief illustration how to work an AFM. **B** segments of position- sensitive photodiode (PSPD).

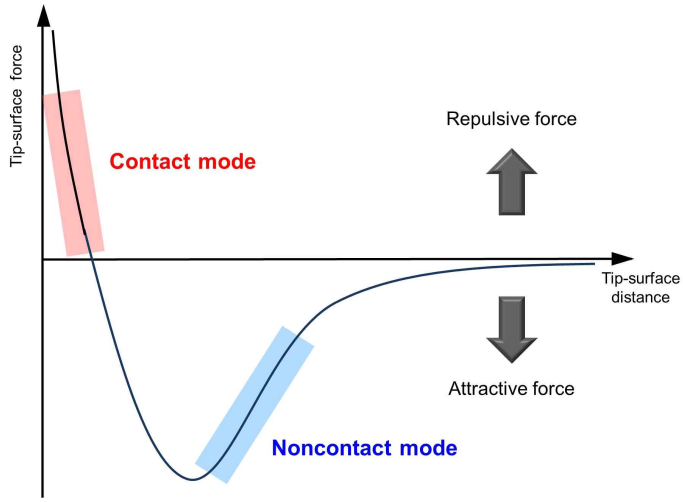

Figure 9 Interatomic force versus distance between tip and sample curve.

9, in the contact mode, the tip-surface distance is very small so a strong repulsive force appears between the tip and the surface. Constant height mode and constant force mode are included in the contact mode. For the constant height mode, variation of the cantilever deflection is related to topographic images, whereas for the constant force mode, z-direction scanner moving of tip is directly connected to topographic images and deflection of cantilever is fixed by the feedback circuit. Using contact mode can damage samples and distort image. For these reasons, contact mode is used for flat samples or for lithography using intended damage. In the noncontact mode, however, an instantaneous polarization interaction, that is to say an attractive interaction, appears. The tip is oscillated at the specific resonance frequency and the amplitude of the oscillation is kept constant. Comparing with noncontact mode and tapping mode, both are based on a feedback mechanism of constant oscillation amplitude. But amplitude of tapping mode set about 50-60% of free amplitude while that of non-contact mode set about ~100%. In conclusion, tapping mode takes advantages of two other modes and provides higher resolution images with minimum sample damage.

3. A Au Core/Ag Shell (Au@Ag) Nanoparticle Probes for Tip-Enhaced Spectroscopy

In the chapter 3 and 4, tip-enhanced spectroscopy with experimental data will be discussed in earnest. In this chapter, a new tip with a Au core/Ag shell nanoparticle (Au@AgNP) developed. And we observed the aspect that effectiveness of TERS signals as the size of the nanoparticle which is attached to the probe increases. Synthesis parts for the tip (3.1.1.) were conducted by my coworker, woong Kim who belongs in department of chemistry, Pohang university of science and technology, Korea.

3.1. Au@Ag Nanoparticle Probes

3.1.1. Preparation for Au@Ag Nanoparticle Probes

Preparation for Au@AgNP probe can be explained over a four-step. Figure 10 shows the transfer process of a single 5 nm AuNP through the differential binding forces of DNA-DNA interactions (first step).[42] The AuNPs tethering a single DNA strand with 63 bases (Oligonucleotides was purchased from IDT) for each were hybridized onto complementary DNA with 20 bases that was immobilized onto the silicon wafer surface.[43] For this, silane coupling agent, N-(3-(triethoxysilyl)-propyl)-O-polyethyleneoxide urethane (TPU, Gelest) was used to generate the underlying silane base layer. And the dendron was immobilized to the silane base layer. The AFM tip (ContGD-G for contact mode; Tap190-G for noncontact mode, BudgetSensors) tethering 40 bases DNA approached the substrate. The single strand of DNA (ss-DNA) on the tip had a base sequence

that is complementary to the single strand part of DNA attached to the 5 nm AuNP. Upon the tip-sample contact, the 40 bases DNA on the tip hybridized with the complementary part of the DNA on the substrate. The binding force between these two strands (50 pN) is stronger than the force between the substrate DNA and the AuNP-bound DNA (20 pN), so the ss-DNA and its bound AuNP was transferred from the substrate to the tip during retraction. In this work, the surfaces of the tip and the substrate were modified with dendrons (Figure 10B) that serve as lateral spacers between the neighboring DNA strands. As reported previously,[44] the dendron-modified AFM tip guarantees single molecular interaction (in our case, transfer of a single seed NP).[45] Using the procedure described above, we transferred AuNP seeds to the tips with a success rate of 70%. The TEM image in Figure 10C shows the transferred AuNP seed.

And the tip was immersed in a silver enhancing solution, which was a mixture of 200 μL of 1.0 mM $AgNO_3$ aqueous solution, and 50 μL of 1 mM sodium L-ascorbate (BioReagent, Sigma Aldrich) in phosphate-buffered saline solution (PBS, pH 7.4). While a strong reductant such as sodium borohydride ($NaBH_4$) produced silver nanoparticles at various positions on the AFM tip, sodium L-ascorbate selectively enhanced silver only on the gold particle and reduced also the nonspecific deposition of silver particles on the silicon surface of the AFM tip. Because the adhesion of the nanoparticle on the tip was weak, the detachment during the measurement was a common problem. We observed that an annealing process increased the adhesion strength. In particular, the tip was heated in air at 500℃ for 10 min (third step, Figure 11A), after enhancing the gold nanoparticle (second step) attached to the tip in the silver solution for 10 min (enhancing at the condition gave the core-shell particles of about 8 nm in size). The thermally treated tip

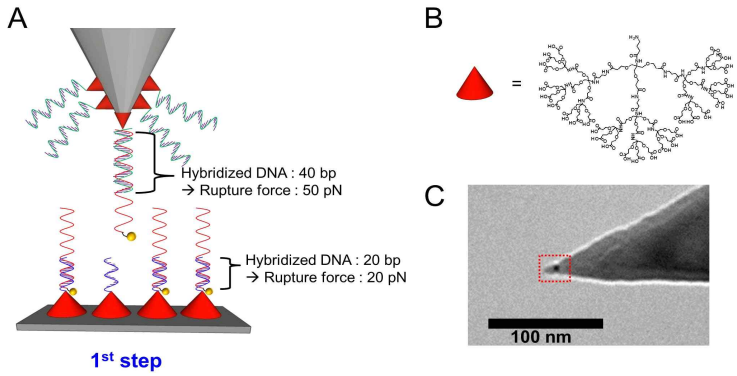

Figure 10 The first step in making Au@Ag NP probes. **A** A schematic illustrating the trasfer from the substrate to the tip of a single DNA strand tethering a AuNP. **B** Chemical structure of the dedron used for the surface modification. **C** The TEM image of a tip with a single AuNP transferred from the substrate.

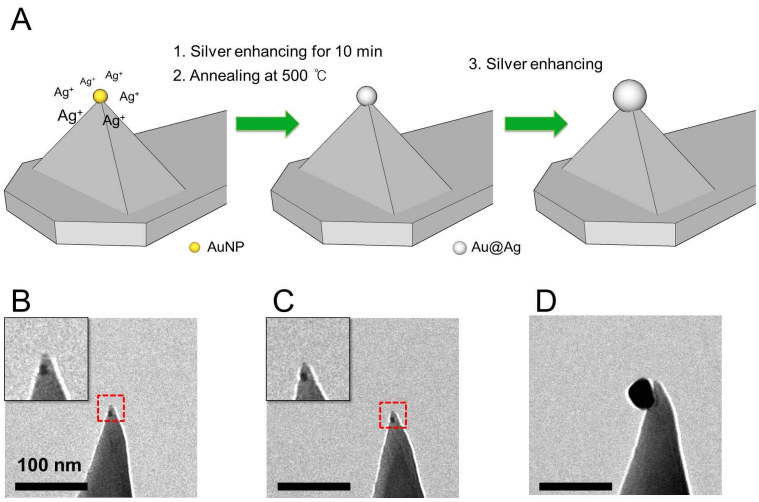

Figure 11 Preparation of the Au@Ag nanoparticle probe and the corresponding TEM images. **A** 5 nm seed AuNP is enhancing (step2) and annealing (step3) after picked up by an AFM tip. And then in a solution of AgNO3 and sodium L-ascorbate, Au@Ag particle is enhancing again (step4). **B** A TEM image of 5 nm AuNP attached to the AFM tip. **C** After enhancing and 500 ℃ annealing process, size of Au@Ag nanoparticle is 7.6±0.3 nm. **D** Final silver shell growth by placing in the silver enhancing solution in 1 h.

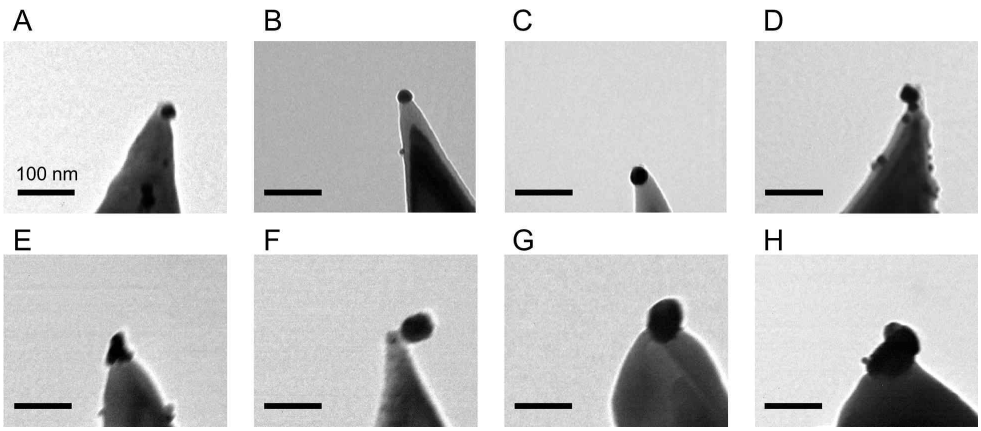

Figure 12 Representative TEM images of the Au@AgNP probes with various sizes of NPs, which are **A** 24 nm, **B** 28 nm, **C** 34 nm, **D** 40 nm, **E** 50 nm, **F** 55 nm, **G** 60, and **H** 90 nm.

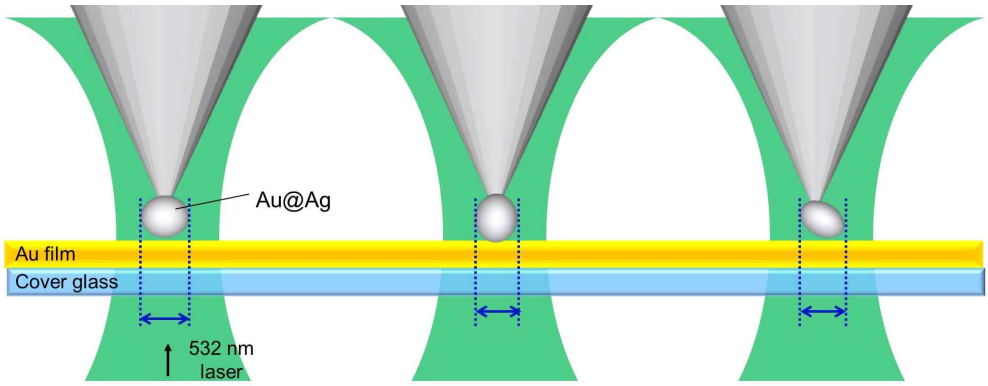

Figure 13 Approach to determine the effective size of elliptical nanoparticles with various orientations.

was immersed in the enhancing solution again (fourth step) to generate a particle of the target size. It was possible to control the size of the resulting silver particle by varying the reaction time. We find that such a four-step procedure is far more effective than a three-step (absence of annealing process) in terms of the adhesion strength of the NPs. In order to minimize the deleterious effect of the oxidized silver layer, the tip was immersed in the silver enhancing solution shortly just before the TERS measurement. We confirmed that last treatment did not induce variations of the particle size. Figure 12 displays representative TEM images of the fabricated Au@Ag probe in which the Au@AgNPs with a diameter of from 24 to 90 nm.

The Au@AgNPs are, in the most case, elliptical so final size of NPs was determined by the following approach (Figure 13). We measure the distance between the left and right ends axis parallel to the beam direction. It's pretty good way to guess the effective size. But it has a limitation that we cannot measure the actual effective size of Au@AgNPs which approaches the Au film in proximity for TERS because we don't know the accurate structure with 3-dimension in Au@AgNPs probe through the TEM images of the probes. In other words, actual effective size of Au@AgNP may differ slightly from our expectations.

3.1.2. FDTD Simulated Results of a Silver Nanoparticle

To characterize the plasmonic properties of Au@AgNP probes, we ran the FDTD simulation[46] for confirming the extinction spectra of a AgNP. Even though we use the core-shell NP probes, it play like a AgNP due to its small size of core. That's why we use AgNP model in FDTD simulations. Also we checked there are marginal

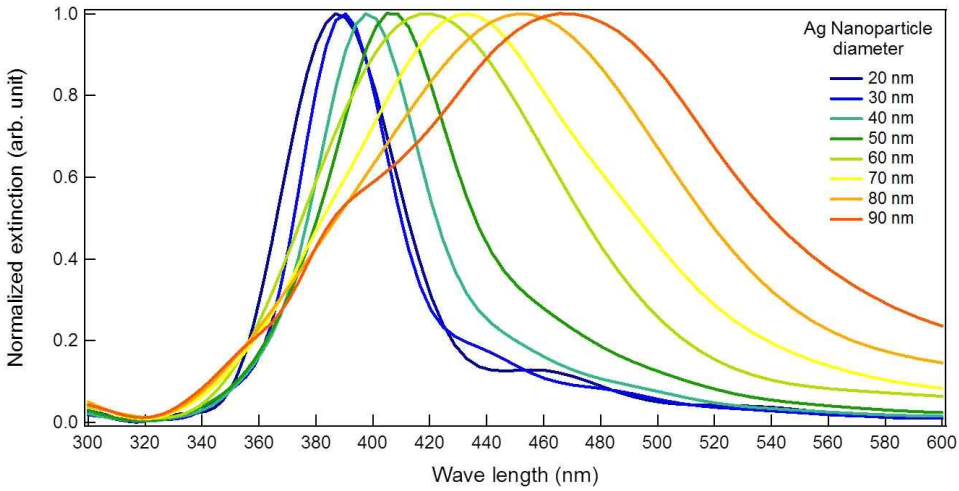

Figure 14 Simulated extinction spectra of AgNPs in accordance with the NP size from 20 to 90 nm. As size of AgNP increases, wavelength of maximum absorbance shifts to red.

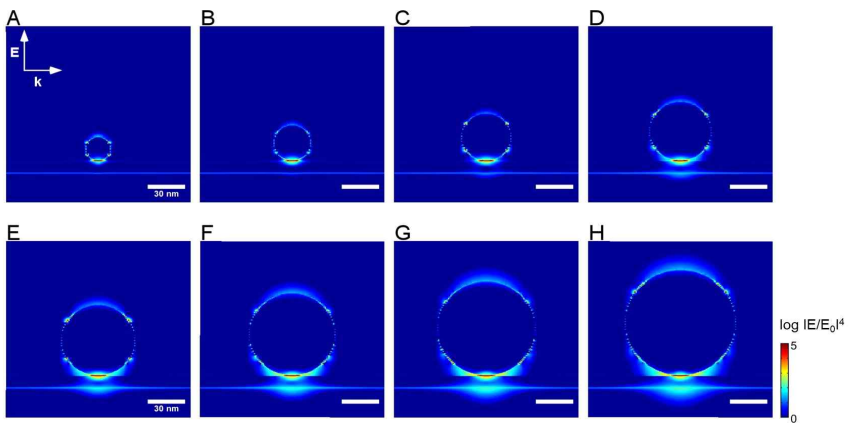

Figure 15 Simulated electric field distribution between the gold film with 10 nm thickness on glass substrate and the AgNP with **A** 20 **B** 30 **C** 40 **D** 50 **E** 60 **F** 70 **G** 80 **H** 90 nm diameter. The spacing between the gold film and AgNP is set in 0.7 nm at all occasions. The color scale bar indicates intensity of electric field which expressed as $\log|E/E_0|^4$. The E, k and the corresponding arrows represent the polarization and propagation direction of the incident light (λ_{ex} = 532 nm).

variations between Au@Ag and AgNP model. Figure 14 is the simulated extinction spectra of AgNP with size from 20 to 90 nm. The λ_{max} of the absorbance shifts to red with increasing the size of the AgNP as expected.

We can also expect enhanced electric field is much larger as size of AgNP increases since bigger size of AgNP is much well resonant with the excitation source (λ_{ex} = 532 nm). It was confirmed by simulated electric distribution[46] in Figure 15. The maximum electric field intensity which is expressed as $\log|E/E_0|^4$ showed up at the junction between AgNP and gold film. In each case, numerical value of electric field intensity ($\log|E/E_0|^4$) is 5.65, 6.36, 6.63, 6.59, 6.62, 6.70, 6.71, and 6.66 in ascending order of AgNPs size.

3.2. Sample Preparation

In Figure 16, the partial experimental setup is displayed that involved sample for TERS measurements. Clean cover glasses were coated with Au (10 nm)/Ti (2 nm) using an e-beam evaporator. Biphenyl-4-thiol (BPT, 97%, Sigama Aldrich) was dissolved in dichloromethane and diluted in ethanol (final concentration of solution: 25 mM). The Au-coated cover glasses were immersed in BPT solution for 2 hours and then it is washed out by ethanol. Finally, the self-assembled BPT monolayer was prepared on the gold-coated cover glass substrate.

3.3. TERS with regard to size of the Au@Ag nanoparticle

To check the vibration peaks of BPT in our setup, we first examined the normal Raman spectrum of the powdery BPT. Sample

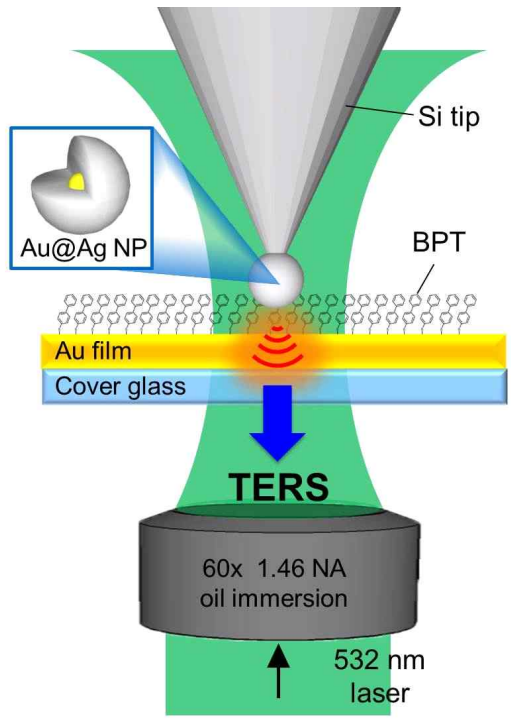

Figure 16 Partial experimental setup for TERS measurements that included sample, Self-assembled BPT monolayer on Au-coated film.

was prepared by just putting the powdered BPT on the cover glass. The spectrum for this normal Raman is shown in Figure 17. And then we carried out the TERS measurements for BPT, switching the probes with various sizes of nanoparticles. Figure 18 shows Raman spectra of the BPT sample collected without and with the tip. The spectra demonstrate the pronounced enhanced Raman peaks of BPT (Table 1; peak assignments for Raman and TERS). Intensity of enhanced Raman signals is increased as size of Au@AgNP increases. The peaks with C-H bending (1174 cm^{-1}) and ring stretching (1288, 1573 and 1585 cm^{-1}) are dominantly enhanced. Especially in the spectrum with the 60 nm of Au@AgNP probe, an extraordinary result was observed. At the wavenumber around 1000 cm^{-1}, three peaks

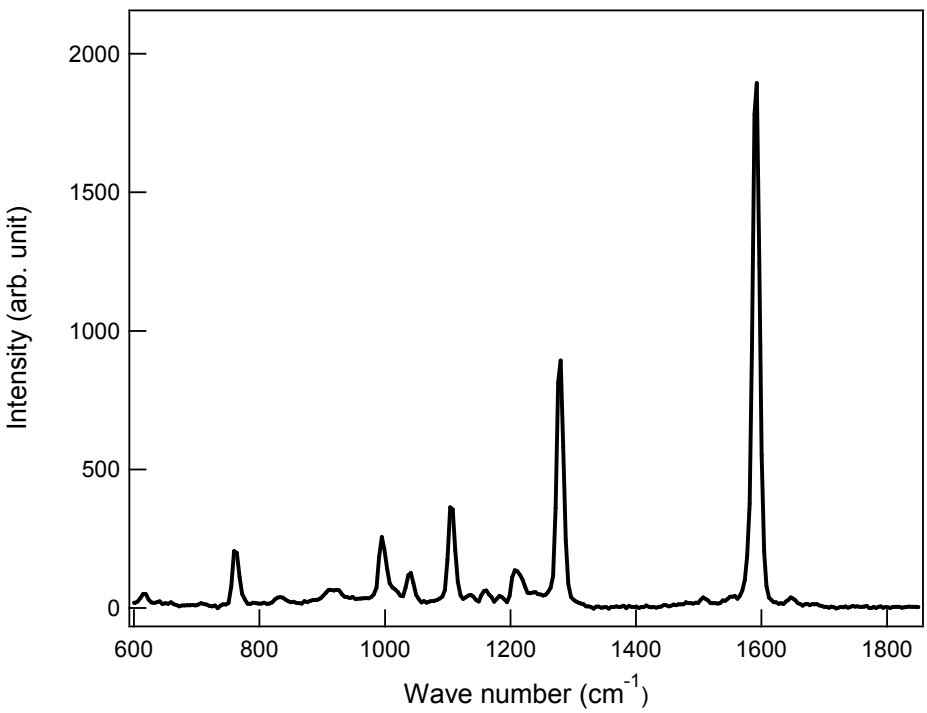

Figure 17 Raman spectrum of BPT (powder). The integration time is 180 s.

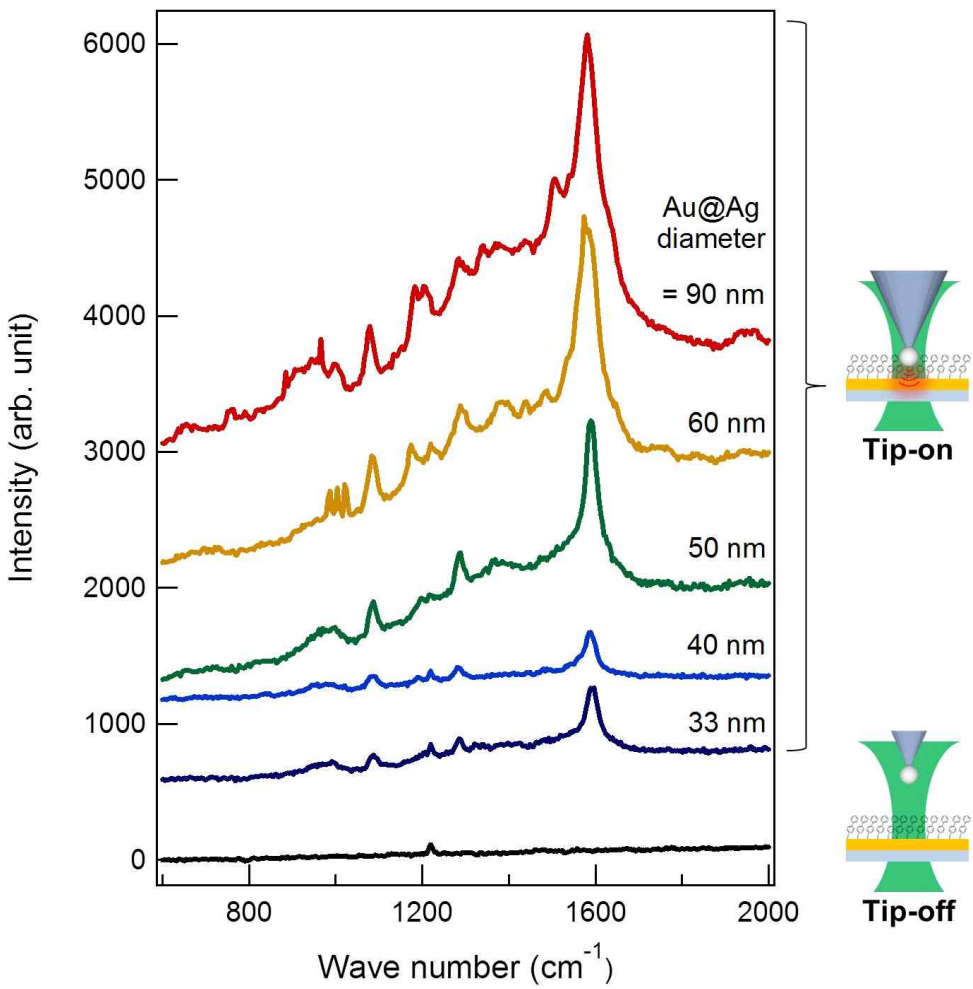

Figure 18 A set of BPT TERS spectra with the Au@AgNP-attached probes. For all cases, an identical BPT sample was examined and the laser power and exposure time are 20 μW and 180 s, respectively.

Peak No.	Normal Raman[b]	TERS	Peak assignments[c]
1	759.51	759.51	ν(S-C)
2	-	986.56	δ(C-H)
3	995	1003.4	
4	-	1020.3	
5	1103.8	1174.1	
6	1280.2	1288.3	ring ν(C=C)
7	1588.8	1573.3	
8	1592.6	1584.9	

Table 1 Peak assignments for the Raman and TERS spectra for BPT (in cm-1). Normal Raman was measured from powdery BPT. For the assignments in TERS, two spectra was employed that was acquired by using 60 and 90 nm Au@AgNP probes. Vibration peak assignments and notations[47-49] are as followed; ν: stretch, δ: bend.

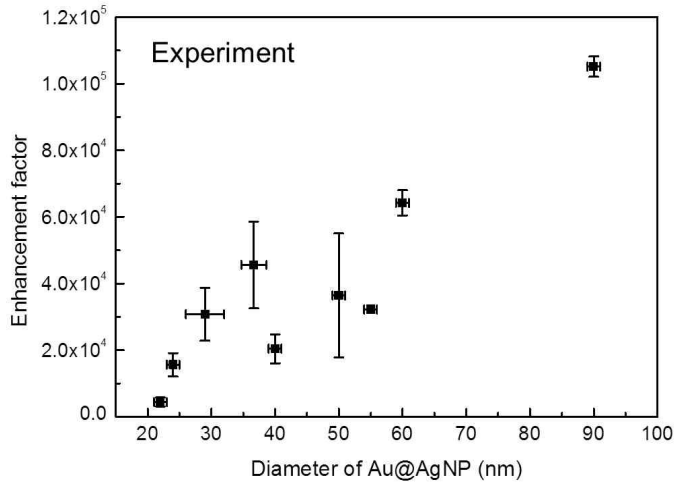

Figure 19 Plot of enhancement factor as a function of size of Au@AgNP at 1573 & 1585 cm^{-1}. In this plot, 20 sets of experimental data were used.

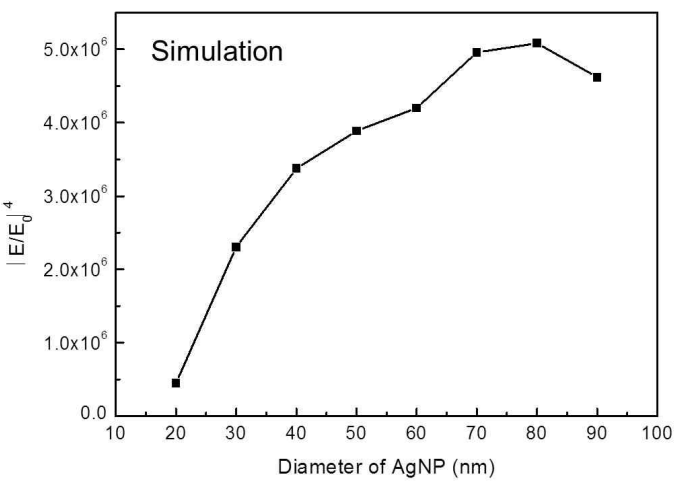

Figure 20 The simulated enhancement factor expressed as $|E/E_0|^4$ along the diameter of AgNP. The $|E/E_0|^4$ indicates the enhancement factor.

appear for the TERS even though only one peak appears for normal Raman. This implies the immense signal enhancement occurs by the 60 nm Au@AgNP probe.

Figure 19 indicates the TERS enhancement factor plotted as a function of Au@AgNP diameter at the most enhanced peaks (1585, 1573 cm^{-1}). For plotting, 20 sets of experimental data were employed. Here, we inserted x-error bar as well and the reason is to calibrate the our approach for measuring the size of Au@AgNP which was discussed in more detail in the previous chapter (3.1.1.). TERS signal shows a systematic increase with increasing size of Au@AgNP.[50-52] The simulated result (Figure 20) supports our experimental data. The dependence qualitatively agrees with the hypothesis that the nanoparticles act as point-like dipoles: within the quasi-static approximation, the dipole polarizability of a small nanosphere is $4\pi\epsilon_0 a^3(\epsilon_M-1)/(\epsilon_M+2)$, where a is the radius of the nanoparticle and ϵ_M is the dielectric function of the metal. Thus, the increase in the dipole strength and the resulting local field intensity.

3.4. Conclusions

The Au@Ag nanoparticle was synthesized selectively on a tip-end and the size of the nanoparticle can be controlled by changing the reaction time in the enhancing solution. With the TERS measurement, we have verified that such tips can be used as plasmonically active near-field probe. As Au@AgNP size is increasing, plasmonic enhancement has been shown a tendency to increase in both cases of the experimental and simulated results. We believe that the current preparation procedure can be extended to nanoparticles of various configurations that is expected to maximize the field enhancement.

4. Nanostar Probes for Tip-Enhanced Spectroscopy

We measured TERS signals and got TEF images by using nanostar probes. Likewise the chapter 3, synthesis parts for the tip (4.1.1.) were conducted by my coworker, woong Kim who belongs in department of chemistry, Pohang university of science and technology, Korea. I cite my sources of chapter 4; *Nanoscale*, 10.1039/C5NR06657C.[42]

4.1. Nanostar Probes

4.1.1. Synthesis of Nanostars and Nanostar Probes

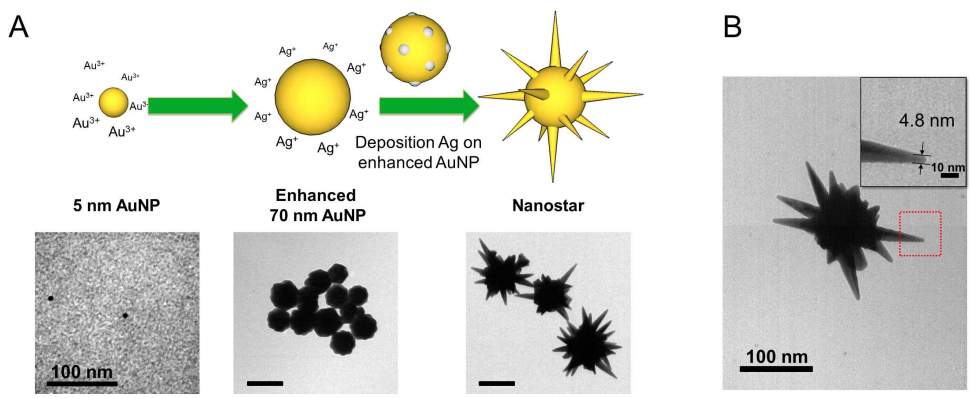

Figure 21 **A** A schematic diagram of nanostar synthesis and the corresponding TEM images of 5 nm AuNP, enhanced 70 nm AuNP and nanostar. **B** The TEM image of a nanostar. The inset shows the magnified views of the spikes of the nanostar.

Nanostars were synthesized by enhancing small seed Au nanoparticles (AuNPs, diameter of 5 nm, Ted Pella) and subsequently

forming sharp spikes on the enlarged nanoparticles as shown in Figue 21A. For the enhancement, the 100 μL of 65 nM seed solution and a 200 μL solution of 50 mM $HAuCl_4$ (99.999%, Sigma Aldrich) was mixed with 10 mL of deionized water. Next, 400 μL of 2.0 mM $AgNO_3$ solution (99.9999%, Sigma Aldrich) and 200 μL of 100 mM ascorbic acid solution (99.0%, Sigma Aldrich) was added. The resulting solution was stirred for 1-2 minutes, and the color turned from yellow to pink. The size of the seed NPs increased through the reduction of gold ions to form lager NPs with a diameter of 70 nm. Finally, the spikes were grown on top of the NPs by the reduction of gold on silver deposition sites as reported previously.[53] In Figure 21A, each images corresponding to the steps are characterized by the transmission electron microscopy (TEM, JEM-1011, JEOL). Also, in Figure 21B, we confirmed that sharp edge of the spike of the nanostar had measured 4.8 nm.

Synthesis of nanostars on the end of a scanning tip is similar to that of the colloidal nanostars described above. I'll explain the synthesis of nanostars over three steps for better understanding. Please note that actual synthesis process for second and thrid step is the one-pot procedure. First, we attach the seed NP to the tip via DNA-DNA hybridization,[43,54] and then grow nanostars *in situ*. The alternative strategy of directly attaching fully grown nanostars to the tip (either by electrostatic pickup or chemical functionalization) is unfeasible because the contact area between the nanostar and the tip is too small to provide sufficient adhesion between the nanoparticle and the tip.

The first step is that a gold nanoparticle of 5 nm in diameter was transferred to an AFM tip (See Figure 11 in chapter 3.1.1.). Next, Figure 22 schematically shows the one-pot synthetic procedure for the preparation of the nanostar probe by enhancing solution after 5 nm of a seed AuNP picked up by an AFM tip. Here's how

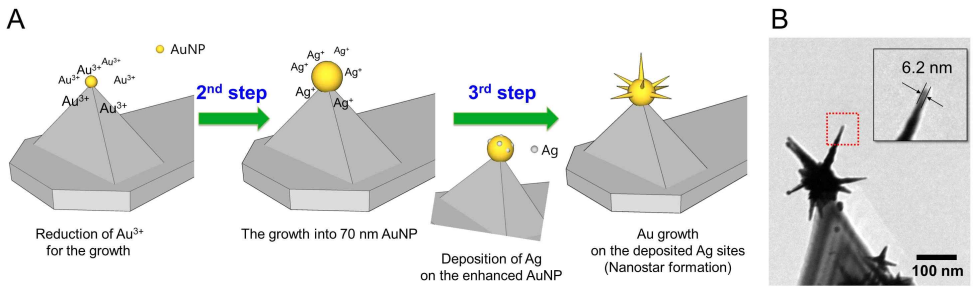

Figure 22 **A** The one-pot synthetic procedure fabricating a nanostar probe, which includes the growth of the NP (second step) and the subsequent growth of sharp spikes on the active site of the AuNP (third step). **B** TEM image of selected nanostar probe. The inset shows a magnified view of the spike.

enhancing solution was made. 20 μL of 50 mM $HAuCl_4$ and the same volume of 1.0 M HCl were added to 20 mL deionized pure water. Under vigorous stirring, 40 μL of 2.0 mM $AgNO_3$ solution and 20 μL of 100 mM freshly prepared ascorbic acid solution were added. Then, the probes were added into the solution immediately after the mixing. The yellowish color of the resulting solution changed to green after a few minutes. After the color change, the immersed probes were rinsed by deionized water to remove nonspecifically bound particles and excess chemicals. The Au^{3+} ions were reduced to make the initial nanoparticle bigger (second step, Figure 22A). For this growth step, ascorbic acid reduced Au^{3+} preferentially in the developing solution because Au ions have higher reducing potential than Ag ions ($Au^{3+}+3e^- \rightarrow Au$, 1.5 eV; $Ag^+ + e^- \rightarrow Ag$, 0.8 eV). Tiny silver particles were deposited on the surface of the enhanced AuNP through the under-potential reduction[55-58] by ascorbic acid, and the active sites of the AuNP initiated formation of gold spikes (third step, Figure 22A). It is known that the surface density of silver islands determines the number and shape of the spikes. A careful tuning of Ag^+ concentration is important for the generation of spikes with the

desired dimensions. Solutions with high Ag^{+} concentrations (>40 μM) led to very short spikes (length: 15–20 nm) and significant nonspecific growth on the tip body. Solutions of low concentration (<0.04 μM) led to no spikes on the surface of AuNP. We found that the medium concentration (4 μM) yielded nanostars with sufficiently long spikes (length = 50–80 nm), while the number of spikes was smaller than that of nanostars grown in solution. Additionally, we observed that a solution with high Au^{3+} concentration induced nonspecific formation of nanoparticles on the whole body of the AFM tip, and slow stirring resulted in nanostars with too-thin branches. The use of a dilute Au^{3+} solution (50 μM) suppressed the nonspecific growth of unwanted parts and a stirring speed of 700–800 rpm resulted in spikes with sufficient thickness (~10 nm). The procedure we employed is based on the method by Yuan *et al*,[53] but it was modified to avoid nonspecific growth. More typical procedures of nanostar generation, which involve the use of shape-directing reagents such as cetyltrimethylammonium bromide (CTAB)[59] or polyvinylpyrrolidone (PVP)[60], were not employed because such reagents tend to generate background signals in TERS and TEF measurements.

Figure 22B displays a representative TEM image of the fabricated nanostar probe in which the spikes with a radius of under 10 nm are located at the apex of the tip. Typically, ten out of 15 tips formed a nanostar at the tip apex (yield = 67%). We found that the orientation (relative angle between the axes of the tips and the spikes) of each spike was hard to control. The nanostar tips were found to have mechanical stabilities sufficient for AFM scanning. In only one or two cases out of ten, the nanostar was detached from the probe during scanning, although the TEM images obtained before and after the scanning show slight blunting and wear on the remaining nanostar.

4.1.2. Properties of the Nanostars and Nanostar Probes

4.1.2.1. Optical Properties of the Nanostars

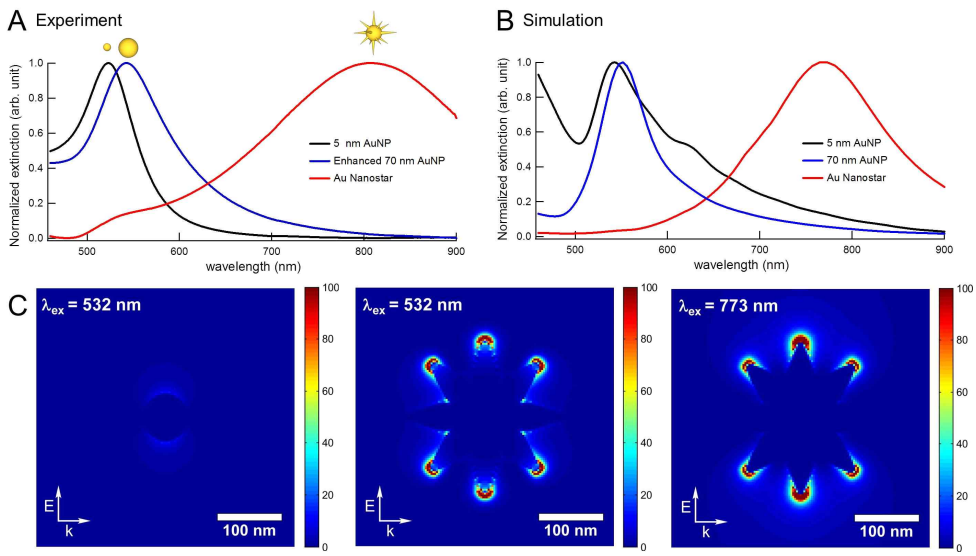

Figure 23 The optical properties of the nanostars. **A** The extinction spectra for experiment of 5 nm AuNPs (black), 70 nm AuNPs (blue), and the nanostars (red). **B** FDTD simulated scattering spectra of the corresponding nanoparticle. The λ_{max} of the nanostar is 773 nm. **C** Simulated local field distribution around the 70 nm spherical AuNP at λ_{ex} = 532 nm, the Au nanostar at λ_{ex} = 532 nm and the Au nanostar at λ_{ex} = 773 nm. The color-scale for intensity is expressed in $|E/E_0|^2$. The E,k and the corresponding arrows represent the polarization and propagation direction of the incident light.

We examined the plasmonic properties of nanostars in a colloid. The seed AuNPs with a diameter of 5 nm showed dipolar plasmon resonance at λ_{max} = 519 nm (Figure 23A, black line). The enlarged NPs showed a slightly red-shifted resonance at λ_{max} = 543 nm (Figure 23A, blue line). The Au nanostars resulted in a resonance

at λ_{max} = 809 nm (Figure 23A, red line). Such a red shift following spike enhancement is caused by the excitation of longitudinal plasmon modes in the spikes of the nanostars. Because we use the laser with wavelength, λ_{ex} = 532 nm, the dipolar plasmon of the nanostar is slightly off-resonant with the excitation source. The change in scattering spectra was fully simulated by finite-difference time-domain (FDTD) calculation,[46] as shown in Figure 23B. It showed similar aspects compared with the experiment. According to simulated electric distribution (Figure 23C), the nanostar provides strong electric field enhancement that is significantly larger than that of the spherical NP.

4.1.2.2. Mechanical Properties of the Nanostar Probes

Regarding the performance of the nanostar tip for the topographic measurement, we can see both advantage and disadvantage of it over the commercial silicon probe (PPP-NCH, Nanosensors). For the samples of small topographic contrast (for example, single molecules, graphene, or DNA chains on a flat substrate), only one spike (usually with a radius of <5 nm) on the nanostar is expected to interact with the sample, and thus the tip will provide spatial resolution that is equal to, or better than, the one obtained from the Si-tip. For the samples of large topographic contrast (for example, nanoparticles with >10 nm diameter), several differently oriented spikes on the nanostar may interact with the nanostructure concomitantly, leading to noticeable topographic convolution effect (Figure 24). In this regard, the nanostar tip is better suited for the sample of small topographic contrast.

4.2. Sample Preparation

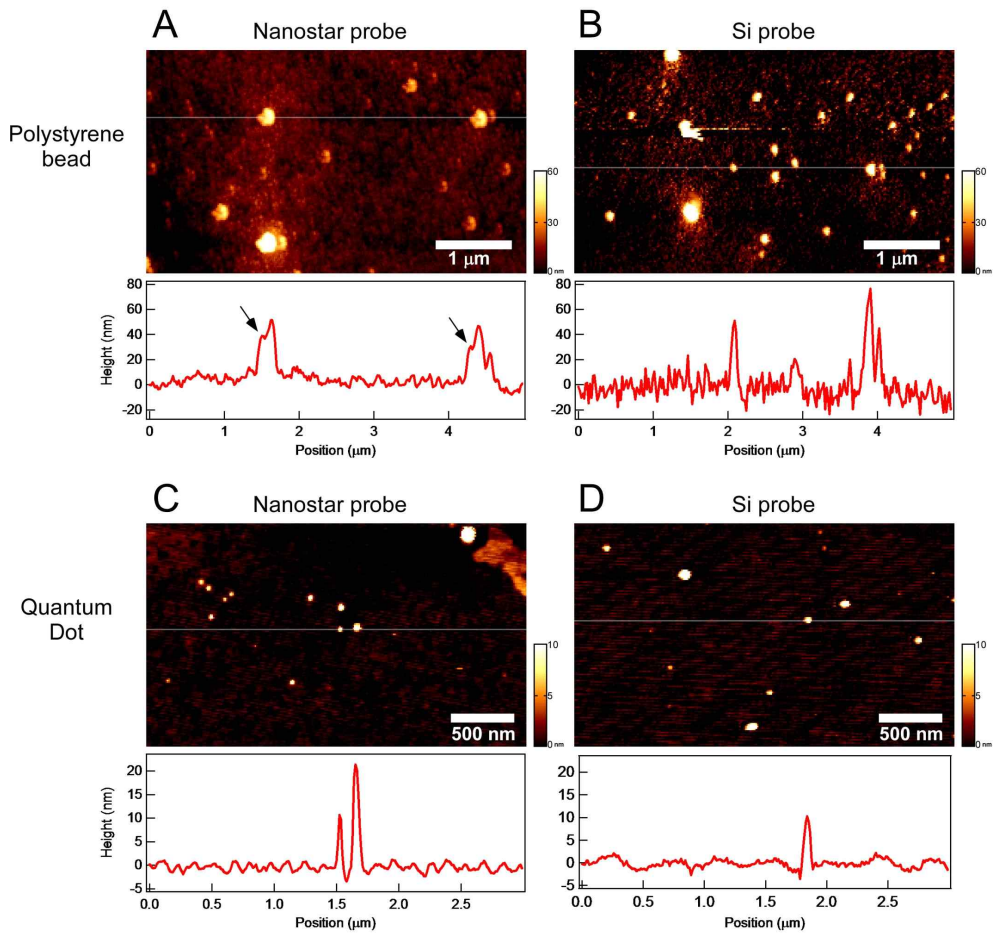

Figure 24 The AFM tapping mode topographic images of polystyrene beads (**A** and **B**, average diameter of 20 nm) and CdSe quantum dots (**C** and **D**, average diamter 5-10 nm), obtained with a commercially availabe Si-tip (**B** and **D**) and the nanostar tip (**A** and **E**). An associated profile for each images sampled along the white line is presented below of the corresponding image. The black arrows in **A** point the topographic feature arising from the tip-convolution effect.

Two types of samples are separately prepared for the TERS and TEF as indicated in Figure 25.

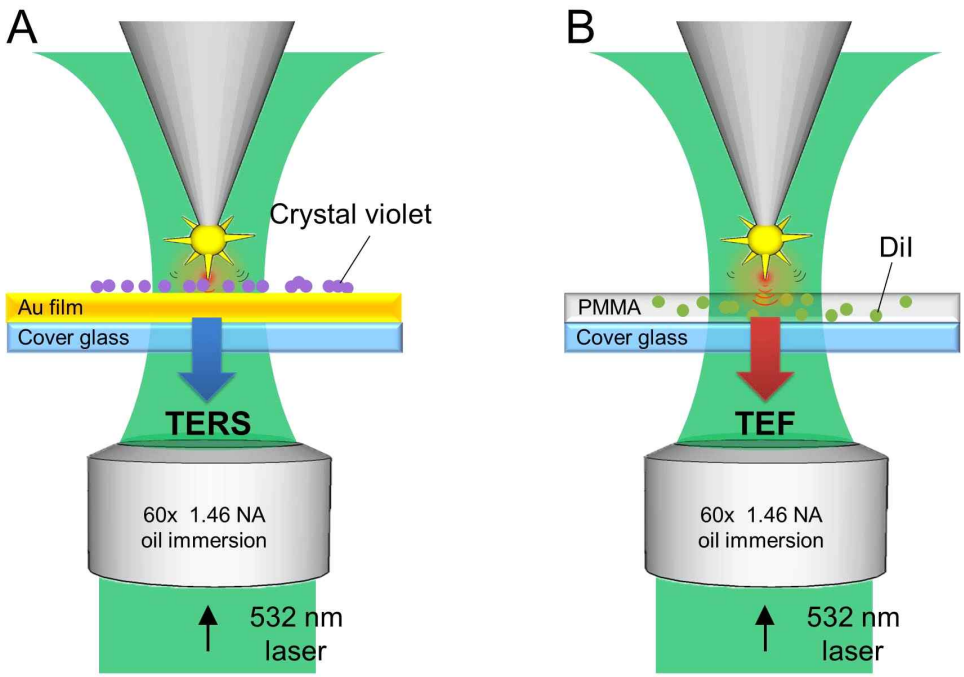

Figure 25 Two types of the samples for the TENOM. **A** CV molecules were placed on the gold-coated cover glass for the TERS measurement. **B** DiI dye embedded in a PMMA layer on the cover glass for the TEF measurement.

For the TERS measurements, clean cover galsses were coated with the Au (10 nm)/Ti (2 nm) using an e-beam evaporator. A stock solution of crystal violet (CV, 90.0%, Sigma Aldrich) was diluted in ethanol, and a drop of 10 μL was placed on the gold-coated cover glasses. The junction between Au nanostar of the probe and gold flim makes the strongest hot-spot.

For the TEF measurements, on the other hand, the poly(metyl methacrylate) (PMMA, 15000 MW, Sigma Aldrich) film is coated on

the glass. 1,1′-dioctadecyl-3,3,3′,3′-tetramethylindocarbocyanine perchlorate (DiI, Sigma Aldrich) dye molecules[61] are embedded in the PMMA film. The PMMA coating was conducted for the following reasons; ① to adjust the distance between the AFM tip and dye molecules, ② to immobilize the dye molecules, and ③ to prevent the photobleaching of the fluorescent. Accordingly, to make the proper thickness of the PMMA film for TEF, we need to find the proper concentration of the PMMA. After many trials and errors (Figure 26), we can get a linear plot that the thickness of the film for PMMA as a function of the concentration of the PMMA in Figure 16E. The thickness is measured the following procedure; First, we had scanned 5×5 μm area of the PMMA sample with commercial silicon tip by contact mode. Then, film was scratched out within the scanned area. Next, we scanned larger area, 10×10 μm with same tip but by tapping mode. That area involves all part of scratched area so we can confine the thickness of the film by comparing the height contrast. As a result, 0.5 mg/mL (PMMA/toluene) of the PMMA concentration is used and at this time the thickness of film is under 2 nm. This concentration of PMMA is made by adding 1 mL of the PMMA solution to the 20 μL of 10^{-8} M DiI solution. DiI solution was prepared in DMSO and diluted in toluene before using. Then, a drop of 20 μL solution was placed on a cover glass that had been cleaned by Piranha and RCA I processes. With a spin coater (Spin-1200, MIDAS System) at 3000 rpm for a 60 seconds, a thin layer with under 2 nm of thickness of PMMA flim was formed.

We need to check some requirements for sample to show TEF. The quantum yield of DiI is small value as 0.07 in methanol. Also, absorption wavelength of DiI dye is resonant with the wavelength of the excitation source (in our setup, λ_{ex} = 532 nm). Maximum excitation/emission wavelength of DiI dye are 549/565 nm, respectively. Taken together, DiI dye is good candidate for TEF.

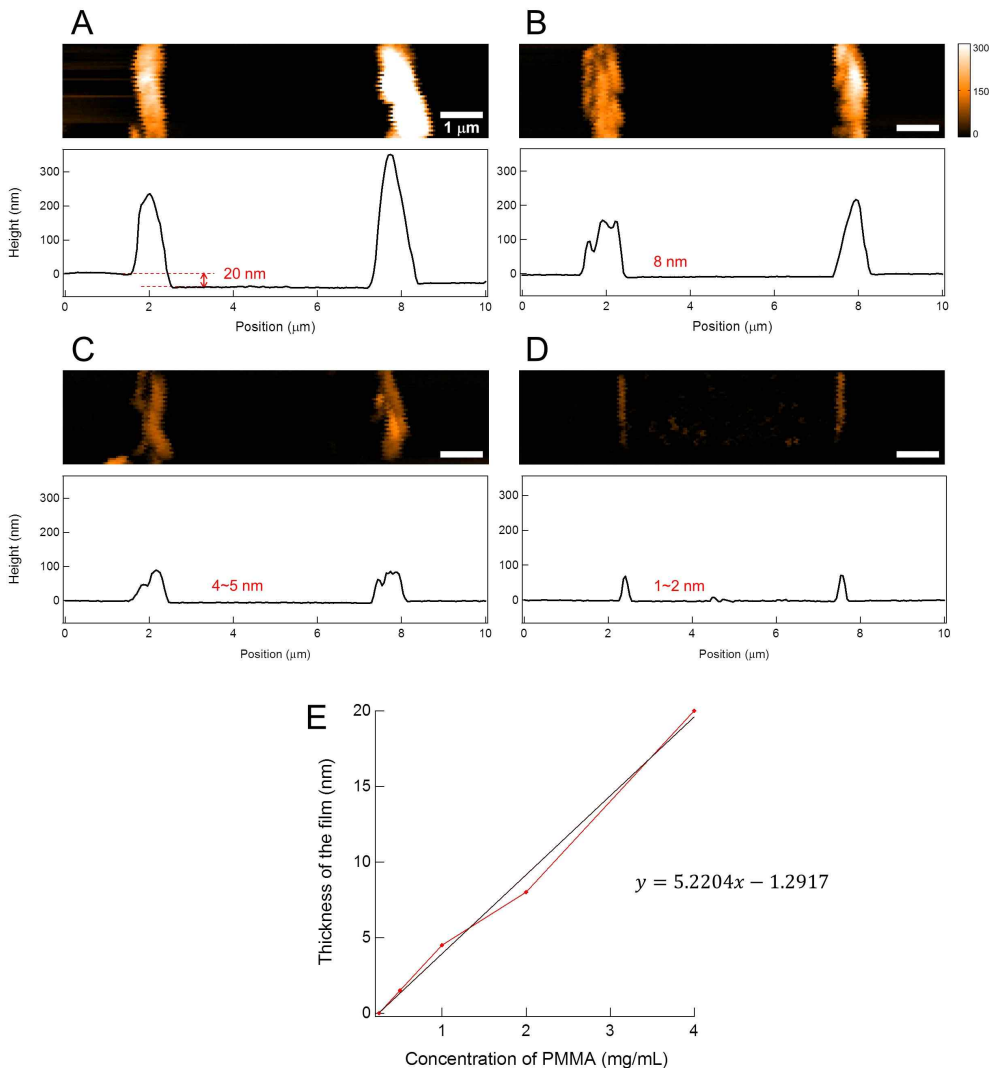

Figure 26 The measurement of the PMMA film thickness. The topographic images and the corresponding line profile in the concentration of the PMMA with **A** 4 mg/mL, **B** 2 mg/mL, **C** 1 mg/mL and **D** 0.5 mg/mL in toluene solution. **E** The linear plot that the thickness of the polymer film as a function of the concentration of PMMA.

4.3. Tip-Enhanced Raman Scattering

For the TERS measurement, the contact mode in the AFM was used to approach as close to the surface of the sample as possible. To check the experimental conditions for TERS, we got two spectra with the tip by time intervals. And we are keeping an eye on aspect of the intensity change in Raman peaks. With regard to two consecutive TERS spectra, less than 20% of decrease in TERS signal was observed under exposure to 80 μW of laser power (Figure 27). This fact supports that the TERS experimental condition (power of laser, integration time) is reasonable for the TERS measurements. Figure 28 shows Raman spectra of the CV sample collected with and without the tip. The spectra demonstrate the pronounced enhancement of eight major peaks of CV (see Table 1 for the peak assignments). For the particular spectra shown, the ratio of peak intensity with (I) and without (I_0) tip is ~10 as determined by the area of the peak at 804 cm^{-1} (I/I_0 = 215/20). Note that I_0 also contains a SERS signal of CV arising from the hotspots on Au surfaces. We found that the ratio varied from 2 to 10 for different tips, yet all of the tips showed TERS activity.

The control experiment was conducted to establish a standard how efficiently the signal of TERS exerts. For fhe control, the AFM tip had been coated with the Au film (40 nm)/Ti (1 nm) by the e-beam evaporation. Raman spectra with and without the Au-coated tip is shown in Figure 29. For comparison, the experimental conditions are set equal to those of the experiment with the nanostar probe. In the control experiment, the ratio of peak intensity at 804 cm^{-1} with and without tip is 1.38 (= 121/88). Compared to that of the nanostar, it is very small value but TERS activity is appeared though.

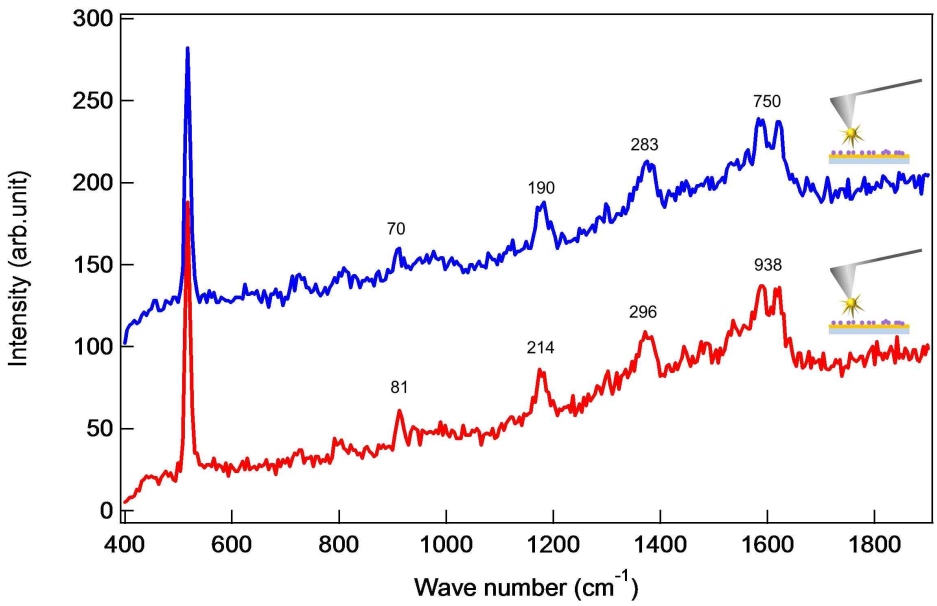

Figure 27 The two consecutive TERS spectra (red→blue) of CV on the gold surface obtained from the same tip and the same position in the sample (each with 10 seconds of integration time and 80 μW of the laser power). We observe less than 20% of decrease in TERS signal. For the clarity, the second spectrum is displaced along y-axis. Numbers in the spectra indicate the integrated area of each peaks.

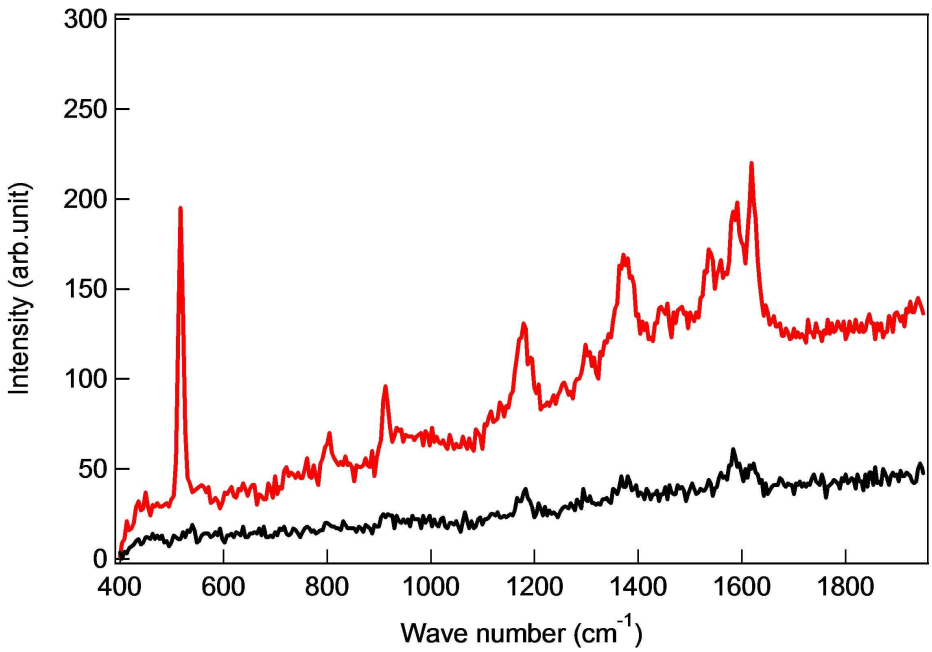

Figure 28 TERS spectra of crystal violet (inset in figure) with (red) and without (black) the nanostar tip. Laser power and exposure time were 80 μW and 10 seconds, respectively. Major vibration modes of CV are indicated with vertical lines and wavenumbers. The asterisk(∗) points to the Si-phonon mode of the tip.

Peak No.	Raman	TERS	Peak assignments[a]
1	-	804	$\gamma_{as,\,oop,\phi-H}$
2	-	912	
3	1183	1178	$\nu_{as,\,ip,\,C-H,C-\phi}$
4	1367	1367	$\nu_{as,\phi-C-\phi,C-N}$
5	1380	1387	ω
6	1536	1536	
7	1583	1591	
8	1622	1618	

Table 2 Peak assignments for the Raman and the TERS spectra for the crystal violet[b] (in cm^{-1})

a) All of the confocal Raman and TERS spectra were obtained with λ_{ex} = 532 nm.

b) Vibrational peak assignments and notations.[62-65]

γ : bend, as: antisymmetric, oop: out-of-plane; ν : stretch; ip : in-plane;

ω : ring breathing.

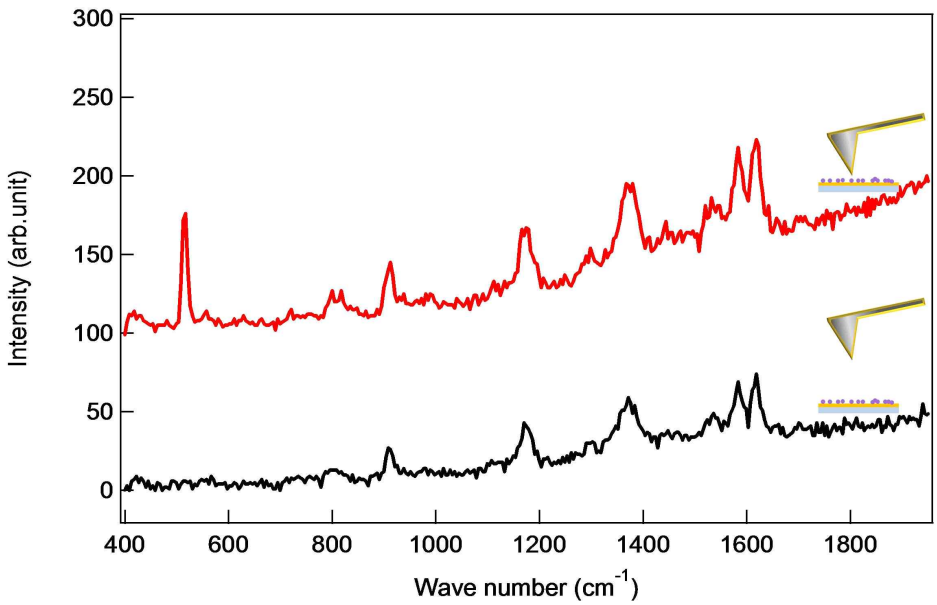

Figure 29 The control experiment for TERS spectra of crystal violet with (red) and without (black) the Au-coated probe (the thickness of Au is 40 nm). Laser power and exposure time were 80 μW and 10 sec, as same as in the experiment with the nanostar probe.

4.4. Tip-Enhanced Fluorescence

In the TEF experiment, the laser power was controlled to less than 200 nW in order to avoid photobleaching. Figures 30A-E compare TEF images of the DiI sample with the tip engaged with the surface (Figure 30; first row, tip-on) and with images with the tip retracted (Figure 30; second row, tip-off). Two features are evident from the comparison. First, the tip-on images show significantly enhanced signal intensity and spatial resolution of 90-200 nm compared with the tip-off images showing diffraction-limited spot sizes of 300-400 nm.

There are some facts are worthy of notice. During the TEF scanning, spikes on the nanostar probe often became blunt, possibly due to mechanical deformation by the tapping mode feedback with the sample surface. Nevertheless, the nanostar probes maintained a constant level of enhancement during several hours of usage. Second, we found that the degree of the enhancement varied from one molecule to another, with the observed optical enhancement varying from 5 times to 10^2 times within the same sample. For example, only one spot out of the two in the images in Figure 30D shows significant tip-enhancement (the lower bound for enhancement is 100 as determined by the Gaussian fitting of the line-profiles of the same TEF spot with and without the tip). Such variation may originate from different orientations of DiI molecules[25,26,66] and the variability in the tip-molecule distance.[23-27] Certainly, the nanostar tip produced images of individual DiI spots as the superposition of a diffraction-limited Gaussian point-spread function (psf) with a sharp tip-enhnaced psf (see Figure 30E). Therefore, for the Figure 30A and E, two Gaussian functions were used for one spot in order to model the enhanced (narrow) and unenhanced (broad) components of fluorescence from DiI spot. The images obtained with a monolithic

Au-coated tip (thickness of 10 nm), on the other hand, showed only a diffraction-limited psf with a sharp dip (see Figure 30F) by the Au-surface of the tip indicating tip-induced fluorescence quenching instead of tip-enhancement (compare Figure 30E and F).

As recently confirmed experimentally by Maouli et al,[29] the tip with isolated nanostuctures show better local field enhancement than the tips monolithically coated with gold or silver. This difference originates from the fact that the extended cone-structures associated with metal-coated tips are largely off-resonant with the excitation light, whereas the isolated nanostructures are fully resonant (dipolar plasmons) with the visible radiation. The ideal cone-shaped TERS tips should in theory provide extreme field enhancement, yet in reality such geometry is hardly achieved in typical experiments. In particular for the TEF measurement, there exists surface-induced quenching competing against the fluorescence enhancement caused by the local field enhancement. The quenching rate for the nanostar and coated tips will be similar. For the monolithic tip, the field enhancement is insufficient to overcome the fluorescence quenching, whereas for the nanostar tip, the enhancement is sufficient. This is why we observe a dip (quenching) in the TEF images obtained with the coated tip (Figure 30F).

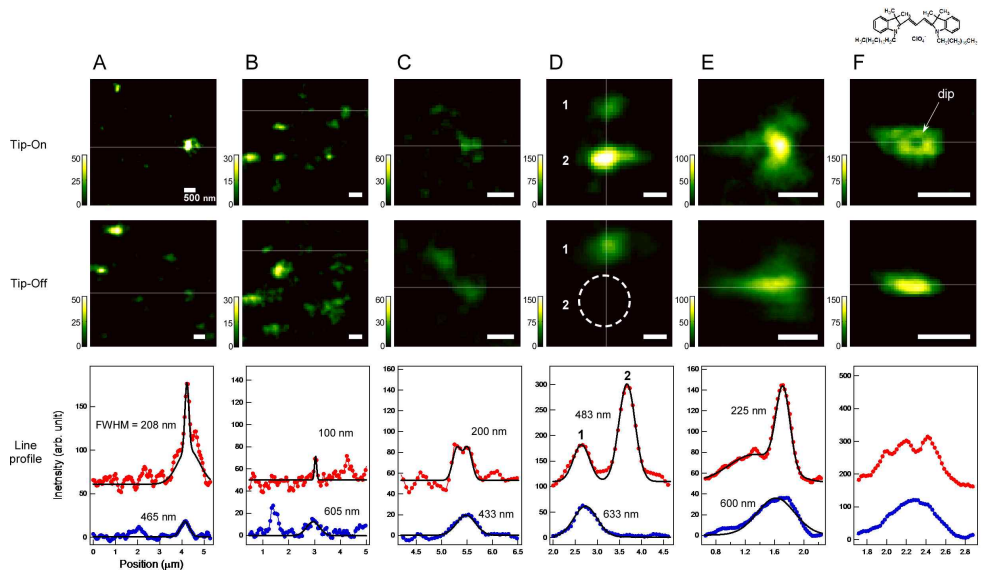

Figure 30 TEF images of DiI sample wih (tip-on) and without (tip-off) the nanostar probe. The images were obtained from the same sample at different position. For each of the data set, different probes were used except for **A** and **E**. **A-E** show the representative TEF images (with and without the tip) and line profiles (red: tip-on, blue: tip-off) sampled along the lines indicated in the corresponding images. **F** The TEF images obtained with a Au-coated tip. The tip-on and tip-off line profiles are offset in y-axis for the better visibility of the data. The fits to the Gaussian functions (black solid curves) are also shown.

4.5. Conclusions

For the nanostar probe and its performance for TERS and TEF showed that the current approach is viable for TENOM, although there still exists room for further improvement of the nanostar tip and their application. First of all, the nanostar tips showed large tip-to-tip variations in nano-optical properties, which we believe originated from the dispersion of the nanostar shape and the variation in spike orientation. The structural imperfections as well as the resonance characteristics because the dipolar plasmon of the nanostar is not optimally resonant with the excitation wavelength, may have contributed to the marginal spatial resolution (~100 nm) and the field enhancement observed in TERS and TEF. With further refinement of the structure or use of more appropriate excitation wavelength, we will be able to optimize the field enhancement. By carefully tuning the growth steps, the plasmonic properties of nanostars can be further optimized, or different shapes of nanoparticles (such as octahedrons or cubes) can be grown at the end of the tip. Such size and shape fine-tuning will help improve the performance of the tip for improved mechanical stability, signal enhancement, and spatial resolution in TERS and TEF. Besides the plasmonic properties of the tip, the properties of the sample (molecules and substrate) will influence the spectroscopic enhancement. For the TERS measurement, the enhancement will be influenced by the tip-sample distance and the local morphology of the substrate (note that our substrate has a finite roughness.). For the TEF measurement, we use the PMMA matrix to immobilize the target molecule. The finite thickness of the PMMA layer, as well as the random orientation of the molecule, will cause the variation in fluorescence enhancement through the variation in tip-molecule distance. Currently, we are exploring ways to improve such

variabilities of sample/substrates, as well as the plasmonic properties.

Above all, the majority of the nanostar probes showed local field enhancement with high spatial resolution that were useful for TERS and TEF measurement. The current probes, however, still have limitation for the effectiveness of the TENOM. Extended investigation of such probes promises deeper understanding of the optical phenomena and fabrication of more effective probes.

References

1. A. Hartschuh, *Angew. Chem. Int. Edit*, 2008, **47**, 8178 -8191.
2. N. Mauser and A. Hartschuh, *Chem. Soc. Rev.*, 2014, **43**, 1248-1262.
3. Lipson, Lipson and Tannhause, Optical Physics., *United Kingdom: Cambridge.*, 1998, 340.
4. Katherine A.Willets, Richard P. Van Duyne, *Annu. Rev. Phys. Chem.*, 2007, **58,** 267 - 297.
5. Neil Anderson, Pascal Anger, Achim Hartschuh, Lukas Novotny, *Nano Lett*, 2006, **6**, 4, 744-749.
6. Chi Chen, Norihiko Hayazawa, Satoshi Kawata, *Nat. Commun.*, 2014, **5**, 3312
7. Luiz Gustavo Canc¸ado, Achim Hartschuh, Lukas Novotny, *J. Raman Spectrosc.*, 2009, **40**, 1420-1426.
8. Jun Yu, Yuika Saito, Taro Ichimura, Satoshi Kawata, Prabhat Verma, *Appl. Phys. Lett.*, 2013, **102**, 123110.
9. N. Kumar, B. Stephanidis, R. Zenobi, A. J. Wain, D. Roy, *Nanoscale*, 2015, **7**, 7133 - 7137.
10. Noriko N. Horimoto, Shigeru Tomizawa, Yasuhiko Fujita, Shinji Kajimoto, Hiroshi Fukumura, *Chem. Commun.*, 2014, **50**, 9862-9864.
11. Gennaro Picardi, Marc Chaigneau, Razvigor Ossikovski, Christophe Licitra, Guillame Delapierre, *J. Raman Spectrosc.*, 2009, **40**, 1407-1412.
12. Yu Liu, Shuping Xu, Haibo Li, Xiaoguang Jian, Weiqing Xu, *Chem. Commun.*, 2011, **47**, 3784 - 3786.
13. Debdulal Roy, Jian Wang, Craig Williams, *J. Appl. Phys.*, 2009, **105**, 013530.
14. Wenyu Tao, Aiwu Zhao, Henghui Sun, Zibao Gan, Maofeng Zhang, Da Li, Hongyan Guoa, *RSC Adv.*, 2014, **4**, 3487-3493.
15. Lukas Novotny, Niek van Hulst, *Nature Photonics*, 2011, **5**, 83-90.
16. Anshuman Singh, Gaetan Calbris, Niek F. van Hulst, *Nano Lett.*, 2014, **14**, 8, 4715-4723.
17. Christiane Ho¨ppener, Ryan Beams, Lukas Novotny, *Nano Lett.*, 2009, **9**,

2, 903-908.
18. Jordan M. Gerton, Lawrence A. Wade, Guillaume A. Lessard, Z. Ma, Stephen R. Quake, *PRL*, 2004, **93**, 18, 180801.
19. Hadi Eghlidi, Kwang Geol Lee, Xue-Wen Chen, Stephan Go¨tzinger, Vahid Sandoghdar, *Nano Lett.*, 2009, **9**, (12), 4007-4011.
20. Mathieu Mivelle, Thomas S. van Zanten, Lars Neumann, Niek F. van Hulst, Maria F. Garcia-Parajo, *Nano Lett.*, 2012, **12**, 11, 5972-5978.
21. Palash Bharadwaj, Ryan Beams, Lukas Novotny, *Chem. Sci.*, 2011, **2**, 136-140.
22. Palash Bharadwaj, Pascal Anger, Lukas Novotny, *Nanotechnology*, 2007, **18,** 044017.
23. A. I. Dragan, C. D. Geddes, *Phys. Chem. Chem. Phys.*, 2011, **13**, 3831-3838.
24. W. E. Moerner, David P. Fromm, *Rev. Sci. Instrum.*, 2003, **74**, 8, 3597.
25. Sergei Ku¨hn, Ulf Ha°kanson, Lavinia Rogobete, Vahid Sandoghdar, 2006, *PRL*, **97**, 017402.
26. Pascal Anger, Palash Bharadwaj, Lukas Novotny, *PRL*, 2006, **96**, 113002.
27. J. Azoulay, A. D´ebarre, A. Richard, P. Tch´enio, *Europhys. Lett.*, 2000, **51,** 4, 374-380.
28. Anatoliy I. Dragan, Chris D. Geddes, *Appl. Phys. Lett.*, 2012, **100**, 093115.
29. Phil Holzmeister, Enrico Pibiri, Ju¨rgen J. Schmied, Tapasi Sen, Guillermo P. Acuna, Philip Tinnefeld, *Nat. Commun.*, 2014, **5**, 5356.
30. Imad Maouli, Atsushi Taguchi, Yuika Saito, Satoshi Kawata, Prabhat Verma, *Appl. Phys. Express*, 2015, 8, 032401.
31. Minsky. M, *Scanning.*, 1988, 10, 128-138.
32. Rober H Webb, *Rep. Prog. Phys.*, 1996, **59**, 427-471.
33. D. Semwogerere, E.R.Weeks, Confocal Microscopy, in: Encyclopedia of Biomaterials and Biomedical Engineering., *Taylor&Francis.*, 2005.
34. Yuika Saito, and Prabhat Verma, *J. Phys. Chem. Lett.*, 2012, **3**, 1295-1300.

35. Toshihiro Mino, Yuika Saito, Hiroyuki Yoshida, Satoshi Kawata, Prabhat Verma, *J. Raman spectrosc.*, 2012, **43**, 2029-2034.
36. Hidekazu Ishitobi, Issei Nakamura, Taka-aki Kobayashi, Norihiko Hayazawa, Zouheir Sekkat, Satoshi Kawata, Yasushi Inouye, *ACS photonics.*, 2014, **1,** 3, 190-197.
37. Anna M. Chizhik, Regina Ja¨ger, Alexey I. Chizhik, Sebastian Ba¨r, Hans-Georg Mack, Marcus Sackrow, Catrinel Stanciu, Alexey Lyubimtsev, Michael Hanack, Alfred J. Meixner, *Phys. Chem. Chem. Phys.*, 2011, **13**, 1722-1733.
38. R. Dorn, S. Quabis, G. Leuchs, *Phys. Rev. Lett.*, 2003, **91**, 233901.
39. Franz J. Giessibl, *Rev. Mod. Phys.*, 2003, **75**, 3, 949-983.
40. Nader Jalili, Karthik Laxminarayana, *Mechatronics*, 2004, **14**, 907 - 945.
41. Veeco Instruments Inc, MultiMode SPM Instruction Manual, 2004, NanoScope Software Version 5, 38-65.
42 W Kim, N Kim, JW Park, ZH Kim, *Nanoscale*, 2016, **8**, 987-994.
43. D. Kim, N. K. Chung, J. S. Kim and J. W. Park, *Soft Matter*, 2010, **6**, 3979-3984.
44. Y. J. Jung, B. J. Hong, W. Zhang, S. J. B. Tendler, P. M. Williams, S. Allen and J. W. Park, *J. Am. Chem. Soc.*, 2007, **129**, 9349-9355.
45. P. Hinterdorfer and Y. F. Dufrene, *Nat. Methods*, 2006, **3**, 347-355.
46. Lumerical Solutions, http://www.lumerical.com/
47. J. Kalbacova, R. D. Rodriguez, V. Desale, M. Schneider, I. Amin, R. Jordan and D. R. Zahn, *Nanospectroscopy*, 2014, **1**, 12 - 18.
48. G. Socrates, Infrared and Raman characteristic group frequencies: tables and charts, *Ltd WJS*, 2001, 245.
49. Y. R. Lee, M. S. Kim and C. H. Kwon, *Bull. Korean Chem. Soc*, 2013, **34**, 470-474.
50. W. H. Park and Z. H. Kim, *Nano Lett.*, 2010, **10**, 4040-4048.
51. K. Kim, H. B. Lee and K. S. Shin, *Spectrochim. Acta A*, 2013, **100**, 10-14.
52. K. Kim and K. S. Shin, *Anal. Sci.*, 2011, **27**, 775-783.
53. H. K. Yuan, C. G. Khoury, H. Hwang, C. M. Wilson, G. A. Grant and

T. Vo-Dinh, *Nanotechnology*, 2012, **23**, 075102.
54. K. Liu, Y. Song, W. Feng, N. N. Liu, W. K. Zhang and X. Zhang, *J. Am. Chem. Soc.*, 2011, **133**, 3226-3229.
55. C. J. Orendorff and C. J. Murphy, *J. Phys. Chem. B*, 2006, **110**, 3990-3994.
56. M. Z. Liu and P. Guyot-Sionnest, *J. Phys. Chem. B*, 2005, **109**, 22192-22200.
57. M. Grzelczak, J. Perez-Juste, P. Mulvaney and L. M. Liz-Marzan, *Chem. Soc. Rev.*, 2008, **37**, 1783-1791.
58. R. Michalitsch, B. J. Palmer and P. E. Laibinis, *Langmuir*, 2000, **16**, 6533-6540.
59. T. K. Sau and C. J. Murphy, *J. Am. Chem. Soc.*, 2004, **126**, 8648-8649.
60. L. Lu, A. Kobayashi, K. Tawa and Y. Ozaki, *Chem. Mater.*, 2006, **18**, 4894-4901.
61. M. Mivelle, T. S. van Zanten and M. F. Garcia-Parajo, *Nano Lett.*, 2014, **14**, 4895-4900.
62. H. Masuhara and S. Kawata, *Nanophotonics: Integrating Photochemistry*, Optics and Nano/bio Materials Studies. Elsevier, 2004, 132-138.
63. S. Sunder and H. Bernstein, *Can. J. Chem.*, 1981, **59**, 964-967.
64. M. Volny, A. Sengupta, C. B. Wilson, B. D. Swanson, E. J. Davis and F. Turecek, *Anal. Chem.*, 2007, **79**, 4543-4551.
65. S. L. Kleinman, E. Ringe, N. Valley, K. L. Wustholz, E. Phillips, K. A. Scheidt, G. C. Schatz and R. P. Van Duyne, *J. Am. Chem. Soc.*, 2011, **133**, 4115-4122.
66. S. Kuhn and V. Sandoghdar, *Appl. Phys. B*, 2006, **84**, 211-217.

Abstract (in Korean)
나노입자 탐침을 이용한 탐침증강 분광법

나노크기 물체의 화학적·물리학적 특성을 연구하기 위해서 소량의 분자에서의 화학적 정보와 높은 공간 분해능을 가지는 광학이미지는 필수적이다. 이런 관점에서 탐침 증강 근접장 광학 현미경(TENOM)은 높은 공간 분해능을 제공할 뿐만 아니라 탐침 끝 부분에서의 플라즈모닉 향상에 의해 신호의 세기가 강하기 때문에 촉망받고 있다. 이는 다시 말하자면, 탐침 증강 근접장 광학 현미경은 탐침의 장 향상과 공간 한정에 결정적으로 의존한다는 것을 의미한다. 그래서 우리는 보다 나은 탐침의 광학적 성질을 찾기 위해서 다양한 종류의 탐침을 이용해서 향상된 광학 신호를 받는 탐구를 진행하였다.

탐침 증강 근접장 광학 현미경을 적용하기 위해, 우리는 532 nm 파장을 가지는 방사상으로 편광된 빛이 포함된 공초점 현미경과 탐침이 탑재된 원자간력 현미경(AFM)을 사용하였다. 실험 구성 장비의 유효성을 점검하기 위해 우리는 먼저 탐침에 평행한 방향(z축)으로 편광을 만들어 주는 방사형 편광기를 테스트하였다. 방사형 모드와 순환형 모드에서 나일 레드(이는 폴리스타이렌 비드 안에 들어있으며, 비드의 지름은 20 nm)의 형광 이미지를 얻음으로써 레이저의 방향이 z축에 평행함을 확인할 수 있었다. 그 다음으로 탐침 증강 라만 산란(TERS)과 탐침 증강 형광(TEF)에 대한 실험이 수행되었으며, 이는 비슷한 방식으로 합성된 두 가지 유형의 특별한 방법으로 제작된 탐침을 이용하였다.

우리의 실험 구성 장비가 탐침 증강 라만 산란과 탐침 증강 형광 측정에 적합한지 확인하기 위해서, 우리는 금 입자를 중심으로 조절된 두께로 은 껍질의 구조를 가지는 나노 입자를 탐침을 사용하였다. Au@Ag 탐침의 합성을 위해 금 나노 입자를 DNA-DNA 상호작용에 의해 집어 올리고, 은 용액에서 성장하는 과정이 시행되었다. 탐침 증강 라만 산란 측정을 위해서 Au@Ag 탐침(나노 입자 크기: 22-90 nm)과 함

께 샘플로는 금 필름 위에 바이페닐 싸이올(BPT)로 구성된 자가 조립 단층(SAM)이 준비되었다. 우리는 이러한 탐침이 높은 플라즈모닉 장 향상을 보임을 확인하였고, 이는 나노 입자의 크기가 증가할수록 분명하게 드러났다.

더 나아가서, 우리는 중심 지름이 70 nm에 뾰족한 가지 부분의 길이가 50 nm에서 80 nm가 되는 금속 나노스타로 구성된 새로운 주사 탐침을 개발하였다. 접근 방법은 탐침 픽업 과정과 은 이온의 존재 하에 아스코르브산과 함께 금 이온이 환원되면서 나노스타의 뾰족한 가지 부분이 자라는 성장과정이 포함된다. 나노 스타 탐침은 그 뾰족한 끝 부분에 의해 좁은 부위에 향상된 전자기장을 만든다. 우리는 거의 모든 탐침이 탐침 증강 라만 산란과 탐침 증강 형광에 대해서 100 배까지의 신호 향상과 더불어 100 nm 이하의 광학 해상도를 가짐을 확인하였다. 이는 탐침 증강 형광 분광법에서는 DiI 염료, 탐침 증강 라만 산란 분광법에서는 크리스탈 바이올렛(CV)으로 실험하였다. 그러나 현재의 탐침은 커다란 탐침에 대한 가변성을 보였고, 이는 샘플 표면에 대하여 나노 스타의 뾰족한 가지 부분의 축 방향을 조절할 수 없기 때문에 나타났을 것이다. 추후에 제조 방법에 있어서 개선이 요구되는 바이다. 이 결과는 전반적으로 탐침 증강 분광법에 효율적인 새로운 탐침 제조에 대한 접근법을 뒷받침해준다.

이학석사 학위논문

나노입자 탐침을 이용한 탐침증강 분광법

Nanoparticle Probes for Tip-Enhanced Spectroscopy

2016년 2월

서울대학교 대학원

화학부 물리화학

김 나 라

Abstract

Nanoparticle Probes for Tip-Enhanced Spectroscopy

NARA KIM
Department of Chemistry
The Graduate School
Seoul National University

For exploring chemical and physical properties of nanoscale objects, chemical information of single molecule and optical images with high spatial resolution is imperative. In this regard, tip-enhanced near-field optical microscopy (TENOM) is an evolving field having extensive potential. Because it provides higher spatial resolution as well as the electric field enhancement at the tip-end. This means, in other words, plasmonic enhancement and spatial confinement within the tip are critically connected to the enhanced optical signal. Therefore, we explored enhanced optical signals with various kinds of the probes to find the optimal plasmonic properties of the probes.

To apply the TENOM, we use a confocal microscopy with a radially polarized light at 532 nm wavelength and an atomic force microscopy (AFM) fitted with the tip. To check the validation of our experimental setup, we first examined the radial polarizer which generates the polarization component of a laser at 532 nm parallel to the tip (z-aixs). By getting fluorescence images of nile red (in polystyrene beads with a diameter 20 nm) in both radial and azimuthal mode, we were convinced that polarization of laser was parallel to the z-axis in the focal plane. And then, experiments for tip-enhanced Raman scattering (TERS) and fluorescence (TEF) were

conducted with two types of special fabricated probes which were synthesized in a similar way.

In order to guarantee the our setup is available for the TERS and TEF measurements, we used a nanoparticle - a Au core/Ag shell nanoparticle (Au@AgNP) with a controlled thickness of shell - attached probe. For the synthesis of Au@AgNP probe, a seed Au nanoparticle (NP) is picked up by DNA-DNA interaction and enhanced with a silver solution were employed. For the TERS measurement, the self-assembled biphenyl-4-thiol (BPT) monolayer on Au film as the sample was employed with the Au@AgNP (size: 20-90 nm) probe. We find that such tips show high plasmonic field enhancement and this reveals clearly as size of NPs increases.

For a further study, we developed a scanning probe with a metallic nanostar (a core diameter of ~70 nm and spike lengths between 50 nm and 80 nm). The approach involves AuNP pickup process and growth of spikes through reduction of Au^{3+} with ascorbic acid in the presence of Ag^{+}. The nanostar probe makes the narrow enhancement field on account of its sharp edge. We find that nearly all of the tips show the local field enhancement up to 100-fold with an improved optical resolution below 100 nm for TERS and TEF was confirmed. These were evaluated with DiI dye for TEF and crystal violet for TERS. The current probe, however, shows large tip-to-tip variability, which may arise from the uncontrolled orientation of the apexes of the spike with respect to the sample surface, which calls for the further fabrication improvement. The result overall supports a new fabrication approach for the probe that is effective for tip-enhanced spectroscopy.

.....

keywords : Tip-enhanced near-field optical microscopy, tip-enhanced Raman scattering, tip-enhnaced fluorescence, nanostar, Au@Ag nanoparticle, plasmon

Student Number : 2014-20304

Table of Contents

1. Introduction

Spectroscopic methods with high spatial resolution combined with strong signal intensity are becoming more important for understanding chemical and physical properties of nanoscale objects. One of these methods is the tip-enhanced near-field optical microscopy (TENOM) which has been continuously developed. The TENOM (1.1) is the combination of the confocal microscopy and the atomic force microscopy (AFM). To understand basic concepts of TENOM, we first discuss how enhanced electric field appears around a metallic probe (1.1.1). Then, we are exploring the enhanced signals by the enhanced electric field in terms of the tip-enhanced Raman scattering (1.1.2.) and fluorescence (1.1.3.).

1.1. Tip-Enhanced Near-field Optical Microscopy

Tip-enhanced near-field optical microscopy (TENOM)[1,2] is a powerful optical tool capable of providing a huge signal enhancement as well as high spatial resolution. The conventional optical microscope has theoretical limitation of the instrument owing to the diffraction of the light. According to Abbe's diffraction limit,[3] Abbe's resolution, d, is expressed as below:

$$d = \frac{\lambda}{2nsin\theta} = \frac{\lambda}{2NA}$$

where d is proportional to the wavelength of illumination (λ) and inversely proportional to refractive index of the imaging medium (n) and the sine of the aperture angle ($\sin\theta$). The objective numerical aperture (NA) is defined by $nsin\theta$. If visible laser is applied to this

equation, the resolution is about 200-400 nm. It's still big to observe the material with nanometer scale. To break the diffraction limit of the light, therefore, the AFM tip is introduced into the confocal microscope. This is the TENOM. The confinement of the near-field in the vicinity of the metallic tip enable not only better resolution but also significant signal enhancement. With these things, TENOM can be put to use in every ways. In particular, Raman spectroscopy has limitations because of low intensity although it has strong points such as having molecular specific information. At this point, TENOM could be the solution. Also, for the fluorescence microscope, it will takes effect in terms of nanoimaging. In short, with the TENOM, we can get chemical compositions from the sample and nanoimaging with the sufficient signal and resolution but with the minimum damage.

1.1.1. Enhanced electric field at a metallic tip

At a metallic tip, the enhanced electric field could be explained in a lightening rod effect and a surface plasmon resonance based on metallic nanoparticles. First of all, the lightening rod is related to the geometry of the metallic tip. An electrical charge highly accumulates at the end of the sharp tip. Therefore, in the presence of the irradiation, the electric fields are the strongest at the end of the tip so that higher photon confinement in the small volume in the vicinity of the tip is possible. Next, suppose a metallic nanoparticle is attached to the AFM tip. Then, enhanced signal can be explained by the localized surface plasmon resonance (LSPR). The surface plasmon is the oscillations of localized electric field around the nanoparticle with specific frequencies. The LSPR occurs when particles are much smaller than the wavelength of the incident excitation source.[4] The

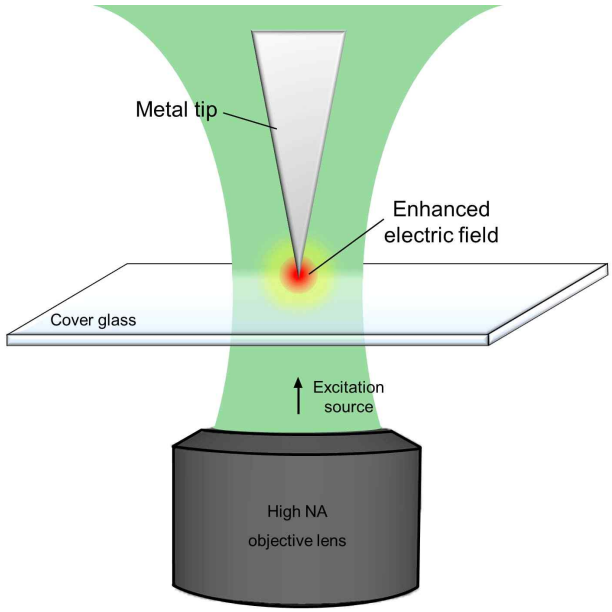

Figure 1 Schemetic enhaced-electric field at a metallic tip under the exposure of the exictation source.

shape and size of the metallic nanoparticles affect the resonant frequency of the conduction electron. Electromagnetic field of light bring the conduction electrons to excitation of the LSPR. And this causes the generation of strong electromagnetic field around the metallic nanoparticles. To sum up, the strongest electric field in the sharp tip leads to spatial confinement of the near-field in vicinity of the metallic tip. This resulted in considerable enhanced signal. Due to the spatial confinement of the near-field, in the TENOM, the enhanced field is localized in very small regions (ranging between 10-100 nm). In the confocal microscope, however, the diameter of laser when it is focused in the focal plane that means the size of effective electromagnetic field is about 300-600 nm. In other words, compared with the conventional microscope, the area of effective electromagnetic field become extremely smaller (see Figure 1). The

spatial confinement of the near-field also can be thought of in terms of the resolution of the image. Along with the AFM, the resolution is strongly correlated with the geometry of the tip in the TENOM. However, actually in the TENOM, it is more complicated since we need to take into account the enhanced field related to the geometry of the tip.

There are several factors that affect the intensity of the electric field. First, the enhanced electric field is working efficiently when the distance between tip and sample is very small.[5] A little reflection is likely to show that this is the natural consequences because the tip escaped from focal spot of laser as the tip retracted from a sample. At the focal spot, the amount that exposed to the laser at the tip is the largest. Second, we need to consider the LSPR. As mentioned above, the size, arrangement and shape of the nanoparticles at the tip make a change of the resonant frequency of the conduction electron of metallic nanoparticles. When the resonant frequency of a metallic probe and wavelength of the excitation source are well matched, the intensity of the enhanced electromagnetic field could be maximized. Note that both the geometry of the metallic nanoparticle at the tip and the wavelength of the excitation source could be considered. Lastly, the polarizaion of light has a influence. Considering the experimental setup, the AFM tip (z-direction, see Figure 1) is perpendicular aligned to the sample surface (xy-plane). Additionally, the laser is placed along the z-direction. For effective interaction between the tip and laser, the polarization of the laser must have z-direction. That's why we use radial polarizer in the confocal setup (It will be referred with more details in 2.1.2.).

1.1.2 Tip-enhanced Raman scattering

The tip-enhanced electric field leads to the tip-enhanced signal. In the case of Raman spectroscopy, it is powerful analysis tool as it provide vibration spectra (also known as fingerprints) contained molecular specific information. Unfortunately, its own scattering cross-section is very weak resulting in difficulties for analysis. To suppressing the weakness of the conventional Raman spectroscopy, tip-enhanced Raman scattering (TERS)[6-11] has been applied. Applying the strong enhanced electric field at the metallic tip to Raman spectroscopy, the intensity of the Raman signal can be enormously enhanced.

For the TERS, sample has been chosen as one-dimensional structure (eg. carbon nanotube)[6-8] or uniform coverage for flims[9] or self-assembly monolayers (SAMs).[10,11] This is because position of sample area is reflected in the signal enhancement factor. The signal enhancement factor (EF) for TERS is expressed as below:[12-14]

$$EF = \frac{I_{TERS} / N_{TERS}}{I_{Raman} / N_{Raman}}$$

where N_{Raman} and N_{TERS} are the number of probe molecules in the normal Raman and TERS signal, respectively. The I_{Raman} and I_{TERS} denote the corresponding intensity. If N_{TERS} and N_{Raman} are changed as the position of sample is chaged, it's not reasonable to compare the ratio between I_{TERS}/N_{TERS} and I_{Raman}/N_{Raman}. Therefore, sample need to have uniform coverage properties. The number of probe molecules for the normal Raman, N_{Raman}, is calculated by [(the density of probe molecule) × (diffraction limited area of the laser focal spot) × (depth of focus)] / (molecular weight of the molecule). In the case of SAMs, N_{TERS} can be expressed as follow; (surface

packing density of the SAMs) × (area of the enhanced local field). The area of the enhanced local field is determined by the FDTD simulation results.

1.1.3. Tip-Enhanced Fluorescence

In tip-enhanced fluorescence (TEF)[15-22], there are a few more things should be considered. Because of the mechanism in fluorescence that the excitation occur from the real excited electronic energy state (cf. virtual state in Raman) to ground state, the photobleaching and quenching appear. To minimize the photobleaching, the intensity of the excitation source should be diminished. Additionally, if a metallic particle is too close to probe molecules below 2 nm, quenching is dominant than spontaneous fluorescence emission. Therefore, in the case of TEF, the tip-sample distance is more critical than in the TERS and proper distance (2-10 nm) between the tip and the sample should be take into consideration (Figure 2).[23-27]

There are requirements for sample showing up TEF efficiently. The orientation and its dipole moment of probe molecules plays an important role that sample, interacting with the tip when tip is in proximity under the laser exposure.[24-26] If orientation and its dipole moment of the molecule are aligned in z-direction, enhanced signal in TEF will be maximized. But aligning the molecules in the direction we want is still exploring. With those difficulties, we just fixed the sample by spin-coating with the polymer film (eg. polymethyl methacrylate, PMMA). Then, orientation of molecules are random so we select a molecule with high enhancement among them. With polymer coating, one more merit exists that we can adjust the

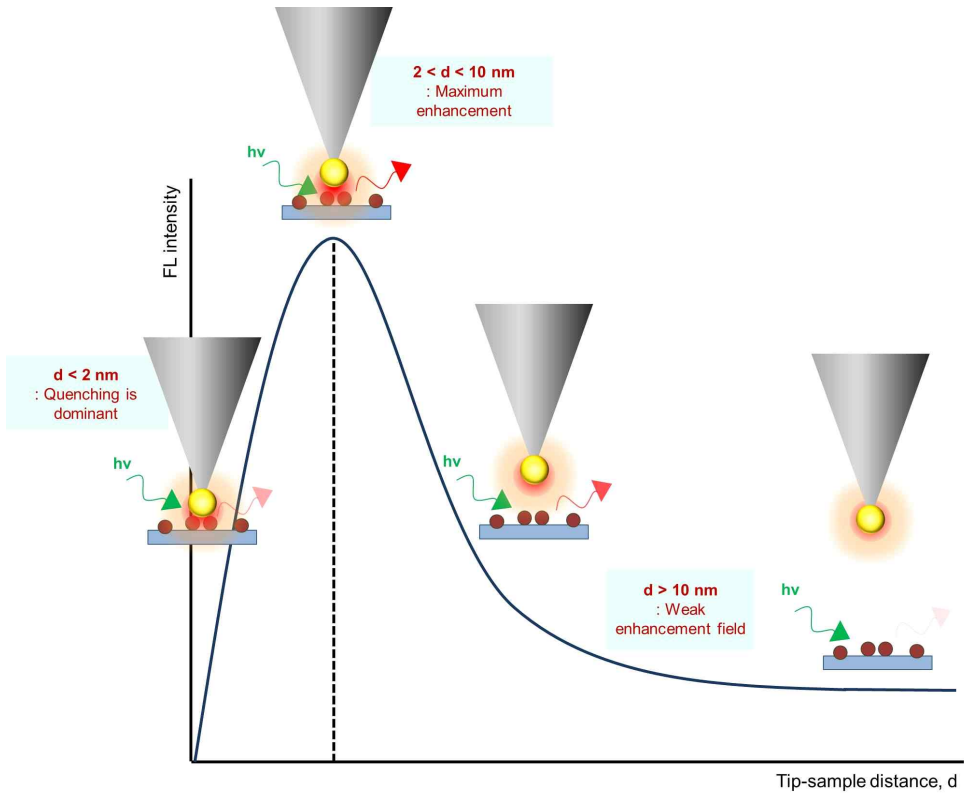

Figure 2 Fluorescence (FL) intensity as a function of the distance between the tip and the sample surface.

tip-sample distance by adjusting the thickness of the polymer film. Another sample condition is that sample ought not to have high quantum yield.[23,28,29] In the far field, the quantun yield of fluorescence $Q_0 = \Gamma/(\Gamma + k_{nr})$, while in the presence of near-field metallic nanoparticles, $Q_m = (\Gamma + \Gamma_m)/(\Gamma + k_{nr})$. The Γ is the fluorescence radiative rate, the k_{nr} is the nonradiative rates, and the Γ_m is an additional radiative rate. If the Q_0 is too high, the Γ_m will be neglected so the enhanced fluorescence signal is almost not appeared. Therefore, the sample with low quantum yield of fluorescence should be selected.

Nanostructures within the AFM tip are significant as well. In TERS, monolithic metal coated tip has been overwhelmingly used due to simplicity of the fabrication.[6-11] In TEF, however, tip with isolated structure has better local field enhancement than monolithic metal coated tip.[30] For the monolithic tip, the field enhancement is not strong to overcome the quenching owing to its structure. It becomes easier to extricate the local field from the tip-end. Besides, metal-coated tips are off-resonant with the excitation source. For the isolated nanostructure, on the other hand, the local field stayed behind its isolated structure rather than escaping from it. Also, it is fully resonant with the visible irradiation by tuning. Therefore, isolated metallic nanoparticle attached probe is preferred for TEF.

In turn, finding optimal conditions (eg. kind of the sample, design for the tip and power of laser, etc) for TEF, we can get fluorescence images with high spatial resolution and considerable enhancement.

2. Experimental setup

In this chpater, I'll explain the confocal microscope experimental setup combined with the atomic force microsopy (AFM). All of the experimental data are acquired from this setup. First, I'll explain the entire composition of the TENOM setup and how it works (2.1.). Then, I'll discuss setup in detail divided into the confocal microscopy (2.1.1.), a radial polarizer (2.1.2.) and an atomic force microscopy (2.1.3.).

2.1. Tip-Enhanced Near-field Optical Microscopy

The schematic design for the experimental setup is shown in Figure 3. To start with the irradiation of the laser with λ_{ex} = 532 nm, rays with only λ_{ex} = 532 nm passes through 532 nm line filter and other rays are blocked by this. First set of two lenses and a pinhole functions as a spatial filter. Second set of a pinhole involving the linear polarizer and the radial polarizer (Nanophoton, ZPol-532-QzM-4) will be discussed at greater length later (in the chapter 2.1.2.) for making parallel polarization beam to the tip. The dichroic mirror divided ray that half is transmitted and another half is reflected. Next two lenses are used for making 4f system to validate the confocal system. The laser goes to combined AFM (XE-120, Park Systems) and inverted microscope (IX71, Olympus). The laser is focused onto the tip through an objective lens (oil immersion, NA = 1.46), and Raman and fluorescence signals are collected through the same objective lens. Then, beam is faced with the 532 nm edge filter so only ray with λ>532 nm (Raman and fluorescence signals which

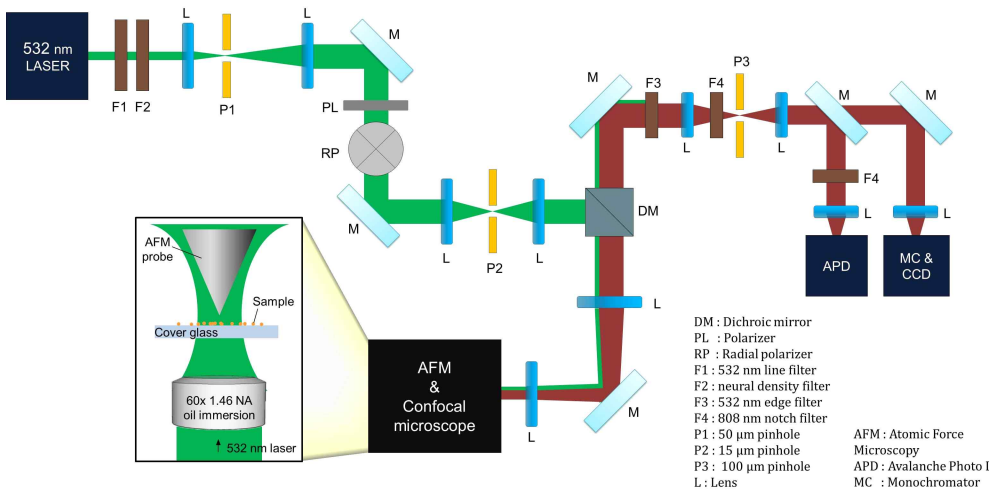

Figure 3 The experimental tip-enhanced spectroscopy setup.

we want to observe) can pass and the other is blocked. The 808 nm notch filter is blocked only the ray with λ = 808 nm from the laser involved in AFM. Third set of a pinhole also acts as spatial filter so the signal-to-noise ratio could be increased. The signal is collected to the following detectors; The avalanche photodiodes (APDs, Thorlabs) and a Raman spectrometer (Triax 320, Horiba; DU-401, Andor Tech) can be switched by a flipped mirror. We get fluorescence images by APDs and spectra by Raman spectrometer. Before using the setup, the alignment has been always checked.

2.1.1. Confocal microscopy

Confocal microscopy uses in various ways due to its high resolution images and easy operation, although it has diffraction limit of light. The invention of the confocal microscope is attributed to Marvin Minsky in 1955.[31] In Minsky's design, pinhole apertures is the

key factor to eliminate out-of-focus rays.

Confocal microsope is almost same with a conventional microscope, but main difference is that light source passes pinhole aperture with a diameter 20-100 μm hole. To understand confocal microscopy,[31,32] look Figure 4. Light is focused by a lens and then light is focused again by a following lens. Red plane indicates the signal comes from the target species located in the focal volume, source 1. In other words, a point source of light is confocal with source 1. We also see light coming from a out-of-focus that generates background signal. Blue plane is not at the focal point of the lens, so it cannot pass pinhole aperture. Consequentially, by applying pinhole, it's possible to pass selectively source 1 and reject light coming from out-of-focus like source 2. In this way, the background signal is significantly reduced compared with the conventional microscope. In addition, the resolution in depth can be considerably improved. However, the confocal microscope still has resolution limitation due to diffraction as the conventional microscope does.

We get confocal fluorescence image of nile red molecules (in the polystyrene beads with a diameter of 20 nm, Invitrogen), Figure 5A, which is appeared as small circles. A solution that was diluted with water by a factor of 10^4 times was spin-coated at 3000 rpm for 60 seconds on a glass substrate. The glass substrate treated piranha and RCA I processes before using. Resolution could be checked by line indicated in Figure 5A, white line. Line profile is appeared in Figure 5B and C. Full width at half maximum (FWHM) which means resolution is confirmed up to 250 nm. We get theoretical value by putting parameters into Abbe's diffraction limit equation, $d = \lambda/2NA$. We use light source as a laser with $\lambda = 532nm$ and oil immersion

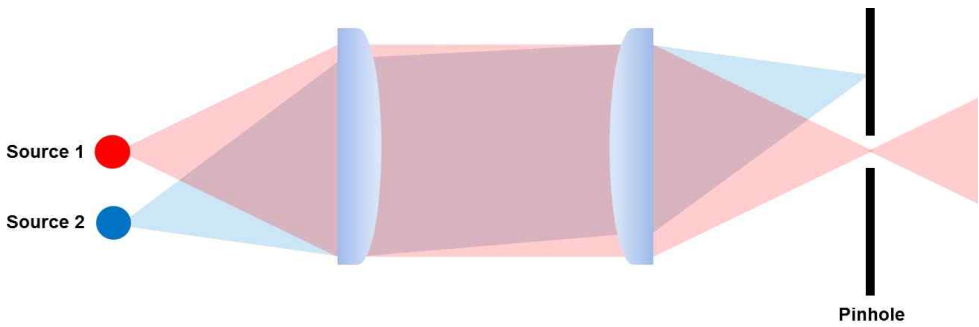

Figure 4 Source 1 (red) passed through two lenses and focuses on aperture of a pinhole. Otherwise, source 2 (blue) is blocked by a pinhole. As a result, light from only source 1 (red) makes signal by reaching a detector. Background from defocused rays such as source 2 (blue) is considerably depressed.

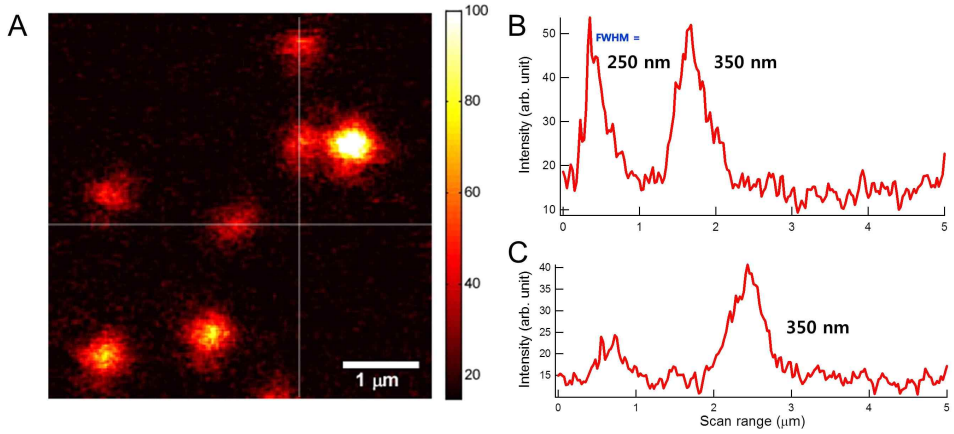

Figure 5 **A** confocal fluorescence image. Image smoothing processing is applied. In each points, the exposure time is 10 ms. The color scale bar indicates intensity of fluorescence. **B** Line profile applicable to a white parallel line in 2A. Here, FWHM is about 250, 350 nm, respectively. **C** Line profile applicable to a white vertical line in 2A. FWHM is about 350 nm.

objective lens that has $NA = 1.46$. To apply these, $d = 532/(2 \times 1.46) = 182\,nm$. Compared with experimental data, 250 nm, it is not deviate a lot. Therefore, we can confirm the size of pinhole is proper, and the confocal microscope is well operate as well.

2.1.2 Polarization mode converter

Polarization mode converter can be used in many ways, e.g. polarization Raman microscope,[34,35] surface deformations,[36] optical imaging of tautomerization,[37] and high-focusing microscopy.[38] We insert polarization mode converter into the confocal setup to use near-field microscopy that is basis for the concept of the confinement of incident light with a nanoparticle which was discussed already in chapter 1. Now, let's look at the radial polarization in detail.

First, we need to know how radially and azimuthally polarized doughnut mode (RPDM and APDM, respectively) is made. To make doughnut-mode laser beam, laser passes through a linear polarizer, a polarization mode converter[37,38] (also known as radial polarizaer), a lens, a pinhole and a lens in order (as shown in Figure 6A). The linear polarizer is an optical filter that make beam with only specific direction of vector passes. We adjust the beam through the polarizer is parallel to its reflection plane. And then, beam passes radial polarizer that consists of four segments of half-wave plate. By rotating polarization mode converter, we can make RPDM or APDM. Both two modes have doughnut-shaped intensity distribution,[38] and the pinhole (with a diameter of 15 μm) functions as a mode cleaner.[37,38]

The electric field vector in the focal plane is completely different even though both RPDM and APDM have doughnut-shaped

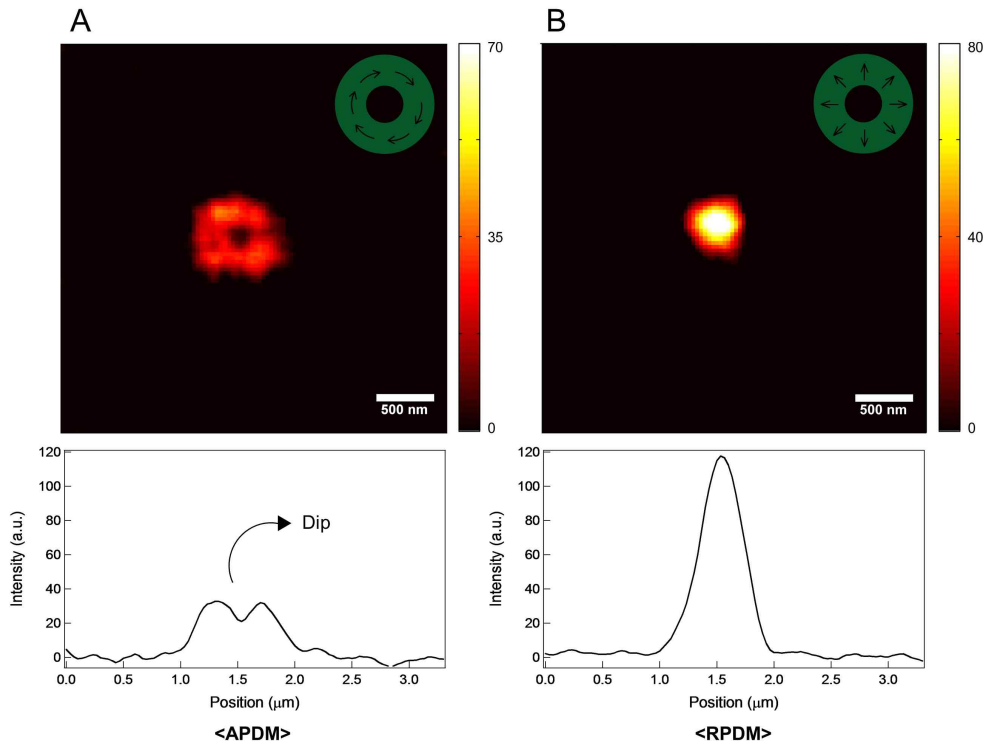

Figure 6 Fluorescence images of nile red molecules and line profiles sampled along the corresponding images when using **A** APDM and **B** RPDM, respectively.

intensity distribution. In APDM (Figure 6B), when laser is focused by high NA objective lens, only in-plane (xy) polarization component is remained in the focal plane.[34,37] This still contains doughnut mode intensity distribution in that the lateral field intensity is strictly dominant. In RPDM (Figure 6C), however, additional mode that the electric field vector in the focal plane is parallel to z-axis (longitudinal direction) is made.[34,37] Here, longitudinal components is stronger than in-plane so that the electric field intensity is the strongest at the center instead of doughnut mode intensity distribution. According to this, fluorescence image in APDM and

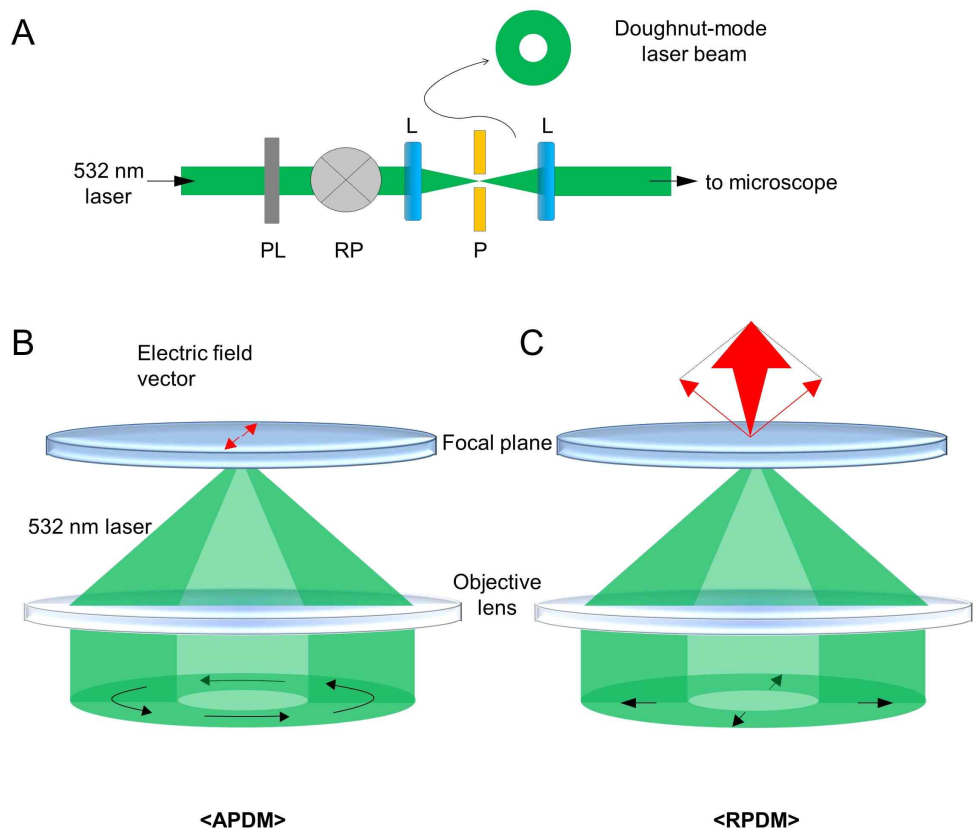

Figure 7 The polarization mode converter. **A** The partial experimental setup (PL: linear polarizer, RP: radial polarizer, L: lens, P: pinhole with a diameter of 15 μm). **B** Electric field formation in the focal plane when APDM is focused by high NA objective lens. **C** When RPDM is focused in the focal plane, direction of vector is perpendicular to the focal plane.

RPDM emerged as doughnut and filled sphere shape, respectively (Figure 7). In the line profile indicated in Figure 7A (APDM), the dip indicated with an arrow proves that the polarization mode converter works properly. In Figure 7B (RPDM), fluorescence appear as a small sphere with the higher intensity distribution at the center as expected.

2.3. Atomic Force Microscopy (AFM)

We use a near-field microscopy that is combined with the confocal microscopy involved the radial polarizer (we discussed so far in the previous sections) and an atomic force microscopy (AFM). In this section, we look through how the AFM functions.[39,40]

The AFM is measured in three dimensions, the horizontal (xy) plane and the vertical (z) plane. Resolution at z-direction up to nanoscale is normally higher than xy plane. The key principle is the beam-lever deflection method based on laser and photodiode array (Figure 8). In Figure 8A, the reflected laser from cantilever of the AFM probe is detected by a position-sensitive photodiode (PSPD). Here, deflection of cantilever can vary as topography of the sample changes. If tip is moving up and down, the laser will reach the A and B sections of the PSPD (see Figure 8B). Likewise, the laser will fluctuate between C and D sections of PSPD when the tip is moving side to side. In the case of the former, it generates AFM signal (normal force). The latter case, it generates the lateral force microscopy (LFM) signal (lateral force) and the type of image data is friction.[41]

The signal from the PSPD goes to feedback loop that controls the z-position of the probe through piezoelectric scanner connecting to the AFM probe. In our system, scanner of sample is moving to xy plane with a raster scannig, while AFM head is moving up and down (z-direction). In other words, the images of AFM are acquired by the combination of raster scanning in sample stage and height profiling in AFM.

The AFM imaging modes can be largely categorized as the contact, tapping and noncontact mode. As you can see in the Figure

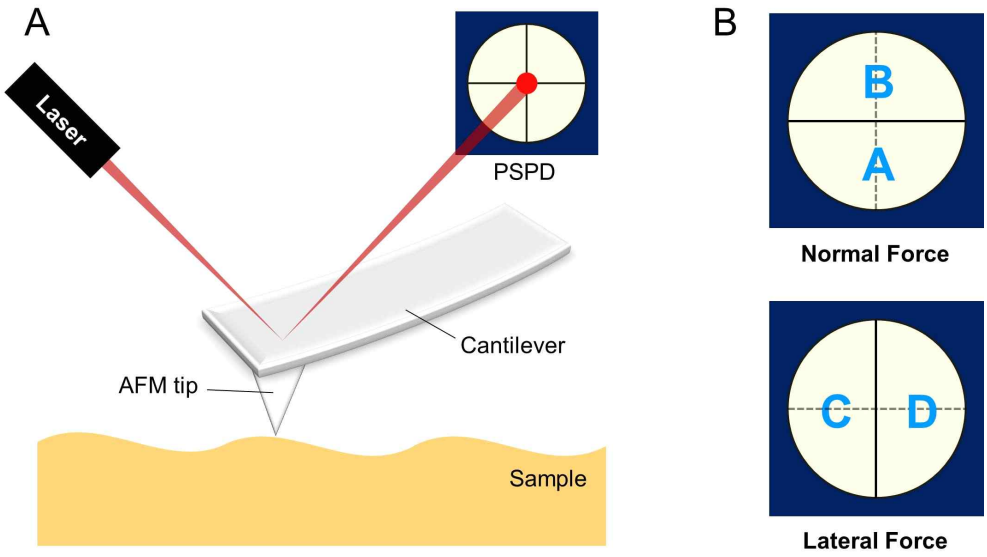

Figure 8 **A** A brief illustration how to work an AFM. **B** segments of position- sensitive photodiode (PSPD).

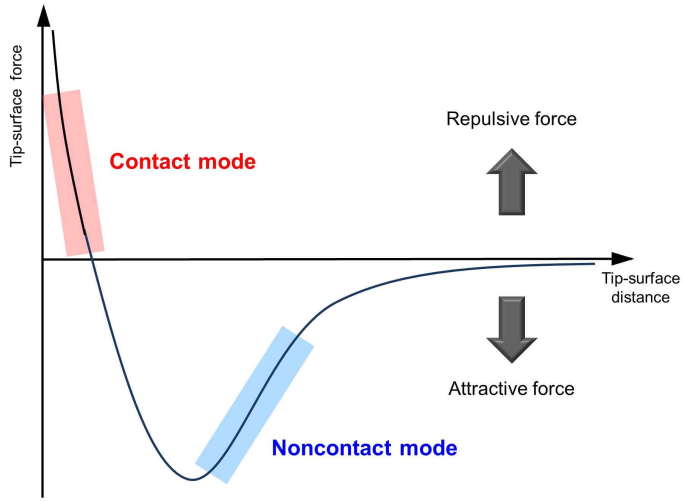

Figure 9 Interatomic force versus distance between tip and sample curve.

9, in the contact mode, the tip-surface distance is very small so a strong repulsive force appears between the tip and the surface. Constant height mode and constant force mode are included in the contact mode. For the constant height mode, variation of the cantilever deflection is related to topographic images, whereas for the constant force mode, z-direction scanner moving of tip is directly connected to topographic images and deflection of cantilever is fixed by the feedback circuit. Using contact mode can damage samples and distort image. For these reasons, contact mode is used for flat samples or for lithography using intended damage. In the noncontact mode, however, an instantaneous polarization interaction, that is to say an attractive interaction, appears. The tip is oscillated at the specific resonance frequency and the amplitude of the oscillation is kept constant. Comparing with noncontact mode and tapping mode, both are based on a feedback mechanism of constant oscillation amplitude. But amplitude of tapping mode set about 50-60% of free amplitude while that of non-contact mode set about ~100%. In conclusion, tapping mode takes advantages of two other modes and provides higher resolution images with minimum sample damage.

3. A Au Core/Ag Shell (Au@Ag) Nanoparticle Probes for Tip-Enhaced Spectroscopy

In the chapter 3 and 4, tip-enhanced spectroscopy with experimental data will be discussed in earnest. In this chapter, a new tip with a Au core/Ag shell nanoparticle (Au@AgNP) developed. And we observed the aspect that effectiveness of TERS signals as the size of the nanoparticle which is attached to the probe increases. Synthesis parts for the tip (3.1.1.) were conducted by my coworker, woong Kim who belongs in department of chemistry, Pohang university of science and technology, Korea.

3.1. Au@Ag Nanoparticle Probes

3.1.1. Preparation for Au@Ag Nanoparticle Probes

Preparation for Au@AgNP probe can be explained over a four-step. Figure 10 shows the transfer process of a single 5 nm AuNP through the differential binding forces of DNA-DNA interactions (first step).[42] The AuNPs tethering a single DNA strand with 63 bases (Oligonucleotides was purchased from IDT) for each were hybridized onto complementary DNA with 20 bases that was immobilized onto the silicon wafer surface.[43] For this, silane coupling agent, N-(3-(triethoxysilyl)-propyl)-O-polyethyleneoxide urethane (TPU, Gelest) was used to generate the underlying silane base layer. And the dendron was immobilized to the silane base layer. The AFM tip (ContGD-G for contact mode; Tap190-G for noncontact mode, BudgetSensors) tethering 40 bases DNA approached the substrate. The single strand of DNA (ss-DNA) on the tip had a base sequence

that is complementary to the single strand part of DNA attached to the 5 nm AuNP. Upon the tip-sample contact, the 40 bases DNA on the tip hybridized with the complementary part of the DNA on the substrate. The binding force between these two strands (50 pN) is stronger than the force between the substrate DNA and the AuNP-bound DNA (20 pN), so the ss-DNA and its bound AuNP was transferred from the substrate to the tip during retraction. In this work, the surfaces of the tip and the substrate were modified with dendrons (Figure 10B) that serve as lateral spacers between the neighboring DNA strands. As reported previously,[44] the dendron-modified AFM tip guarantees single molecular interaction (in our case, transfer of a single seed NP).[45] Using the procedure described above, we transferred AuNP seeds to the tips with a success rate of 70%. The TEM image in Figure 10C shows the transferred AuNP seed.

And the tip was immersed in a silver enhancing solution, which was a mixture of 200 μL of 1.0 mM $AgNO_3$ aqueous solution, and 50 μL of 1 mM sodium L-ascorbate (BioReagent, Sigma Aldrich) in phosphate-buffered saline solution (PBS, pH 7.4). While a strong reductant such as sodium borohydride ($NaBH_4$) produced silver nanoparticles at various positions on the AFM tip, sodium L-ascorbate selectively enhanced silver only on the gold particle and reduced also the nonspecific deposition of silver particles on the silicon surface of the AFM tip. Because the adhesion of the nanoparticle on the tip was weak, the detachment during the measurement was a common problem. We observed that an annealing process increased the adhesion strength. In particular, the tip was heated in air at 500℃ for 10 min (third step, Figure 11A), after enhancing the gold nanoparticle (second step) attached to the tip in the silver solution for 10 min (enhancing at the condition gave the core-shell particles of about 8 nm in size). The thermally treated tip

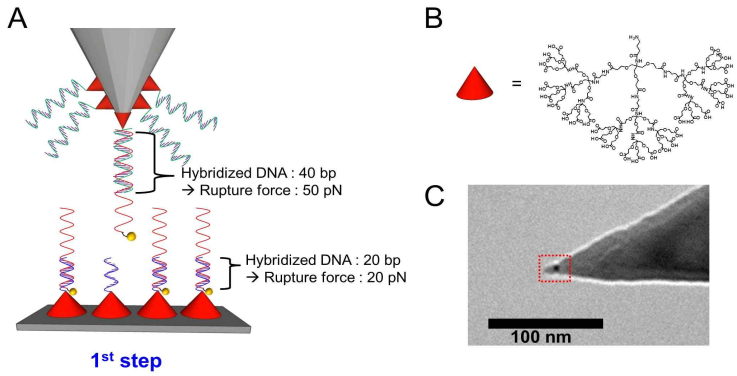

Figure 10 The first step in making Au@Ag NP probes. **A** A schematic illustrating the trasfer from the substrate to the tip of a single DNA strand tethering a AuNP. **B** Chemical structure of the dedron used for the surface modification. **C** The TEM image of a tip with a single AuNP transferred from the substrate.

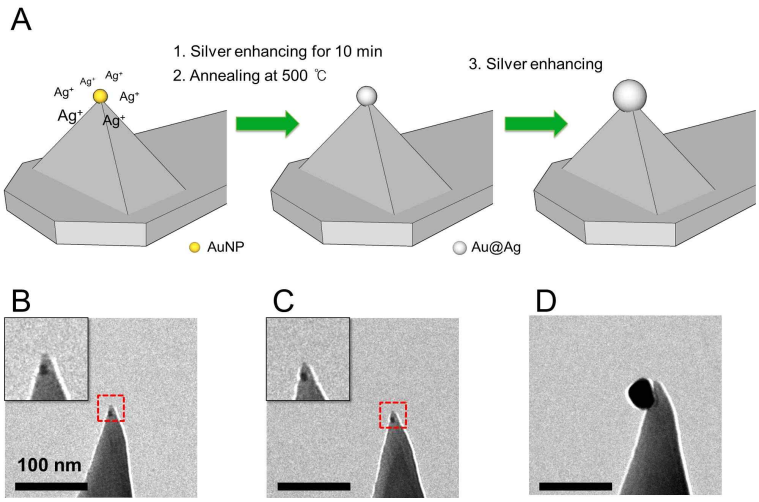

Figure 11 Preparation of the Au@Ag nanoparticle probe and the corresponding TEM images. **A** 5 nm seed AuNP is enhancing (step2) and annealing (step3) after picked up by an AFM tip. And then in a solution of AgNO3 and sodium L-ascorbate, Au@Ag particle is enhancing again (step4). **B** A TEM image of 5 nm AuNP attached to the AFM tip. **C** After enhancing and 500 ℃ annealing process, size of Au@Ag nanoparticle is 7.6±0.3 nm. **D** Final silver shell growth by placing in the silver enhancing solution in 1 h.

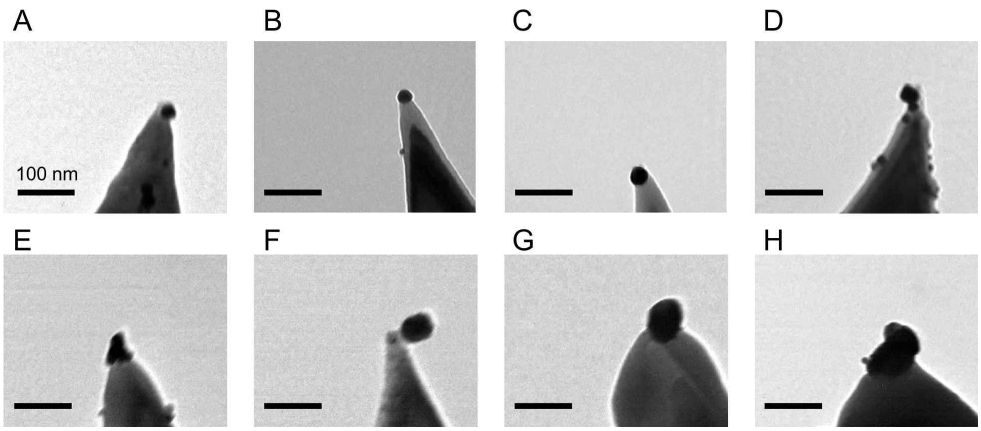

Figure 12 Representative TEM images of the Au@AgNP probes with various sizes of NPs, which are **A** 24 nm, **B** 28 nm, **C** 34 nm, **D** 40 nm, **E** 50 nm, **F** 55 nm, **G** 60, and **H** 90 nm.

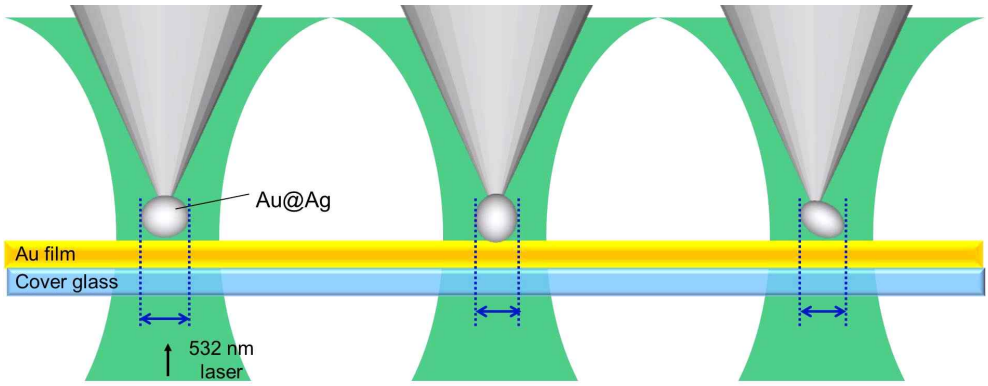

Figure 13 Approach to determine the effective size of elliptical nanoparticles with various orientations.

was immersed in the enhancing solution again (fourth step) to generate a particle of the target size. It was possible to control the size of the resulting silver particle by varying the reaction time. We find that such a four-step procedure is far more effective than a three-step (absence of annealing process) in terms of the adhesion strength of the NPs. In order to minimize the deleterious effect of the oxidized silver layer, the tip was immersed in the silver enhancing solution shortly just before the TERS measurement. We confirmed that last treatment did not induce variations of the particle size. Figure 12 displays representative TEM images of the fabricated Au@Ag probe in which the Au@AgNPs with a diameter of from 24 to 90 nm.

The Au@AgNPs are, in the most case, elliptical so final size of NPs was determined by the following approach (Figure 13). We measure the distance between the left and right ends axis parallel to the beam direction. It's pretty good way to guess the effective size. But it has a limitation that we cannot measure the actual effective size of Au@AgNPs which approaches the Au film in proximity for TERS because we don't know the accurate structure with 3-dimension in Au@AgNPs probe through the TEM images of the probes. In other words, actual effective size of Au@AgNP may differ slightly from our expectations.

3.1.2. FDTD Simulated Results of a Silver Nanoparticle

To characterize the plasmonic properties of Au@AgNP probes, we ran the FDTD simulation[46] for confirming the extinction spectra of a AgNP. Even though we use the core-shell NP probes, it play like a AgNP due to its small size of core. That's why we use AgNP model in FDTD simulations. Also we checked there are marginal

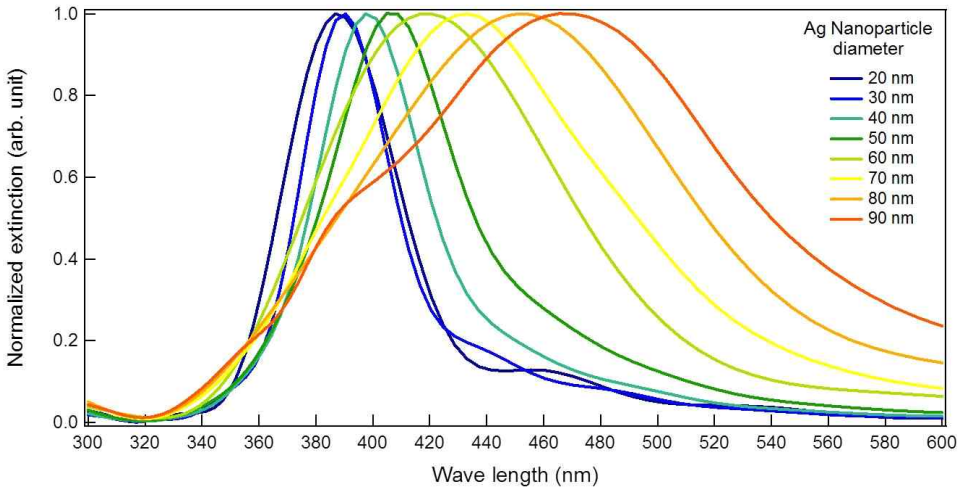

Figure 14 Simulated extinction spectra of AgNPs in accordance with the NP size from 20 to 90 nm. As size of AgNP increases, wavelength of maximum absorbance shifts to red.

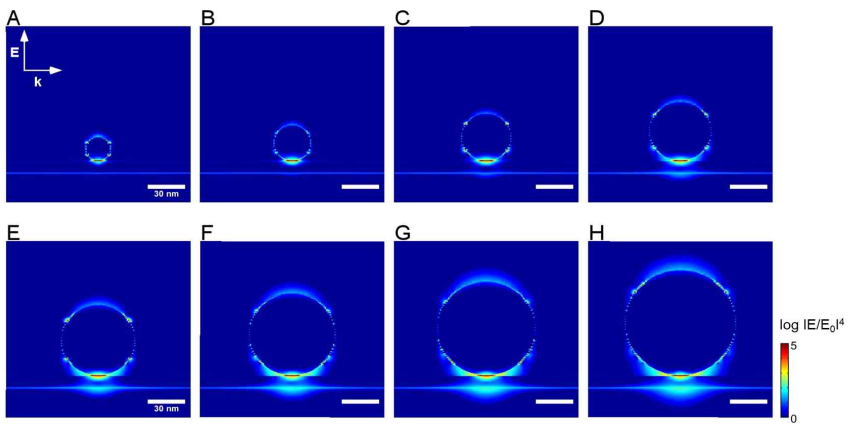

Figure 15 Simulated electric field distribution between the gold film with 10 nm thickness on glass substrate and the AgNP with **A** 20 **B** 30 **C** 40 **D** 50 **E** 60 **F** 70 **G** 80 **H** 90 nm diameter. The spacing between the gold film and AgNP is set in 0.7 nm at all occasions. The color scale bar indicates intensity of electric field which expressed as $\log|E/E_0|^4$. The E, k and the corresponding arrows represent the polarization and propagation direction of the incident light (λ_{ex} = 532 nm).

variations between Au@Ag and AgNP model. Figure 14 is the simulated extinction spectra of AgNP with size from 20 to 90 nm. The λ_{max} of the absorbance shifts to red with increasing the size of the AgNP as expected.

We can also expect enhanced electric field is much larger as size of AgNP increases since bigger size of AgNP is much well resonant with the excitation source (λ_{ex} = 532 nm). It was confirmed by simulated electric distribution[46] in Figure 15. The maximum electric field intensity which is expressed as $\log|E/E_0|^4$ showed up at the junction between AgNP and gold film. In each case, numerical value of electric field intensity ($\log|E/E_0|^4$) is 5.65, 6.36, 6.63, 6.59, 6.62, 6.70, 6.71, and 6.66 in ascending order of AgNPs size.

3.2. Sample Preparation

In Figure 16, the partial experimental setup is displayed that involved sample for TERS measurements. Clean cover glasses were coated with Au (10 nm)/Ti (2 nm) using an e-beam evaporator. Biphenyl-4-thiol (BPT, 97%, Sigama Aldrich) was dissolved in dichloromethane and diluted in ethanol (final concentration of solution: 25 mM). The Au-coated cover glasses were immersed in BPT solution for 2 hours and then it is washed out by ethanol. Finally, the self-assembled BPT monolayer was prepared on the gold-coated cover glass substrate.

3.3. TERS with regard to size of the Au@Ag nanoparticle

To check the vibration peaks of BPT in our setup, we first examined the normal Raman spectrum of the powdery BPT. Sample

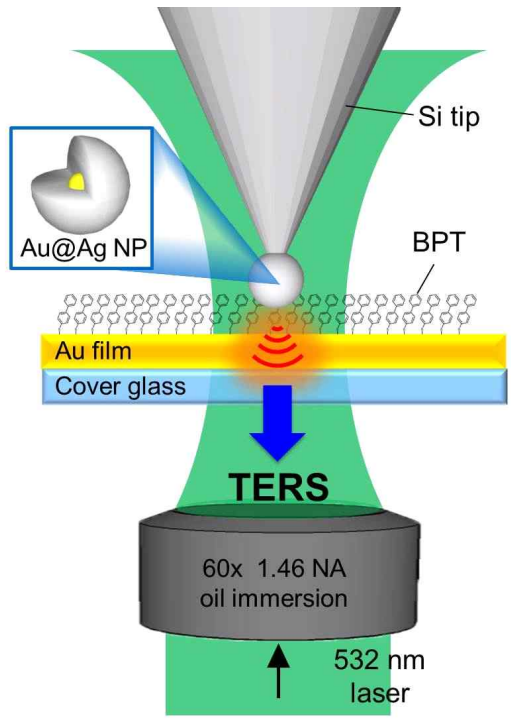

Figure 16 Partial experimental setup for TERS measurements that included sample, Self-assembled BPT monolayer on Au-coated film.

was prepared by just putting the powdered BPT on the cover glass. The spectrum for this normal Raman is shown in Figure 17. And then we carried out the TERS measurements for BPT, switching the probes with various sizes of nanoparticles. Figure 18 shows Raman spectra of the BPT sample collected without and with the tip. The spectra demonstrate the pronounced enhanced Raman peaks of BPT (Table 1; peak assignments for Raman and TERS). Intensity of enhanced Raman signals is increased as size of Au@AgNP increases. The peaks with C-H bending (1174 cm^{-1}) and ring stretching (1288, 1573 and 1585 cm^{-1}) are dominantly enhanced. Especially in the spectrum with the 60 nm of Au@AgNP probe, an extraordinary result was observed. At the wavenumber around 1000 cm^{-1}, three peaks

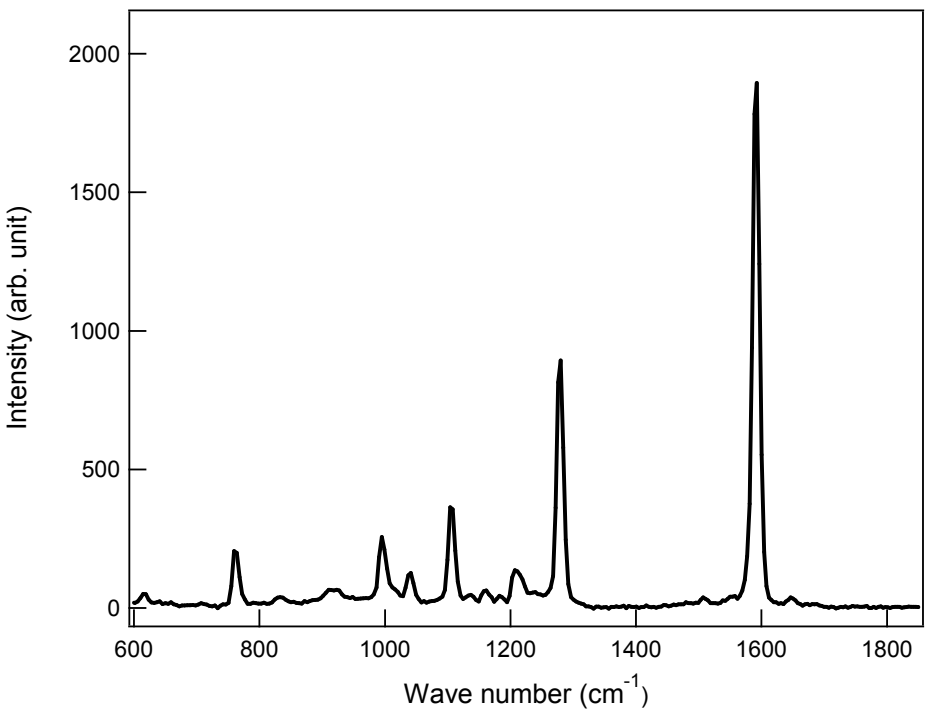

Figure 17 Raman spectrum of BPT (powder). The integration time is 180 s.

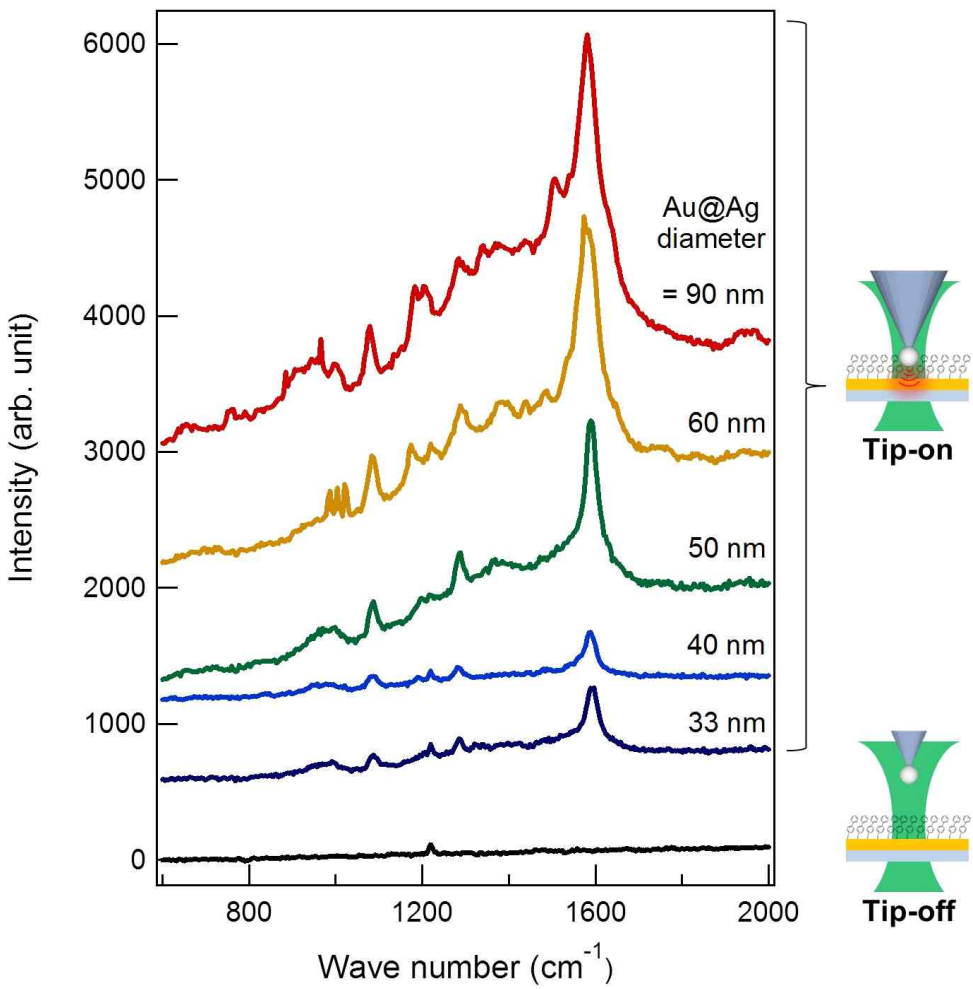

Figure 18 A set of BPT TERS spectra with the Au@AgNP-attached probes. For all cases, an identical BPT sample was examined and the laser power and exposure time are 20 μW and 180 s, respectively.

Peak No.	Normal Raman[b]	TERS	Peak assignments[c]
1	759.51	759.51	ν(S-C)
2	-	986.56	δ(C-H)
3	995	1003.4	
4	-	1020.3	
5	1103.8	1174.1	
6	1280.2	1288.3	ring ν(C=C)
7	1588.8	1573.3	
8	1592.6	1584.9	

Table 1 Peak assignments for the Raman and TERS spectra for BPT (in cm-1). Normal Raman was measured from powdery BPT. For the assignments in TERS, two spectra was employed that was acquired by using 60 and 90 nm Au@AgNP probes. Vibration peak assignments and notations[47-49] are as followed; ν: stretch, δ: bend.

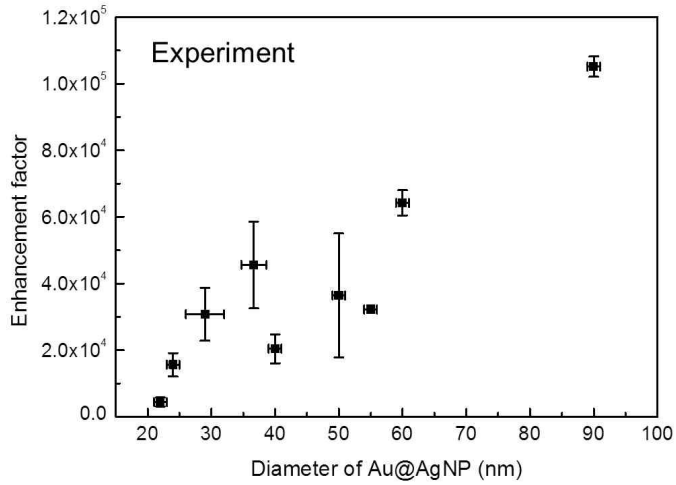

Figure 19 Plot of enhancement factor as a function of size of Au@AgNP at 1573 & 1585 cm^{-1}. In this plot, 20 sets of experimental data were used.

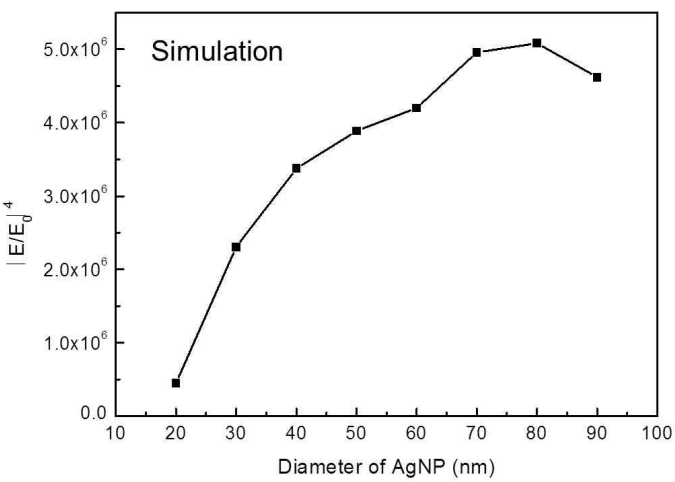

Figure 20 The simulated enhancement factor expressed as $|E/E_0|^4$ along the diameter of AgNP. The $|E/E_0|^4$ indicates the enhancement factor.

appear for the TERS even though only one peak appears for normal Raman. This implies the immense signal enhancement occurs by the 60 nm Au@AgNP probe.

Figure 19 indicates the TERS enhancement factor plotted as a function of Au@AgNP diameter at the most enhanced peaks (1585, 1573 cm^{-1}). For plotting, 20 sets of experimental data were employed. Here, we inserted x-error bar as well and the reason is to calibrate the our approach for measuring the size of Au@AgNP which was discussed in more detail in the previous chapter (3.1.1.). TERS signal shows a systematic increase with increasing size of Au@AgNP.[50-52] The simulated result (Figure 20) supports our experimental data. The dependence qualitatively agrees with the hypothesis that the nanoparticles act as point-like dipoles: within the quasi-static approximation, the dipole polarizability of a small nanosphere is $4\pi\epsilon_0 a^3(\epsilon_M-1)/(\epsilon_M+2)$, where a is the radius of the nanoparticle and ϵ_M is the dielectric function of the metal. Thus, the increase in the dipole strength and the resulting local field intensity.

3.4. Conclusions

The Au@Ag nanoparticle was synthesized selectively on a tip-end and the size of the nanoparticle can be controlled by changing the reaction time in the enhancing solution. With the TERS measurement, we have verified that such tips can be used as plasmonically active near-field probe. As Au@AgNP size is increasing, plasmonic enhancement has been shown a tendency to increase in both cases of the experimental and simulated results. We believe that the current preparation procedure can be extended to nanoparticles of various configurations that is expected to maximize the field enhancement.

4. Nanostar Probes for Tip-Enhanced Spectroscopy

We measured TERS signals and got TEF images by using nanostar probes. Likewise the chapter 3, synthesis parts for the tip (4.1.1.) were conducted by my coworker, woong Kim who belongs in department of chemistry, Pohang university of science and technology, Korea. I cite my sources of chapter 4; *Nanoscale*, 10.1039/C5NR06657C.[42]

4.1. Nanostar Probes

4.1.1. Synthesis of Nanostars and Nanostar Probes

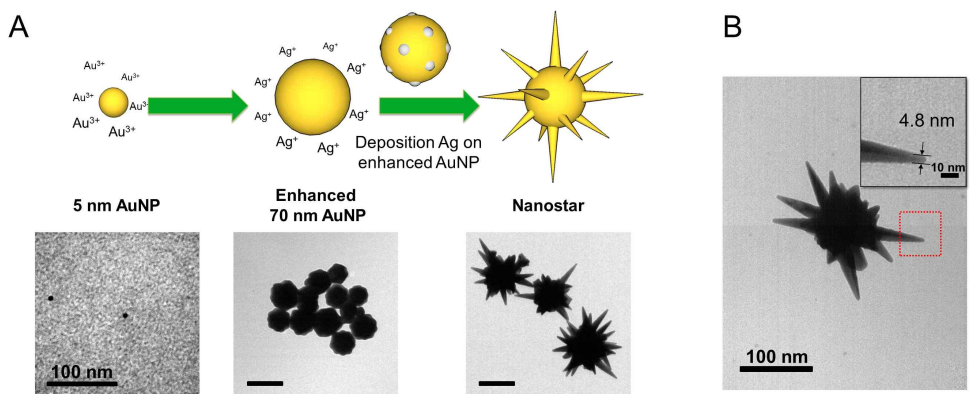

Figure 21 **A** A schematic diagram of nanostar synthesis and the corresponding TEM images of 5 nm AuNP, enhanced 70 nm AuNP and nanostar. **B** The TEM image of a nanostar. The inset shows the magnified views of the spikes of the nanostar.

Nanostars were synthesized by enhancing small seed Au nanoparticles (AuNPs, diameter of 5 nm, Ted Pella) and subsequently

forming sharp spikes on the enlarged nanoparticles as shown in Figue 21A. For the enhancement, the 100 μL of 65 nM seed solution and a 200 μL solution of 50 mM $HAuCl_4$ (99.999%, Sigma Aldrich) was mixed with 10 mL of deionized water. Next, 400 μL of 2.0 mM $AgNO_3$ solution (99.9999%, Sigma Aldrich) and 200 μL of 100 mM ascorbic acid solution (99.0%, Sigma Aldrich) was added. The resulting solution was stirred for 1-2 minutes, and the color turned from yellow to pink. The size of the seed NPs increased through the reduction of gold ions to form lager NPs with a diameter of 70 nm. Finally, the spikes were grown on top of the NPs by the reduction of gold on silver deposition sites as reported previously.[53] In Figure 21A, each images corresponding to the steps are characterized by the transmission electron microscopy (TEM, JEM-1011, JEOL). Also, in Figure 21B, we confirmed that sharp edge of the spike of the nanostar had measured 4.8 nm.

Synthesis of nanostars on the end of a scanning tip is similar to that of the colloidal nanostars described above. I'll explain the synthesis of nanostars over three steps for better understanding. Please note that actual synthesis process for second and thrid step is the one-pot procedure. First, we attach the seed NP to the tip via DNA-DNA hybridization,[43,54] and then grow nanostars *in situ*. The alternative strategy of directly attaching fully grown nanostars to the tip (either by electrostatic pickup or chemical functionalization) is unfeasible because the contact area between the nanostar and the tip is too small to provide sufficient adhesion between the nanoparticle and the tip.

The first step is that a gold nanoparticle of 5 nm in diameter was transferred to an AFM tip (See Figure 11 in chapter 3.1.1.). Next, Figure 22 schematically shows the one-pot synthetic procedure for the preparation of the nanostar probe by enhancing solution after 5 nm of a seed AuNP picked up by an AFM tip. Here's how

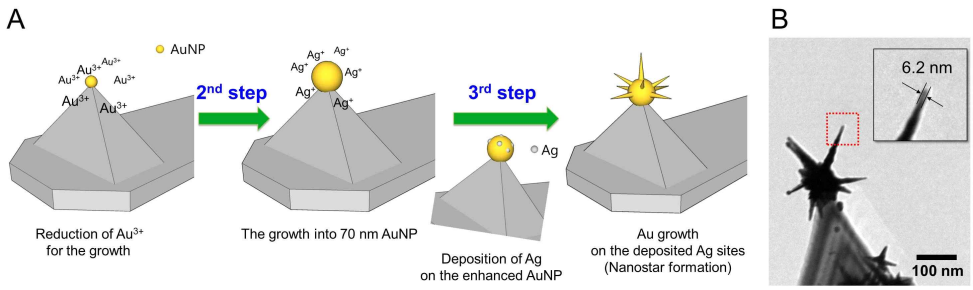

Figure 22 **A** The one-pot synthetic procedure fabricating a nanostar probe, which includes the growth of the NP (second step) and the subsequent growth of sharp spikes on the active site of the AuNP (third step). **B** TEM image of selected nanostar probe. The inset shows a magnified view of the spike.

enhancing solution was made. 20 μL of 50 mM $HAuCl_4$ and the same volume of 1.0 M HCl were added to 20 mL deionized pure water. Under vigorous stirring, 40 μL of 2.0 mM $AgNO_3$ solution and 20 μL of 100 mM freshly prepared ascorbic acid solution were added. Then, the probes were added into the solution immediately after the mixing. The yellowish color of the resulting solution changed to green after a few minutes. After the color change, the immersed probes were rinsed by deionized water to remove nonspecifically bound particles and excess chemicals. The Au^{3+} ions were reduced to make the initial nanoparticle bigger (second step, Figure 22A). For this growth step, ascorbic acid reduced Au^{3+} preferentially in the developing solution because Au ions have higher reducing potential than Ag ions ($Au^{3+}+3e^- \rightarrow Au$, 1.5 eV; $Ag^+ + e^- \rightarrow Ag$, 0.8 eV). Tiny silver particles were deposited on the surface of the enhanced AuNP through the under-potential reduction[55-58] by ascorbic acid, and the active sites of the AuNP initiated formation of gold spikes (third step, Figure 22A). It is known that the surface density of silver islands determines the number and shape of the spikes. A careful tuning of Ag^+ concentration is important for the generation of spikes with the

desired dimensions. Solutions with high Ag^{+} concentrations (>40 μM) led to very short spikes (length: 15–20 nm) and significant nonspecific growth on the tip body. Solutions of low concentration (<0.04 μM) led to no spikes on the surface of AuNP. We found that the medium concentration (4 μM) yielded nanostars with sufficiently long spikes (length = 50–80 nm), while the number of spikes was smaller than that of nanostars grown in solution. Additionally, we observed that a solution with high Au^{3+} concentration induced nonspecific formation of nanoparticles on the whole body of the AFM tip, and slow stirring resulted in nanostars with too-thin branches. The use of a dilute Au^{3+} solution (50 μM) suppressed the nonspecific growth of unwanted parts and a stirring speed of 700–800 rpm resulted in spikes with sufficient thickness (~10 nm). The procedure we employed is based on the method by Yuan *et al*,[53] but it was modified to avoid nonspecific growth. More typical procedures of nanostar generation, which involve the use of shape-directing reagents such as cetyltrimethylammonium bromide (CTAB)[59] or polyvinylpyrrolidone (PVP)[60], were not employed because such reagents tend to generate background signals in TERS and TEF measurements.

Figure 22B displays a representative TEM image of the fabricated nanostar probe in which the spikes with a radius of under 10 nm are located at the apex of the tip. Typically, ten out of 15 tips formed a nanostar at the tip apex (yield = 67%). We found that the orientation (relative angle between the axes of the tips and the spikes) of each spike was hard to control. The nanostar tips were found to have mechanical stabilities sufficient for AFM scanning. In only one or two cases out of ten, the nanostar was detached from the probe during scanning, although the TEM images obtained before and after the scanning show slight blunting and wear on the remaining nanostar.

4.1.2. Properties of the Nanostars and Nanostar Probes

4.1.2.1. Optical Properties of the Nanostars

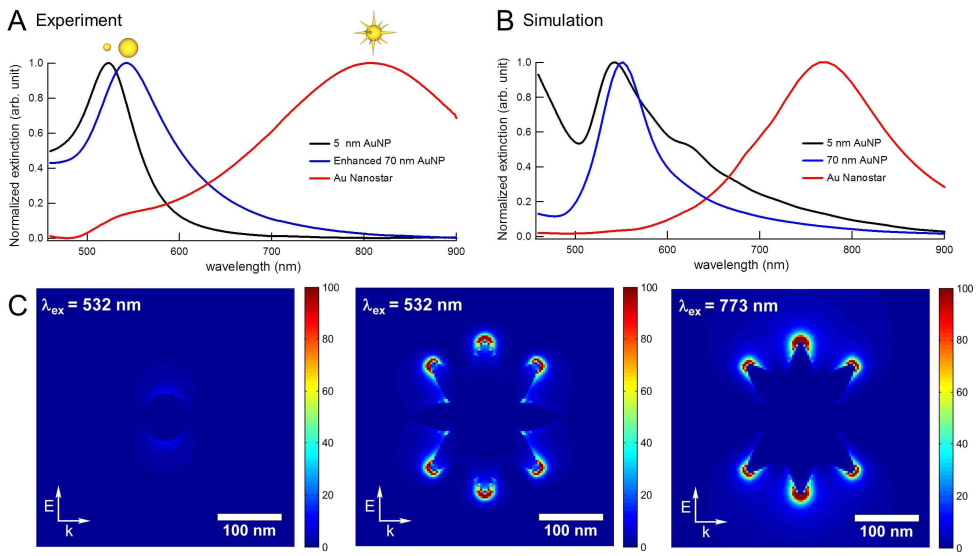

Figure 23 The optical properties of the nanostars. **A** The extinction spectra for experiment of 5 nm AuNPs (black), 70 nm AuNPs (blue), and the nanostars (red). **B** FDTD simulated scattering spectra of the corresponding nanoparticle. The λ_{max} of the nanostar is 773 nm. **C** Simulated local field distribution around the 70 nm spherical AuNP at λ_{ex} = 532 nm, the Au nanostar at λ_{ex} = 532 nm and the Au nanostar at λ_{ex} = 773 nm. The color-scale for intensity is expressed in $|E/E_0|^2$. The E,k and the corresponding arrows represent the polarization and propagation direction of the incident light.

We examined the plasmonic properties of nanostars in a colloid. The seed AuNPs with a diameter of 5 nm showed dipolar plasmon resonance at λ_{max} = 519 nm (Figure 23A, black line). The enlarged NPs showed a slightly red-shifted resonance at λ_{max} = 543 nm (Figure 23A, blue line). The Au nanostars resulted in a resonance

at λ_{max} = 809 nm (Figure 23A, red line). Such a red shift following spike enhancement is caused by the excitation of longitudinal plasmon modes in the spikes of the nanostars. Because we use the laser with wavelength, λ_{ex} = 532 nm, the dipolar plasmon of the nanostar is slightly off-resonant with the excitation source. The change in scattering spectra was fully simulated by finite-difference time-domain (FDTD) calculation,[46] as shown in Figure 23B. It showed similar aspects compared with the experiment. According to simulated electric distribution (Figure 23C), the nanostar provides strong electric field enhancement that is significantly larger than that of the spherical NP.

4.1.2.2. Mechanical Properties of the Nanostar Probes

Regarding the performance of the nanostar tip for the topographic measurement, we can see both advantage and disadvantage of it over the commercial silicon probe (PPP-NCH, Nanosensors). For the samples of small topographic contrast (for example, single molecules, graphene, or DNA chains on a flat substrate), only one spike (usually with a radius of <5 nm) on the nanostar is expected to interact with the sample, and thus the tip will provide spatial resolution that is equal to, or better than, the one obtained from the Si-tip. For the samples of large topographic contrast (for example, nanoparticles with >10 nm diameter), several differently oriented spikes on the nanostar may interact with the nanostructure concomitantly, leading to noticeable topographic convolution effect (Figure 24). In this regard, the nanostar tip is better suited for the sample of small topographic contrast.

4.2. Sample Preparation

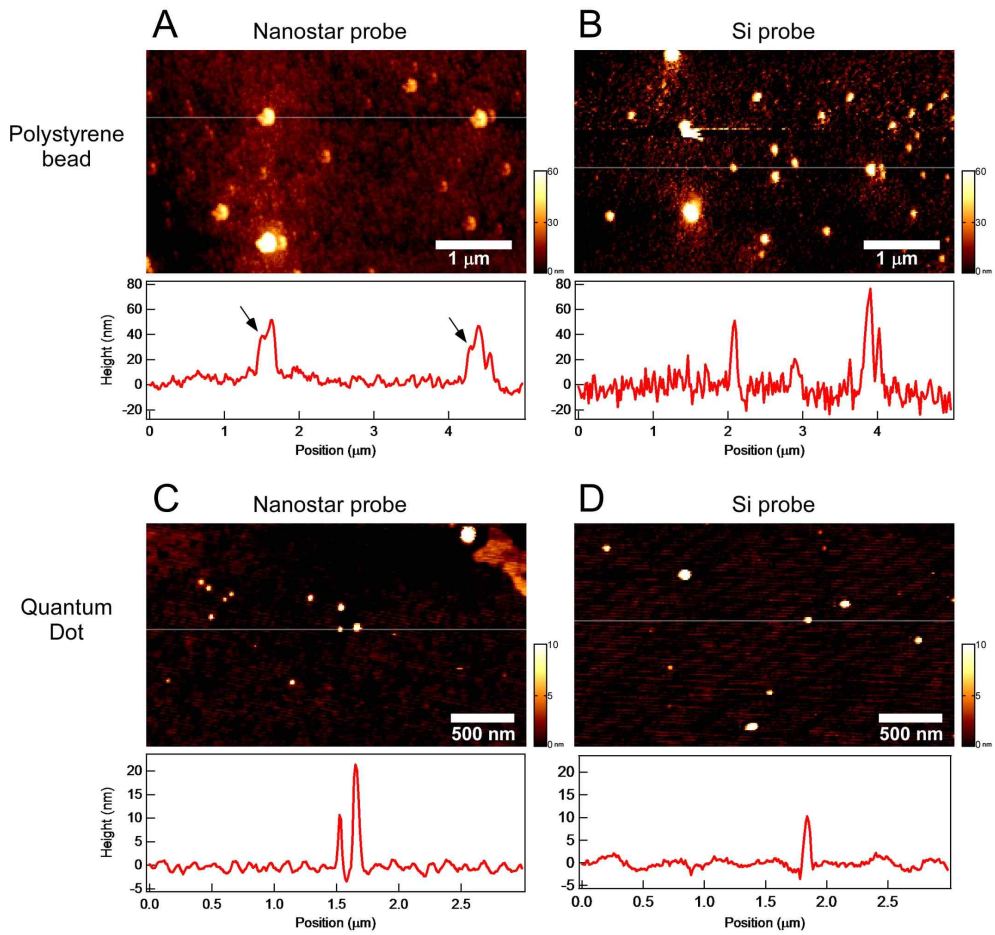

Figure 24 The AFM tapping mode topographic images of polystyrene beads (**A** and **B**, average diameter of 20 nm) and CdSe quantum dots (**C** and **D**, average diamter 5-10 nm), obtained with a commercially availabe Si-tip (**B** and **D**) and the nanostar tip (**A** and **E**). An associated profile for each images sampled along the white line is presented below of the corresponding image. The black arrows in **A** point the topographic feature arising from the tip-convolution effect.

Two types of samples are separately prepared for the TERS and TEF as indicated in Figure 25.

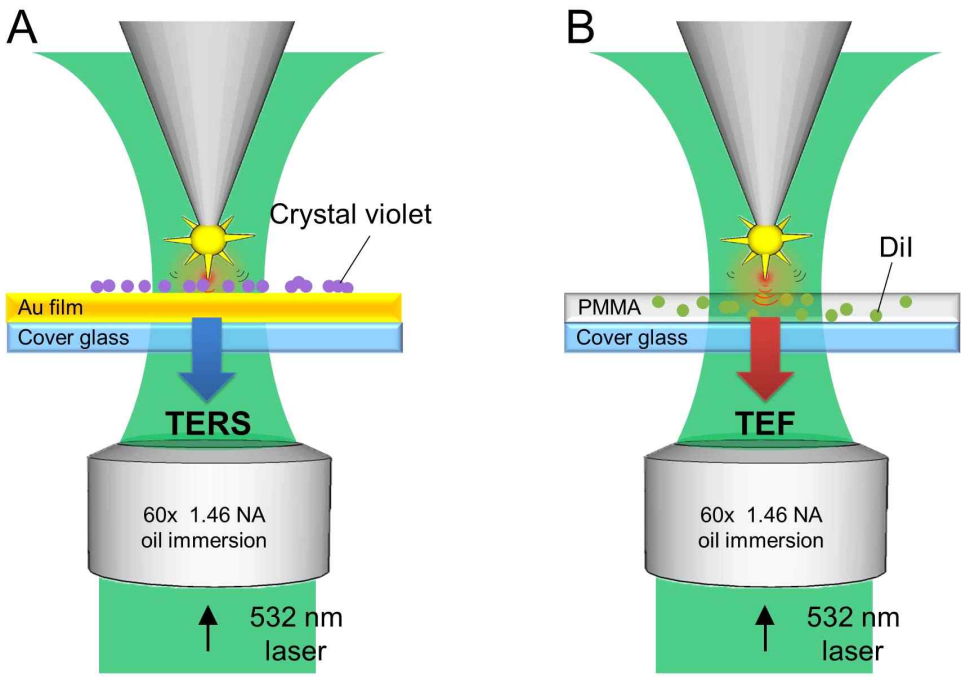

Figure 25 Two types of the samples for the TENOM. **A** CV molecules were placed on the gold-coated cover glass for the TERS measurement. **B** DiI dye embedded in a PMMA layer on the cover glass for the TEF measurement.

For the TERS measurements, clean cover galsses were coated with the Au (10 nm)/Ti (2 nm) using an e-beam evaporator. A stock solution of crystal violet (CV, 90.0%, Sigma Aldrich) was diluted in ethanol, and a drop of 10 μL was placed on the gold-coated cover glasses. The junction between Au nanostar of the probe and gold flim makes the strongest hot-spot.

For the TEF measurements, on the other hand, the poly(metyl methacrylate) (PMMA, 15000 MW, Sigma Aldrich) film is coated on

the glass. 1,1′-dioctadecyl-3,3,3′,3′-tetramethylindocarbocyanine perchlorate (DiI, Sigma Aldrich) dye molecules[61] are embedded in the PMMA film. The PMMA coating was conducted for the following reasons; ① to adjust the distance between the AFM tip and dye molecules, ② to immobilize the dye molecules, and ③ to prevent the photobleaching of the fluorescent. Accordingly, to make the proper thickness of the PMMA film for TEF, we need to find the proper concentration of the PMMA. After many trials and errors (Figure 26), we can get a linear plot that the thickness of the film for PMMA as a function of the concentration of the PMMA in Figure 16E. The thickness is measured the following procedure; First, we had scanned 5×5 μm area of the PMMA sample with commercial silicon tip by contact mode. Then, film was scratched out within the scanned area. Next, we scanned larger area, 10×10 μm with same tip but by tapping mode. That area involves all part of scratched area so we can confine the thickness of the film by comparing the height contrast. As a result, 0.5 mg/mL (PMMA/toluene) of the PMMA concentration is used and at this time the thickness of film is under 2 nm. This concentration of PMMA is made by adding 1 mL of the PMMA solution to the 20 μL of 10^{-8} M DiI solution. DiI solution was prepared in DMSO and diluted in toluene before using. Then, a drop of 20 μL solution was placed on a cover glass that had been cleaned by Piranha and RCA I processes. With a spin coater (Spin-1200, MIDAS System) at 3000 rpm for a 60 seconds, a thin layer with under 2 nm of thickness of PMMA flim was formed.

We need to check some requirements for sample to show TEF. The quantum yield of DiI is small value as 0.07 in methanol. Also, absorption wavelength of DiI dye is resonant with the wavelength of the excitation source (in our setup, λ_{ex} = 532 nm). Maximum excitation/emission wavelength of DiI dye are 549/565 nm, respectively. Taken together, DiI dye is good candidate for TEF.

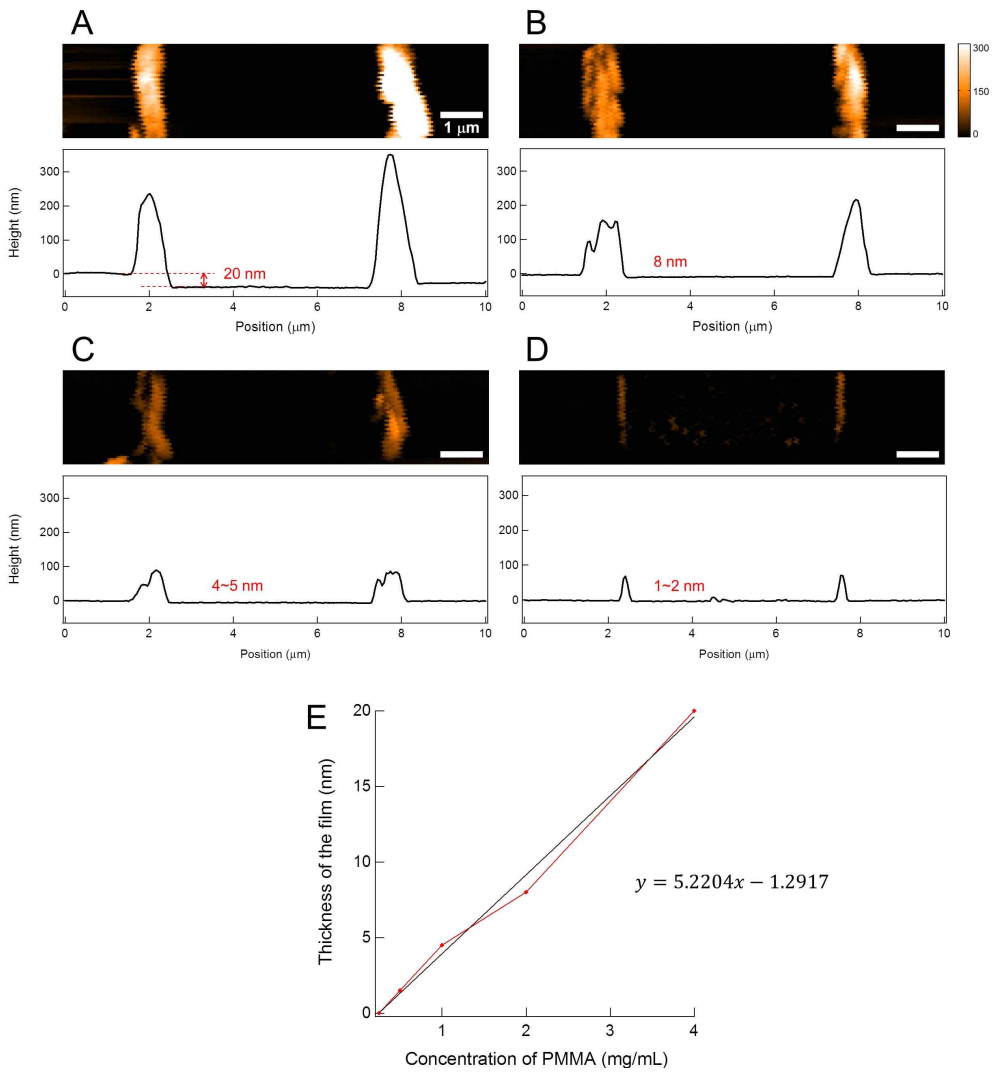

Figure 26 The measurement of the PMMA film thickness. The topographic images and the corresponding line profile in the concentration of the PMMA with **A** 4 mg/mL, **B** 2 mg/mL, **C** 1 mg/mL and **D** 0.5 mg/mL in toluene solution. **E** The linear plot that the thickness of the polymer film as a function of the concentration of PMMA.

4.3. Tip-Enhanced Raman Scattering

For the TERS measurement, the contact mode in the AFM was used to approach as close to the surface of the sample as possible. To check the experimental conditions for TERS, we got two spectra with the tip by time intervals. And we are keeping an eye on aspect of the intensity change in Raman peaks. With regard to two consecutive TERS spectra, less than 20% of decrease in TERS signal was observed under exposure to 80 μW of laser power (Figure 27). This fact supports that the TERS experimental condition (power of laser, integration time) is reasonable for the TERS measurements. Figure 28 shows Raman spectra of the CV sample collected with and without the tip. The spectra demonstrate the pronounced enhancement of eight major peaks of CV (see Table 1 for the peak assignments). For the particular spectra shown, the ratio of peak intensity with (I) and without (I_0) tip is ~10 as determined by the area of the peak at 804 cm^{-1} (I/I_0 = 215/20). Note that I_0 also contains a SERS signal of CV arising from the hotspots on Au surfaces. We found that the ratio varied from 2 to 10 for different tips, yet all of the tips showed TERS activity.

The control experiment was conducted to establish a standard how efficiently the signal of TERS exerts. For fhe control, the AFM tip had been coated with the Au film (40 nm)/Ti (1 nm) by the e-beam evaporation. Raman spectra with and without the Au-coated tip is shown in Figure 29. For comparison, the experimental conditions are set equal to those of the experiment with the nanostar probe. In the control experiment, the ratio of peak intensity at 804 cm^{-1} with and without tip is 1.38 (= 121/88). Compared to that of the nanostar, it is very small value but TERS activity is appeared though.

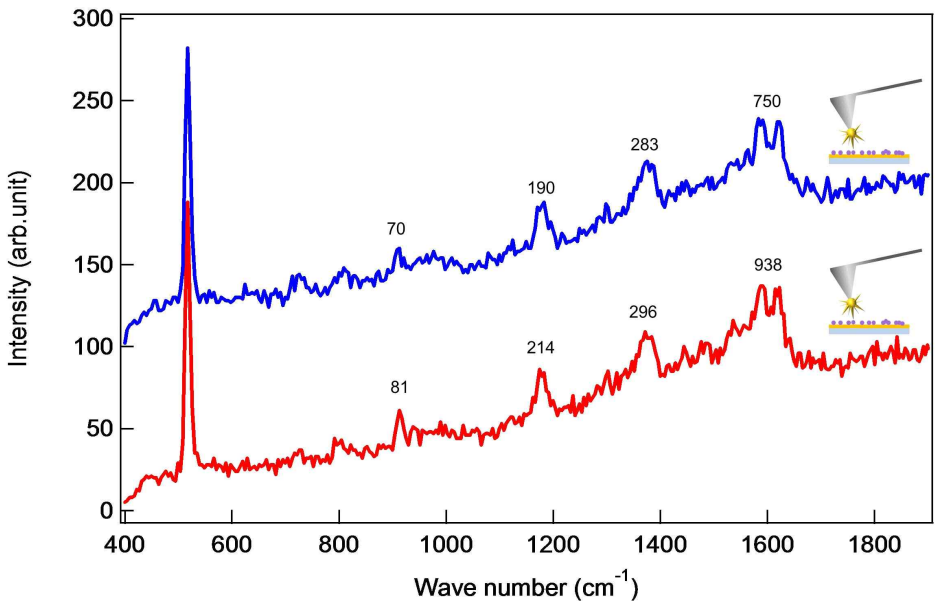

Figure 27 The two consecutive TERS spectra (red→blue) of CV on the gold surface obtained from the same tip and the same position in the sample (each with 10 seconds of integration time and 80 μW of the laser power). We observe less than 20% of decrease in TERS signal. For the clarity, the second spectrum is displaced along y-axis. Numbers in the spectra indicate the integrated area of each peaks.

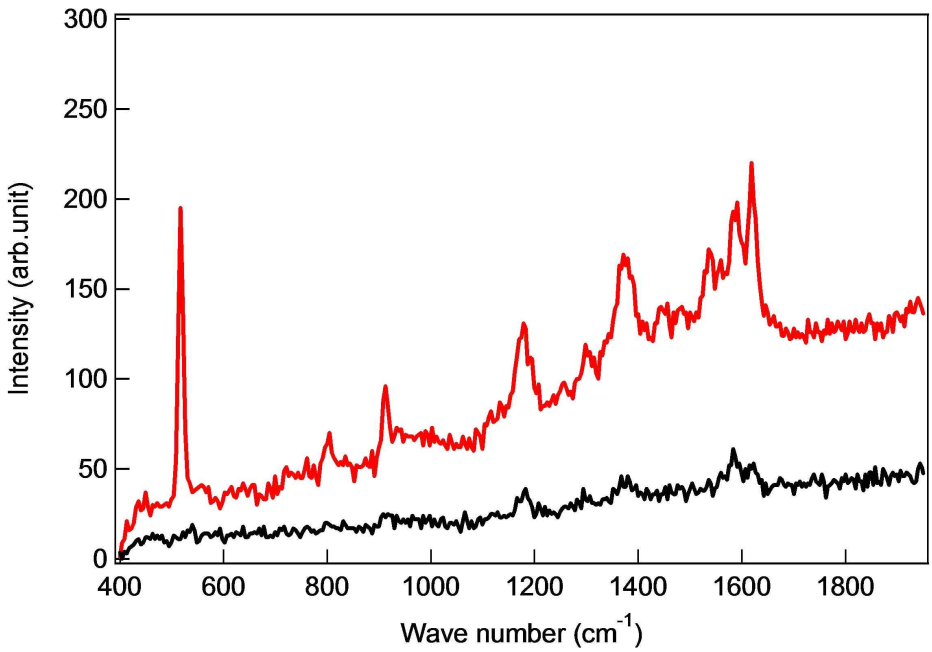

Figure 28 TERS spectra of crystal violet (inset in figure) with (red) and without (black) the nanostar tip. Laser power and exposure time were 80 μW and 10 seconds, respectively. Major vibration modes of CV are indicated with vertical lines and wavenumbers. The asterisk(∗) points to the Si-phonon mode of the tip.

Peak No.	Raman	TERS	Peak assignments[a]
1	-	804	$\gamma_{as,\,oop,\phi-H}$
2	-	912	
3	1183	1178	$\nu_{as,\,ip,\,C-H,C-\phi}$
4	1367	1367	$\nu_{as,\phi-C-\phi,C-N}$
5	1380	1387	ω
6	1536	1536	
7	1583	1591	
8	1622	1618	

Table 2 Peak assignments for the Raman and the TERS spectra for the crystal violet[b] (in cm^{-1})

a) All of the confocal Raman and TERS spectra were obtained with λ_{ex} = 532 nm.

b) Vibrational peak assignments and notations.[62-65]

γ : bend, as: antisymmetric, oop: out-of-plane; ν : stretch; ip : in-plane;

ω : ring breathing.

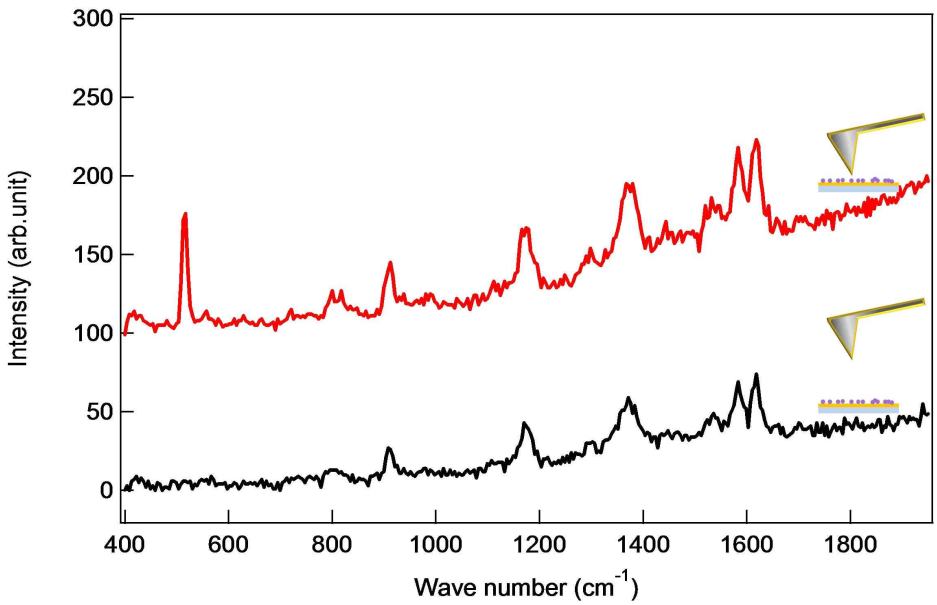

Figure 29 The control experiment for TERS spectra of crystal violet with (red) and without (black) the Au-coated probe (the thickness of Au is 40 nm). Laser power and exposure time were 80 μW and 10 sec, as same as in the experiment with the nanostar probe.

4.4. Tip-Enhanced Fluorescence

In the TEF experiment, the laser power was controlled to less than 200 nW in order to avoid photobleaching. Figures 30A-E compare TEF images of the DiI sample with the tip engaged with the surface (Figure 30; first row, tip-on) and with images with the tip retracted (Figure 30; second row, tip-off). Two features are evident from the comparison. First, the tip-on images show significantly enhanced signal intensity and spatial resolution of 90-200 nm compared with the tip-off images showing diffraction-limited spot sizes of 300-400 nm.

There are some facts are worthy of notice. During the TEF scanning, spikes on the nanostar probe often became blunt, possibly due to mechanical deformation by the tapping mode feedback with the sample surface. Nevertheless, the nanostar probes maintained a constant level of enhancement during several hours of usage. Second, we found that the degree of the enhancement varied from one molecule to another, with the observed optical enhancement varying from 5 times to 10^2 times within the same sample. For example, only one spot out of the two in the images in Figure 30D shows significant tip-enhancement (the lower bound for enhancement is 100 as determined by the Gaussian fitting of the line-profiles of the same TEF spot with and without the tip). Such variation may originate from different orientations of DiI molecules[25,26,66] and the variability in the tip-molecule distance.[23-27] Certainly, the nanostar tip produced images of individual DiI spots as the superposition of a diffraction-limited Gaussian point-spread function (psf) with a sharp tip-enhnaced psf (see Figure 30E). Therefore, for the Figure 30A and E, two Gaussian functions were used for one spot in order to model the enhanced (narrow) and unenhanced (broad) components of fluorescence from DiI spot. The images obtained with a monolithic

Au-coated tip (thickness of 10 nm), on the other hand, showed only a diffraction-limited psf with a sharp dip (see Figure 30F) by the Au-surface of the tip indicating tip-induced fluorescence quenching instead of tip-enhancement (compare Figure 30E and F).

As recently confirmed experimentally by Maouli et al,[29] the tip with isolated nanostuctures show better local field enhancement than the tips monolithically coated with gold or silver. This difference originates from the fact that the extended cone-structures associated with metal-coated tips are largely off-resonant with the excitation light, whereas the isolated nanostructures are fully resonant (dipolar plasmons) with the visible radiation. The ideal cone-shaped TERS tips should in theory provide extreme field enhancement, yet in reality such geometry is hardly achieved in typical experiments. In particular for the TEF measurement, there exists surface-induced quenching competing against the fluorescence enhancement caused by the local field enhancement. The quenching rate for the nanostar and coated tips will be similar. For the monolithic tip, the field enhancement is insufficient to overcome the fluorescence quenching, whereas for the nanostar tip, the enhancement is sufficient. This is why we observe a dip (quenching) in the TEF images obtained with the coated tip (Figure 30F).

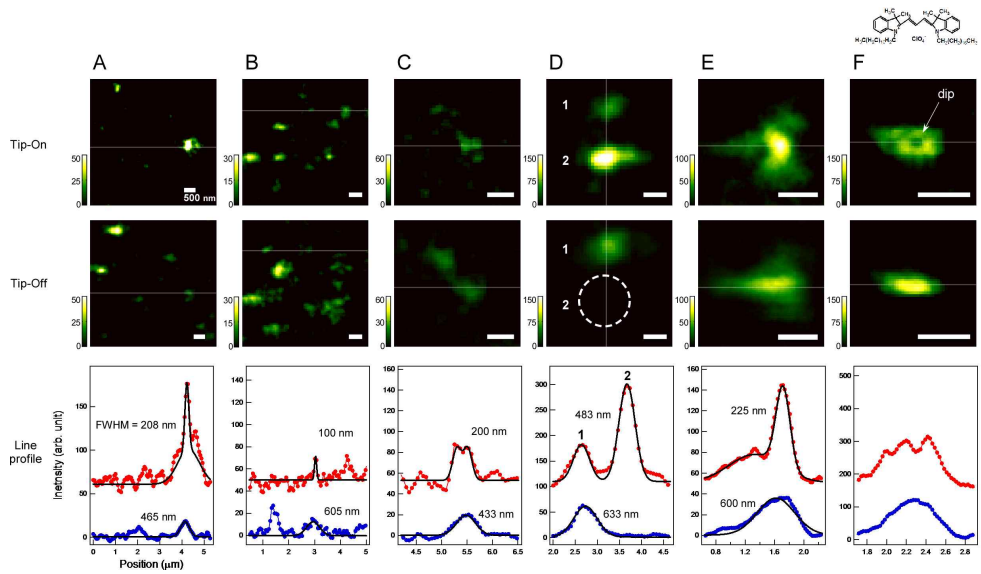

Figure 30 TEF images of DiI sample wih (tip-on) and without (tip-off) the nanostar probe. The images were obtained from the same sample at different position. For each of the data set, different probes were used except for **A** and **E**. **A-E** show the representative TEF images (with and without the tip) and line profiles (red: tip-on, blue: tip-off) sampled along the lines indicated in the corresponding images. **F** The TEF images obtained with a Au-coated tip. The tip-on and tip-off line profiles are offset in y-axis for the better visibility of the data. The fits to the Gaussian functions (black solid curves) are also shown.

4.5. Conclusions

For the nanostar probe and its performance for TERS and TEF showed that the current approach is viable for TENOM, although there still exists room for further improvement of the nanostar tip and their application. First of all, the nanostar tips showed large tip-to-tip variations in nano-optical properties, which we believe originated from the dispersion of the nanostar shape and the variation in spike orientation. The structural imperfections as well as the resonance characteristics because the dipolar plasmon of the nanostar is not optimally resonant with the excitation wavelength, may have contributed to the marginal spatial resolution (~100 nm) and the field enhancement observed in TERS and TEF. With further refinement of the structure or use of more appropriate excitation wavelength, we will be able to optimize the field enhancement. By carefully tuning the growth steps, the plasmonic properties of nanostars can be further optimized, or different shapes of nanoparticles (such as octahedrons or cubes) can be grown at the end of the tip. Such size and shape fine-tuning will help improve the performance of the tip for improved mechanical stability, signal enhancement, and spatial resolution in TERS and TEF. Besides the plasmonic properties of the tip, the properties of the sample (molecules and substrate) will influence the spectroscopic enhancement. For the TERS measurement, the enhancement will be influenced by the tip-sample distance and the local morphology of the substrate (note that our substrate has a finite roughness.). For the TEF measurement, we use the PMMA matrix to immobilize the target molecule. The finite thickness of the PMMA layer, as well as the random orientation of the molecule, will cause the variation in fluorescence enhancement through the variation in tip-molecule distance. Currently, we are exploring ways to improve such

variabilities of sample/substrates, as well as the plasmonic properties.

Above all, the majority of the nanostar probes showed local field enhancement with high spatial resolution that were useful for TERS and TEF measurement. The current probes, however, still have limitation for the effectiveness of the TENOM. Extended investigation of such probes promises deeper understanding of the optical phenomena and fabrication of more effective probes.

References

1. A. Hartschuh, *Angew. Chem. Int. Edit*, 2008, **47**, 8178 -8191.
2. N. Mauser and A. Hartschuh, *Chem. Soc. Rev.*, 2014, **43**, 1248-1262.
3. Lipson, Lipson and Tannhause, Optical Physics., *United Kingdom: Cambridge.*, 1998, 340.
4. Katherine A.Willets, Richard P. Van Duyne, *Annu. Rev. Phys. Chem.*, 2007, **58,** 267 - 297.
5. Neil Anderson, Pascal Anger, Achim Hartschuh, Lukas Novotny, *Nano Lett*, 2006, **6**, 4, 744-749.
6. Chi Chen, Norihiko Hayazawa, Satoshi Kawata, *Nat. Commun.*, 2014, **5**, 3312
7. Luiz Gustavo Canc¸ado, Achim Hartschuh, Lukas Novotny, *J. Raman Spectrosc.*, 2009, **40**, 1420-1426.
8. Jun Yu, Yuika Saito, Taro Ichimura, Satoshi Kawata, Prabhat Verma, *Appl. Phys. Lett.*, 2013, **102**, 123110.
9. N. Kumar, B. Stephanidis, R. Zenobi, A. J. Wain, D. Roy, *Nanoscale*, 2015, **7**, 7133 - 7137.
10. Noriko N. Horimoto, Shigeru Tomizawa, Yasuhiko Fujita, Shinji Kajimoto, Hiroshi Fukumura, *Chem. Commun.*, 2014, **50**, 9862-9864.
11. Gennaro Picardi, Marc Chaigneau, Razvigor Ossikovski, Christophe Licitra, Guillame Delapierre, *J. Raman Spectrosc.*, 2009, **40**, 1407-1412.
12. Yu Liu, Shuping Xu, Haibo Li, Xiaoguang Jian, Weiqing Xu, *Chem. Commun.*, 2011, **47**, 3784 - 3786.
13. Debdulal Roy, Jian Wang, Craig Williams, *J. Appl. Phys.*, 2009, **105**, 013530.
14. Wenyu Tao, Aiwu Zhao, Henghui Sun, Zibao Gan, Maofeng Zhang, Da Li, Hongyan Guoa, *RSC Adv.*, 2014, **4**, 3487-3493.
15. Lukas Novotny, Niek van Hulst, *Nature Photonics*, 2011, **5**, 83-90.
16. Anshuman Singh, Gaetan Calbris, Niek F. van Hulst, *Nano Lett.*, 2014, **14**, 8, 4715-4723.
17. Christiane Ho¨ppener, Ryan Beams, Lukas Novotny, *Nano Lett.*, 2009, **9**,

2, 903-908.
18. Jordan M. Gerton, Lawrence A. Wade, Guillaume A. Lessard, Z. Ma, Stephen R. Quake, *PRL*, 2004, **93**, 18, 180801.
19. Hadi Eghlidi, Kwang Geol Lee, Xue-Wen Chen, Stephan Go¨tzinger, Vahid Sandoghdar, *Nano Lett.*, 2009, **9**, (12), 4007-4011.
20. Mathieu Mivelle, Thomas S. van Zanten, Lars Neumann, Niek F. van Hulst, Maria F. Garcia-Parajo, *Nano Lett.*, 2012, **12**, 11, 5972-5978.
21. Palash Bharadwaj, Ryan Beams, Lukas Novotny, *Chem. Sci.*, 2011, **2**, 136-140.
22. Palash Bharadwaj, Pascal Anger, Lukas Novotny, *Nanotechnology*, 2007, **18,** 044017.
23. A. I. Dragan, C. D. Geddes, *Phys. Chem. Chem. Phys.*, 2011, **13**, 3831-3838.
24. W. E. Moerner, David P. Fromm, *Rev. Sci. Instrum.*, 2003, **74**, 8, 3597.
25. Sergei Ku¨hn, Ulf Ha°kanson, Lavinia Rogobete, Vahid Sandoghdar, 2006, *PRL*, **97**, 017402.
26. Pascal Anger, Palash Bharadwaj, Lukas Novotny, *PRL*, 2006, **96**, 113002.
27. J. Azoulay, A. D´ebarre, A. Richard, P. Tch´enio, *Europhys. Lett.*, 2000, **51,** 4, 374-380.
28. Anatoliy I. Dragan, Chris D. Geddes, *Appl. Phys. Lett.*, 2012, **100**, 093115.
29. Phil Holzmeister, Enrico Pibiri, Ju¨rgen J. Schmied, Tapasi Sen, Guillermo P. Acuna, Philip Tinnefeld, *Nat. Commun.*, 2014, **5**, 5356.
30. Imad Maouli, Atsushi Taguchi, Yuika Saito, Satoshi Kawata, Prabhat Verma, *Appl. Phys. Express*, 2015, 8, 032401.
31. Minsky. M, *Scanning.*, 1988, 10, 128-138.
32. Rober H Webb, *Rep. Prog. Phys.*, 1996, **59**, 427-471.
33. D. Semwogerere, E.R.Weeks, Confocal Microscopy, in: Encyclopedia of Biomaterials and Biomedical Engineering., *Taylor&Francis.*, 2005.
34. Yuika Saito, and Prabhat Verma, *J. Phys. Chem. Lett.*, 2012, **3**, 1295-1300.

35. Toshihiro Mino, Yuika Saito, Hiroyuki Yoshida, Satoshi Kawata, Prabhat Verma, *J. Raman spectrosc.*, 2012, **43**, 2029-2034.
36. Hidekazu Ishitobi, Issei Nakamura, Taka-aki Kobayashi, Norihiko Hayazawa, Zouheir Sekkat, Satoshi Kawata, Yasushi Inouye, *ACS photonics.*, 2014, **1,** 3, 190-197.
37. Anna M. Chizhik, Regina Ja¨ger, Alexey I. Chizhik, Sebastian Ba¨r, Hans-Georg Mack, Marcus Sackrow, Catrinel Stanciu, Alexey Lyubimtsev, Michael Hanack, Alfred J. Meixner, *Phys. Chem. Chem. Phys.*, 2011, **13**, 1722-1733.
38. R. Dorn, S. Quabis, G. Leuchs, *Phys. Rev. Lett.*, 2003, **91**, 233901.
39. Franz J. Giessibl, *Rev. Mod. Phys.*, 2003, **75**, 3, 949-983.
40. Nader Jalili, Karthik Laxminarayana, *Mechatronics*, 2004, **14**, 907 - 945.
41. Veeco Instruments Inc, MultiMode SPM Instruction Manual, 2004, NanoScope Software Version 5, 38-65.
42 W Kim, N Kim, JW Park, ZH Kim, *Nanoscale*, 2016, **8**, 987-994.
43. D. Kim, N. K. Chung, J. S. Kim and J. W. Park, *Soft Matter*, 2010, **6**, 3979-3984.
44. Y. J. Jung, B. J. Hong, W. Zhang, S. J. B. Tendler, P. M. Williams, S. Allen and J. W. Park, *J. Am. Chem. Soc.*, 2007, **129**, 9349-9355.
45. P. Hinterdorfer and Y. F. Dufrene, *Nat. Methods*, 2006, **3**, 347-355.
46. Lumerical Solutions, http://www.lumerical.com/
47. J. Kalbacova, R. D. Rodriguez, V. Desale, M. Schneider, I. Amin, R. Jordan and D. R. Zahn, *Nanospectroscopy*, 2014, **1**, 12 - 18.
48. G. Socrates, Infrared and Raman characteristic group frequencies: tables and charts, *Ltd WJS*, 2001, 245.
49. Y. R. Lee, M. S. Kim and C. H. Kwon, *Bull. Korean Chem. Soc*, 2013, **34**, 470-474.
50. W. H. Park and Z. H. Kim, *Nano Lett.*, 2010, **10**, 4040-4048.
51. K. Kim, H. B. Lee and K. S. Shin, *Spectrochim. Acta A*, 2013, **100**, 10-14.
52. K. Kim and K. S. Shin, *Anal. Sci.*, 2011, **27**, 775-783.
53. H. K. Yuan, C. G. Khoury, H. Hwang, C. M. Wilson, G. A. Grant and

T. Vo-Dinh, *Nanotechnology*, 2012, **23**, 075102.
54. K. Liu, Y. Song, W. Feng, N. N. Liu, W. K. Zhang and X. Zhang, *J. Am. Chem. Soc.*, 2011, **133**, 3226-3229.
55. C. J. Orendorff and C. J. Murphy, *J. Phys. Chem. B*, 2006, **110**, 3990-3994.
56. M. Z. Liu and P. Guyot-Sionnest, *J. Phys. Chem. B*, 2005, **109**, 22192-22200.
57. M. Grzelczak, J. Perez-Juste, P. Mulvaney and L. M. Liz-Marzan, *Chem. Soc. Rev.*, 2008, **37**, 1783-1791.
58. R. Michalitsch, B. J. Palmer and P. E. Laibinis, *Langmuir*, 2000, **16**, 6533-6540.
59. T. K. Sau and C. J. Murphy, *J. Am. Chem. Soc.*, 2004, **126**, 8648-8649.
60. L. Lu, A. Kobayashi, K. Tawa and Y. Ozaki, *Chem. Mater.*, 2006, **18**, 4894-4901.
61. M. Mivelle, T. S. van Zanten and M. F. Garcia-Parajo, *Nano Lett.*, 2014, **14**, 4895-4900.
62. H. Masuhara and S. Kawata, *Nanophotonics: Integrating Photochemistry*, Optics and Nano/bio Materials Studies. Elsevier, 2004, 132-138.
63. S. Sunder and H. Bernstein, *Can. J. Chem.*, 1981, **59**, 964-967.
64. M. Volny, A. Sengupta, C. B. Wilson, B. D. Swanson, E. J. Davis and F. Turecek, *Anal. Chem.*, 2007, **79**, 4543-4551.
65. S. L. Kleinman, E. Ringe, N. Valley, K. L. Wustholz, E. Phillips, K. A. Scheidt, G. C. Schatz and R. P. Van Duyne, *J. Am. Chem. Soc.*, 2011, **133**, 4115-4122.
66. S. Kuhn and V. Sandoghdar, *Appl. Phys. B*, 2006, **84**, 211-217.

Abstract (in Korean)
나노입자 탐침을 이용한 탐침증강 분광법

나노크기 물체의 화학적·물리학적 특성을 연구하기 위해서 소량의 분자에서의 화학적 정보와 높은 공간 분해능을 가지는 광학이미지는 필수적이다. 이런 관점에서 탐침 증강 근접장 광학 현미경(TENOM)은 높은 공간 분해능을 제공할 뿐만 아니라 탐침 끝 부분에서의 플라즈모닉 향상에 의해 신호의 세기가 강하기 때문에 촉망받고 있다. 이는 다시 말하자면, 탐침 증강 근접장 광학 현미경은 탐침의 장 향상과 공간 한정에 결정적으로 의존한다는 것을 의미한다. 그래서 우리는 보다 나은 탐침의 광학적 성질을 찾기 위해서 다양한 종류의 탐침을 이용해서 향상된 광학 신호를 받는 탐구를 진행하였다.

탐침 증강 근접장 광학 현미경을 적용하기 위해, 우리는 532 nm 파장을 가지는 방사상으로 편광된 빛이 포함된 공초점 현미경과 탐침이 탑재된 원자간력 현미경(AFM)을 사용하였다. 실험 구성 장비의 유효성을 점검하기 위해 우리는 먼저 탐침에 평행한 방향(z축)으로 편광을 만들어 주는 방사형 편광기를 테스트하였다. 방사형 모드와 순환형 모드에서 나일 레드(이는 폴리스타이렌 비드 안에 들어있으며, 비드의 지름은 20 nm)의 형광 이미지를 얻음으로써 레이저의 방향이 z축에 평행함을 확인할 수 있었다. 그 다음으로 탐침 증강 라만 산란(TERS)과 탐침 증강 형광(TEF)에 대한 실험이 수행되었으며, 이는 비슷한 방식으로 합성된 두 가지 유형의 특별한 방법으로 제작된 탐침을 이용하였다.

우리의 실험 구성 장비가 탐침 증강 라만 산란과 탐침 증강 형광 측정에 적합한지 확인하기 위해서, 우리는 금 입자를 중심으로 조절된 두께로 은 껍질의 구조를 가지는 나노 입자를 탐침을 사용하였다. Au@Ag 탐침의 합성을 위해 금 나노 입자를 DNA-DNA 상호작용에 의해 집어 올리고, 은 용액에서 성장하는 과정이 시행되었다. 탐침 증강 라만 산란 측정을 위해서 Au@Ag 탐침(나노 입자 크기: 22-90 nm)과 함

께 샘플로는 금 필름 위에 바이페닐 싸이올(BPT)로 구성된 자가 조립 단층(SAM)이 준비되었다. 우리는 이러한 탐침이 높은 플라즈모닉 장 향상을 보임을 확인하였고, 이는 나노 입자의 크기가 증가할수록 분명하게 드러났다.

더 나아가서, 우리는 중심 지름이 70 nm에 뾰족한 가지 부분의 길이가 50 nm에서 80 nm가 되는 금속 나노스타로 구성된 새로운 주사 탐침을 개발하였다. 접근 방법은 탐침 픽업 과정과 은 이온의 존재 하에 아스코르브산과 함께 금 이온이 환원되면서 나노스타의 뾰족한 가지 부분이 자라는 성장과정이 포함된다. 나노 스타 탐침은 그 뾰족한 끝 부분에 의해 좁은 부위에 향상된 전자기장을 만든다. 우리는 거의 모든 탐침이 탐침 증강 라만 산란과 탐침 증강 형광에 대해서 100 배까지의 신호 향상과 더불어 100 nm 이하의 광학 해상도를 가짐을 확인하였다. 이는 탐침 증강 형광 분광법에서는 DiI 염료, 탐침 증강 라만 산란 분광법에서는 크리스탈 바이올렛(CV)으로 실험하였다. 그러나 현재의 탐침은 커다란 탐침에 대한 가변성을 보였고, 이는 샘플 표면에 대하여 나노 스타의 뾰족한 가지 부분의 축 방향을 조절할 수 없기 때문에 나타났을 것이다. 추후에 제조 방법에 있어서 개선이 요구되는 바이다. 이 결과는 전반적으로 탐침 증강 분광법에 효율적인 새로운 탐침 제조에 대한 접근법을 뒷받침해준다.